

THE RELATIONSHIP BETWEEN STELLAR MASS, GAS METALLICITY, AND STAR FORMATION RATE FOR H α -SELECTED GALAXIES AT $Z \approx 0.8$ FROM THE NEWH α SURVEY

MITHI A. DE LOS REYES^{1,2}, CHUN LY^{2,3,10}, JANICE C. LEE^{2,4}, SAMIR SALIM⁵, MOLLY S. PEEPLES², IVELINA MOMCHEVA⁶,
JESSE FEDDERSEN^{6,2}, DANIEL A. DALE⁷, MASAMI OUCHI⁸, YOSHIAKI ONO⁸, AND ROSE FINN⁹

(Dated: August 4, 2018)
Draft version August 4, 2018

ABSTRACT

Using a sample of 299 H α -selected galaxies at $z \approx 0.8$, we study the relationship between galaxy stellar mass, gas-phase metallicity, and star formation rate (SFR), and compare to previous results. We use deep optical spectra obtained with the IMACS spectrograph at the Magellan telescope to measure strong oxygen lines. We combine these spectra and metallicities with (1) rest-frame UV-to-optical imaging, which allows us to determine stellar masses and dust attenuation corrections, and (2) H α narrowband imaging, which provides a robust measure of the instantaneous SFR. Our sample spans stellar masses of $\sim 10^9$ to $6 \times 10^{11} M_{\odot}$, SFRs of 0.4 to $270 M_{\odot} \text{ yr}^{-1}$, and metal abundances of $12 + \log(\text{O}/\text{H}) \approx 8.3\text{--}9.1$ ($\approx 0.4\text{--}2.6 Z_{\odot}$). The correlations that we find between the H α -based SFR and stellar mass (i.e., the star-forming “main sequence”), and between the stellar mass and metallicity, are both consistent with previous $z \sim 1$ studies of star-forming galaxies. We then study the relationship between the three properties using various plane-fitting techniques (Lara-López et al.) and a curve-fitting projection (Mannucci et al.). In all cases, we exclude strong dependence of the $M_{\star}\text{--}Z$ relation on SFR, but are unable to distinguish between moderate and no dependence. Our results are consistent with previous mass-metallicity-SFR studies. We check whether dataset limitations may obscure a strong dependence on the SFR by using mock samples drawn from the SDSS. These experiments reveal that the adopted signal-to-noise cuts may have a significant effect on the measured dependence. Further work is needed to investigate these results, and to test whether a “fundamental metallicity relation” or a “fundamental plane” describes star-forming galaxies across cosmic time.

1. INTRODUCTION

Studying the general relationships between the physical properties of galaxies—including stellar mass (M_{\star}), gas-phase metallicity (Z), and star formation rate (SFR)—provides clues about galaxy formation and evolution. Stellar mass is an estimate of the amount of gas converted into stars in a galaxy over time, while the SFR measures the current rate at which gas is consumed to form stars. In addition, the gas-phase metallicity reflects both the amount of gas reprocessed by stars and galactic interactions with the environment through the infall and outflow of gas.

Combinations of these three properties have been well-studied. The mass–metallicity ($M_{\star}\text{--}Z$) relation is a non-linear one in which Z increases with M_{\star} up to a stellar mass of about $3 \times 10^{10} M_{\odot}$ and then plateaus (e.g.,

Tremonti et al. 2004, hereafter T04; Moustakas et al. 2011; Zahid et al. 2011; Andrews & Martini 2013). The relation has been shown to evolve towards lower metallicity at higher redshifts (Mannucci et al. 2009; Erb et al. 2006; Zahid et al. 2013a; Maiolino et al. 2008), although the exact nature of this evolution is unclear, in part because high- z results are still significantly incomplete at low stellar masses. Similarly, the positive correlation between M_{\star} and SFR ($\text{SFR} \propto M_{\star}^{0.6}$; Salim & Lee 2012); called the “star-formation sequence” (Salim et al. 2007) or the galaxy “main sequence” (Noeske et al. 2007) shows evolution with redshift toward higher SFRs at earlier times (e.g., Noeske et al. 2007; Elbaz et al. 2007; Whitaker et al. 2012).

Despite the tightness of the $M_{\star}\text{--}Z$ relation, some intrinsic scatter remains (~ 0.1 dex). It has been suggested that part of this scatter can be accounted for by a secondary dependence on the SFR—at a given stellar mass, lower-metallicity galaxies tend to have higher SFRs (Ellison et al. 2008; Mannucci et al. 2010; Lara-López et al. 2010), and lower SFR galaxies tend to have higher metallicities (Ellison et al. 2008; Peeples et al. 2008). A relationship between all three properties was proposed (e.g., Mannucci et al. 2010, hereafter Man10).

The physical origin of such a $M_{\star}\text{--}Z\text{--}SFR$ relation is thought to be a result of the way galaxies process gas. The oxygen-to-hydrogen¹¹ gas ratio in a galaxy is regulated by its stellar mass, history of outflows, and gas

madelosr@ncsu.edu

¹ Department of Physics, North Carolina State University, Raleigh, NC

² Space Telescope Science Institute, Baltimore, MD

³ National Aeronautics and Space Administration, Goddard Space Flight Center, Greenbelt, MD, USA

⁴ Visiting Astronomer, SSC/IPAC, Caltech, Pasadena, CA

⁵ Astronomy Department, Indiana University, Bloomington, IN

⁶ Astronomy Department, Yale University, New Haven, CT

⁷ Department of Physics and Astronomy, University of Wyoming, Laramie, WY

⁸ Institute for the Physics and Mathematics of the Universe, TODIAS, University of Tokyo, Japan

⁹ Physics Department of Physics and Astronomy, Siena College, Loudonville, NY

¹⁰ NASA Postdoctoral Fellow.

¹¹ Oxygen is generally used as a proxy for total metal content, since it is the most abundant gas-phase metal in a galaxy.

mass. The amount of oxygen in the interstellar medium (ISM) is primarily set by the mass of oxygen the galaxy has produced in its lifetime (which is roughly proportional to its stellar mass), less the oxygen mass residing in stars and/or lost in outflows (Peeples et al. 2014). The degree to which the ISM oxygen content is diluted is determined by the galaxy’s gas mass (Peeples & Shankar 2011), which is in turn regulated by a balance between star formation, accretion, and outflows (e.g., Davé et al. 2011; Lilly et al. 2013; Forbes et al. 2014).

Infall of metal-poor gas will initially dilute the metal abundance already present in the ISM while enhancing the SFR, leading to the observed trend of Z and SFR inversely proportional at a given mass. However, as the enhanced star formation continues, the freshly produced metals can quickly erase the signature of fresh inflow, causing an *increase* in metallicity while the SFR is still relatively high (Torrey et al. 2012). Outflows driven by star formation must then be removing these freshly produced metals from the ISM in order for the galaxy to continue to have a low ISM abundance in the while having enhanced star formation. In this scenario, an observed M_\star - Z -SFR relation (and its assumed lack of evolution) is largely coincidental and a result of the tendency for galaxies to move toward an equilibrium between galactic inflows and outflows (Davé et al. 2011).

In this framework, if galaxies at different redshifts universally obey the same relation between stellar mass, gas mass, and gas metallicity, then it could imply something “fundamental” about how galaxies expel their metals through time. Measurements of H I masses are not currently feasible at redshifts beyond the local universe, so SFR has generally been used as a proxy for gas mass. Furthermore, a “fundamental” M_\star - Z -SFR relation would imply that the evolution of the M_\star - Z relation and the star-formation sequence are simply consequences of preferentially observing higher SFRs at higher redshifts (Man10; Hunt et al. 2012).

However, the existence of a fundamental M_\star - Z -SFR relation remains controversial. While several works have found evidence of such a relation at local redshifts (see e.g., Man10; Hunt et al. 2012; Andrews & Martini 2013; Pérez-Montero et al. 2013; Yates et al. 2012, hereafter Yat12), Sánchez et al. (2013) and Hughes et al. (2013) were unable to find a significant dependence of the M_\star - Z relation on the total SFR from integral field spectroscopy at local redshifts, and suggested that previously reported results may be due to the impact of observational effects such as aperture bias on the SFR. At higher redshifts, uncertainty remains over the existence of the M_\star - Z -SFR relation and its evolution. Once again, several studies found evidence of a relation (e.g., Richard et al. 2011; Cresci et al. 2012; Belli et al. 2013; Henry et al. 2013a,b, whose results all agreed with the local M_\star - Z -SFR relation), but other studies were less conclusive. Yabe et al. (2012) and Yabe et al. (2014) found a M_\star - Z -SFR relation deviating slightly from that reported at local redshifts, while Zahid et al. (2013b) found a weak dependence of the M_\star - Z relation on SFR that was significantly different from the local relation and concluded that this was a result of redshift evolution. In addition, Stott et al. (2013) stacked spectra and found evidence that star-forming galaxies at $z \sim 0.8$ and $z \sim 1.5$ have gas-phase metallicities that are consistent with the local

M_\star - Z relation, in contrast with other high- z studies. In most cases, samples are potentially subject to dataset limitations.

Ideally, tracking M_\star , Z , and SFR in a consistent manner across a range of redshifts would provide a solid empirical basis from which to study their relationship and its evolution. At low- z , the M_\star - Z -SFR relation has largely been investigated using data from the Sloan Digital Sky Survey (SDSS; York et al. 2000), a sample consisting of over a hundred thousand galaxies that covers stellar masses from about 10^9 to $10^{11.5} M_\odot$, gas-phase metallicities from $12 + \log(\text{O}/\text{H}) = 8.5$ to 9 (0.6 – $2 Z_\odot$), and SFRs from $\log(\text{SFR}/(M_\odot \text{ yr}^{-1})) = -1.45$ to 0.8 (Man10). The M_\star - Z -SFR relation has also been extended to low-mass galaxies, albeit with smaller sample sizes, down to $M_\star \sim 10^{8.3} M_\odot$ with gamma-ray bursts (Mannucci et al. 2011) and $\sim 10^6 M_\odot$ with dwarf galaxies (Hunt et al. 2012).

Studies at higher redshifts generally have much smaller samples that cover more limited portions of parameter space. For $z = 0.4$ – 1 , Man10 used a sample of 69 galaxies with masses of $10^{8.2}$ – $10^{10.7} M_\odot$ from Savaglio et al. (2005), while Lara-López et al. (2010) (hereafter Lar10) used 88 galaxies from Rodrigues et al. (2008) with masses of 10^9 – $10^{11.2} M_\odot$. At $1 \lesssim z \lesssim 3$, the largest samples used are those of Erb et al. (2006) with 91 UV-selected galaxies at $z \sim 2.2$, and that of the Spectroscopic Imaging Survey (Förster Schreiber et al. 2009), consisting of 62 galaxies at $z \sim 2$, both with mass ranges of $\sim 10^9$ – $10^{11} M_\odot$. Recent efforts have increased the sample size at $z \sim 1.5$. Zahid et al. (2013b) used ~ 150 star-forming galaxies from the COSMOS field at $z \sim 1.6$ and masses ranging from approximately $10^{9.5}$ to $10^{11} M_\odot$. Yabe et al. (2012) and Yabe et al. (2014) conducted near-infrared fiber spectroscopy for 70–340 galaxies at $z \sim 1.4$, Stott et al. (2013) used 64 H α -selected galaxies at $z \sim 1$ – 1.5 , and Henry et al. (2013b) performed infrared grism spectroscopy for 83 galaxies at $z \sim 1.5$ – 2.3 . However, at high- z , spectral stacking is predominantly used, and low-mass galaxies below $5 \times 10^9 M_\odot$ have yet to be studied extensively. There have been efforts to extend $z \approx 0.5$ – 3 studies toward lower stellar masses (Xia et al. 2012; Ly et al. 2014; Henry et al. 2013a,b; Belli et al. 2013); however, sample sizes remain limited.

Thus, the M_\star - Z -SFR relation requires further study, particularly for redshifts above $z \sim 0.3$ (the maximum redshift for the SDSS sample). We aim to build upon previous work by using a sample of star-forming galaxies at $z = 0.8$ (when the universe was roughly ~ 7 Gyr old or half of the Hubble time). We use methods of deriving M_\star , Z and SFR which are similar to those used by local studies. Deep rest-frame optical spectra obtained with the IMACS spectrograph at the Magellan 6.5-m telescope are used to measure gas-phase metallicities with oxygen strong-line calibrations. The spectra are used along with (1) rest-frame UV-to-optical imaging data, which allow us to determine stellar masses and dust attenuation corrections, and (2) our H α narrowband imaging data, which provide a robust measure of SFR.

In Section 2, we describe the NewH α survey, sample selection, and spectroscopy. We also present the photometric properties and the spectroscopic emission-line fluxes of the galaxies used in this analysis. Section 3

discusses the calculation of our physical properties from (1) spectral energy distribution (SED) fitting spanning rest-frame 1400–7000 Å to estimate stellar masses, dust attenuation and UV SFRs, (2) H α luminosities to determine SFRs, and (3) several empirical and theoretical strong-line calibrations to estimate gas-phase metallicity. In Section 4, we use our data to produce a M_* – Z relation and a M_* –SFR relation, and compare them with previous literature results. We also investigate the M_* – Z –SFR relation through different plane-fitting and three-dimensional curve-fitting approaches and compare with literature M_* – Z –SFR relations found at local redshifts. In Section 5, we discuss how limitations in: (1) our dataset, (2) plane-fitting techniques, and (3) the parameterization of the M_* – Z –SFR relation may affect our ability to fully constrain the existence or evolution of the M_* – Z –SFR relation. Finally, we summarize our work in Section 6.

Throughout this paper, we assume a Λ CDM cosmology with $H_0 = 70 \text{ km s}^{-1} \text{ Mpc}^{-1}$, $\Omega_M = 0.3$, and $\Omega_\Lambda = 0.7$ for distance-dependent calculations, which is similar to the Seven-Year WMAP results (Komatsu et al. 2011). Unless otherwise noted, a Chabrier (2003) initial mass function (IMF; hereafter Chabrier) is assumed, and all magnitudes are reported on the AB system (Oke 1974).

2. DATA

We present near-IR narrowband photometry and optical spectroscopy for a sample of 299 H α -selected galaxies at $z \sim 0.8$ from the NOAO Extremely Wide-Field Infrared Imager (NEWFIRM) NewH α survey (Ly et al. 2011a; Lee et al. 2012). The galaxies are identified in the Subaru-XMM Deep Survey (SXDS) field (Furusawa et al. 2008), and deep follow-up spectroscopy was performed with the Inamori Magellan Areal Camera and Spectrograph (IMACS; Dressler et al. 2006) at the Magellan 6.5-m Baade telescope (Momcheva et al. 2013). Emission lines from [O II] $\lambda 3727$ to [O III] $\lambda 5007$ are observed in the spectra. In this section, we provide a brief overview of the NewH α survey, the sample selection, and the IMACS spectroscopy. We also describe multi-wavelength broadband photometry used in SED fitting to derive galaxy stellar masses, dust attenuation, and a second measure of the dust-corrected SFR.

2.1. The NewH α Narrowband Survey: Selecting Emission-Line Galaxies

The NewH α Survey is a program that has obtained emission-line selected samples at intermediate redshift (Lee et al. 2012). The program was designed to efficiently obtain statistical samples of both luminous (but rare) and faint emission-line galaxies. We do this by combining the near-IR imaging capabilities of NEWFIRM (Autry et al. 2003; Probst et al. 2008) at the KPNO/CTIO 4-m telescopes to cover large areas (field-of-view of $27'6 \times 27'6$), and FourStar (field-of-view of $10'9 \times 10'9$; Persson et al. 2008) at the Magellan 6.5-m Baade telescope to probe luminosities that are about a factor of three deeper over smaller areas. For both cameras, we use a pair of custom 1% narrowband filters that fit within windows of high atmospheric transmission and low OH airglow at 1.18 μm and 2.09 μm . With these two filters, deep H α -selected galaxy samples are obtained at $z = 0.8$ (near the beginning of the ten-fold decline in the cosmic SFR

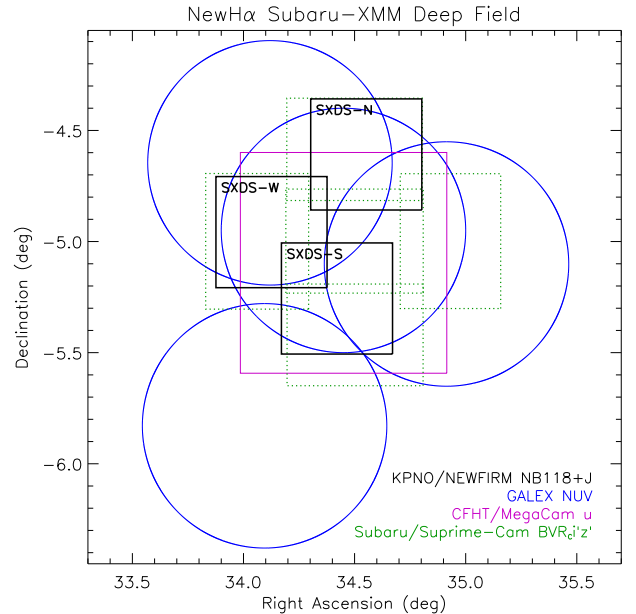


FIG. 1.— NewH α and multi-wavelength ancillary data for the SXDS field. Our NEWFIRM imaging data are shown by labeled squares for three pointings (SXDS-N, SXDS-S, and SXDS-W), along with GALEX NUV (circles, blue in online version), Subaru/Suprime-Cam $BVR_i'z'$ (dashed rectangles, green in online version), and CFHT/Megacam u -band imaging (square, purple in online version). The latter also illustrates the imaging footprint for the UKIRT’s Ultra Deep Survey in JHK .

density) and at $z = 2.2$ (near the peak of the cosmic SFR density; see, e.g., Reddy et al. 2008; Ly et al. 2009, 2011b).

The work presented in this paper focuses on H α emitters at $z = 0.8$, which are detected in NEWFIRM narrowband 1.18 μm (hereafter NB118) and J imaging of a 0.82 deg 2 region in the SXDS (see Figure 1). Here we summarize the NB118 observations, data reduction, and selection method used to produce samples of emission-line galaxy candidates that are then targeted for IMACS spectroscopy.

NEWFIRM at the KPNO 4-m was used to obtain observations over three pointings in the SXDS ($\alpha = 2^h 18^m$; $\delta = -5^\circ$) in 2007 December, 2008 September, and 2008 October. The positioning of these three fields relative to other observations are shown in Figure 1. The cumulative exposure times for each pointing ranged from 8.47 to 12.67 hr in NB118 and from 2.40 to 3.97 hr in J . The median seeing during our observations was $1''.2$, and varied between $1''.0$ and $1''.9$, so point sources are adequately sampled by NEWFIRM’s $0''.4$ pixels. Standard near-IR deep-field observing procedures and reduction techniques were used, and are discussed further in Ly et al. (2011a). The 3σ limiting magnitudes, in apertures (of diameters twice the FWHM) containing at least $\sim 80\%$ of the flux of a point source, range from 23.7 to 24.2 mag (23.4 to 24.1 mag) in NB118 (J).

Sources are selected as emission-line galaxy candidates if they show a J –NB118 color excess that is significant at the 3σ level and is greater than 0.2 mag. The minimum of 0.2 mag is based on the scatter in the color excess for bright point sources. Corrections for the continuum slope are applied based on the $z'–J$ color (Ly et al. 2011a), using publicly available Subaru/Suprime-Cam z' data where available (see Section 2.3 for further

details). The overall procedure follows general selection techniques commonly used in narrowband surveys (Fujita et al. 2003; Ly et al. 2007; Shioya et al. 2008; Villar et al. 2008; Sobral et al. 2009). A total sample of 661 emission-line galaxy candidates meeting these criteria was obtained over the three NEWFIRM pointings. Follow-up spectroscopy was obtained for a subset of these galaxies, as described below. Using a combination of color-selection methods and spectroscopic confirmation, approximately half of these candidates are identified as H α excess emitters at $z \approx 0.8$ (Ly et al. 2011a).

2.2. IMACS Spectroscopy

As discussed in Momcheva et al. (2013), deep follow-up spectroscopy of the NewH α NB118 emission-line galaxy candidate sample was performed in 2008–2009 with IMACS on the Magellan-I telescope. IMACS enables multi-object spectroscopy with slit-masks over a 27.4 diameter area (well-matched to NEWFIRM’s field-of-view), and has good sensitivity to ~ 9500 Å. These two characteristics make IMACS an ideal instrument for optical spectroscopic follow-up of NewH α NB118 excess sources, and in particular, H α emitters at $z \approx 0.8$.

The chosen observational setup yields spectral coverage from 6300 Å to 9600 Å (corresponding to rest-frame ~ 3500 Å to 5300 Å), and captures the strong rest-frame optical emission lines from [O II] $\lambda 3727$ (observed at ≈ 6700 Å) to [O III] $\lambda 5007$ (observed at ≈ 9000 Å) for galaxies at $z \approx 0.8$. Slit widths of 1.5 were chosen (~ 11 kpc at $z = 0.8$). The seeing during our observing runs was generally sub-arcsecond. The typical integration time was 4.5 hours; however, for about half of the H α -emitting galaxies, deeper observations were acquired for a total of 7.75 hours (see Figure 1 of Momcheva et al. 2013) to improve the measurement of detected, but low signal-to-noise (S/N) Balmer lines.

Of the 661 NB118 emission-line galaxy candidates in the SXDS, 386 were targeted with IMACS. Priority was given to sources likely to be intermediate redshift candidates based on their photometric redshifts (Furusawa et al. 2008), while galaxies with low photometric redshift ($z_{\text{phot}} < 0.7$) were used as slit-mask fillers. Sources which showed an NB118 excess at a significance lower than the 3σ cutoff were also used as fillers.

Overall, 225 (74) of the 3σ ($< 3\sigma$) selected sample observed with IMACS have spectroscopic redshift (z_{spec}) between 0.78 and 0.83, confirming that the narrowband photometric excess is due to H α emission. Note that the redshift range about $z = 0.8$ is slightly larger than expected. This is because not all light entering the narrowband filter is normally incident to the filter. As the angle of incidence increases, redshifts are biased blueward, increasing the expected redshift range.

Standard spectroscopic multi-object observational techniques were followed, and long-slit observations of spectrophotometric standards were obtained for flux calibration. Data reduction was performed using the dedicated software package called “COSMOS”, developed by the IMACS instrument team at Carnegie Observatories.¹² To obtain continuum-subtracted and absorption-corrected line flux measurements, the fluxed spectra were

fit with stellar population models. This fitting method, similar to that used for the SDSS (T04; Brinchmann et al. 2004), assumes that any galaxy star formation history (SFH) can be approximated by a sum of discrete bursts (simple stellar populations). Foreground extinction was corrected using the Schlegel et al. (1998) extinction map and the O’Donnell (1994) Milky Way extinction curve; for SXDS, average $E(B - V) = 0.03$.

In Table 1, we present the NEWFIRM photometric properties of the 299 spectroscopically confirmed H α emitters in the SXDS with IMACS. That is, these galaxies have $0.78 < z_{\text{spec}} < 0.83$. These data are used to compute the H α -based SFRs used in the analysis, as discussed in Section 3.2. Table 2 gives the IMACS spectroscopic fluxes for the strong rest-frame optical oxygen emission lines, as well as the Balmer lines (H β , H γ , and H δ). Active galactic nuclei (AGN) classification was performed by Momcheva et al. (2013) using a combination of methods, including UV variability, line widths, and emission-line diagnostics with the “Mass-Excitation” diagram (Juneau et al. 2011), to identify both broad- and narrow-line AGN. The 21 galaxies determined to have AGN are identified in Table 3, and are excluded from the remainder of the analysis, leaving a working sample of 278. For the remaining galaxies, the line fluxes are used to compute the gas-phase metallicities, as discussed in Section 3.3.

2.3. Multiwavelength Photometry

We use multiband photometry (NUV, u , B , V , R_C , i' , z' and J) as constraints in the SED fitting, which is later discussed in Section 3.1. The NUV photometry are based on deep (46 ks) *Galaxy Evolution Explorer* (GALEX, Martin et al. 2005; Morrissey et al. 2007) imaging of the SXDS fields (PI: S. Salim, GI6-005). At $z = 0.8$, the NUV band ($\lambda_C \approx 2300$ Å) samples the rest-frame far-UV. In addition to the dedicated “tile” (1.2-deg circular GALEX pointing) from this program, our NEWFIRM observations in the SXDS also partially overlap three shallower archival GALEX tiles with exposure times of 26–30 ks (Figure 1). The mean 5σ depth for the combined NUV imaging in the NEWFIRM fields is 25.3 mag (exposure time ~ 80 ks), which is ~ 1 mag shallower than the deepest GALEX NUV imaging (the Extended Groth Strip (EGS) field; Salim et al. 2009), with integration time of ≈ 260 ks.

Because sources are unresolved in GALEX at $z \approx 0.8$ (the GALEX FWHM is $\sim 5''$), we use PSF source extraction and photometry based on u -band priors, which improves upon the NUV photometry used in Momcheva et al. (2013). The u -band photometry is based on a (1 deg)² pointing with Canada-France-Hawaii Telescope (CFHT) Megacam (Boulade et al. 2003) with a 3σ depth in 2'' aperture of 27.0 mag (Foucaud, S., private communication)¹³. The prior-based photometry is performed using EMphot software (version 2.0; Vibert et al. 2009). Priors were limited to $u \leq 25$ mag in order to match the GALEX depth. We insert artificial sources to check that the fluxes can be recovered without any systematic errors, and find that not limiting the priors to $u \leq 25$ mag

¹² <http://code.obs.carnegiescience.edu/cosmos>.

¹³ Based on publicly available CFHT/Megacam data: <http://www1.cadc-ccda.hia-ihp.nrc-cnrc.gc.ca/en/>.

results in an underestimate of the NUV fluxes. Source extraction was performed separately in all four tiles (within 0.55 deg radius), and the results were averaged using photometric errors as weights. The resultant photometry represents the total galaxy light. NUV (rest-frame FUV) photometry was extracted in areas where u photometry was available, covering 75% of NEWFIRM fields (see Figure 1).

The optical photometry was obtained with Suprime-Cam (Miyazaki et al. 2002) as part of the Subaru Telescope Observatory Projects (Furusawa et al. 2008). The SXDS fields observed by NEWFIRM roughly correspond with the Suprime-Cam south, west, and north pointings (SXDS-S, SXDS-W, and SXDS-N; Figure 1). Subaru imaging is publicly available in five broadband filters to 3σ depths of $B = 28.4$, $V = 27.8$, $R_C = 27.7$, $i' = 27.7$, and $z' = 26.6$ mag. The Suprime-Cam data reduction and photometry are further described in Furusawa et al. (2008).

3. STELLAR MASS, SFR, AND GAS-PHASE METALLICITY MEASUREMENTS

We now turn our attention to calculating physical properties for the galaxies in the sample from the data presented in Section 2.

3.1. Stellar Masses

Following the methodology of Salim et al. (2007), we derive stellar masses by fitting SEDs to the eight-band¹⁴ photometry that span rest-frame UV and optical wavelengths, their photometric uncertainties, and spectroscopic redshift. Stellar masses have already been computed using SED fitting for this same sample for the nebular reddening analysis of Momcheva et al. (2013). The main improvement in the calculation performed here is the inclusion of u -band photometry, which in combination with the NUV photometry, provides more direct constraints on internal dust attenuation for galaxies at $z \sim 0.8$ via the rest-frame UV color. We give a brief summary of the modeling used, and refer readers to Salim et al. (2007, 2009) for further details.

We use total magnitudes determined within Kron apertures (MAG_AUTO from SExtractor; Bertin & Arnouts 1996), except in the NUV band, where PSF extracted magnitudes are used as described above. The SEDs are fit with a library of 45,000 Bruzual & Charlot (2003) stellar population synthesis models.¹⁵ The model libraries are built with a wide range of SFHs and metallicities, as described in Salim et al. (2007), and updated in da Cunha et al. (2008). Only models with formation ages lower than 6.8 Gyr, corresponding to the age of the universe at $z = 0.8$, are allowed. Each model is attenuated according to the prescription of Charlot & Fall (2000), with randomly sampled values of both the total optical depth and the fraction of the total optical depth due to attenuation by the ambient ISM. The dust attenuation in the SED fitting is mainly constrained by the UV slope, which gets steeper with increasing attenuation (Calzetti et al. 1994). However, differences in the SFHs can produce significant scatter between the UV slope and dust

attenuation (e.g., Kong et al. 2004). This is generally overcome in our modeling because the near-IR and optical data help to constrain the age. Intergalactic reddening is included via the prescription of Madau (1995), and a Chabrier IMF is assumed. The spectroscopic redshift provides the luminosity distance, which allows the apparent model quantities to be scaled to absolute values. We use 0.025 mag calibration errors in all bands, including the NUV photometry, yielding approximately unit Gaussian residuals with respect to model photometry. An offset of +0.12 mag in R_C -band photometry is applied in order to correct the rest-frame 3700 Å discrepancy with the stellar synthesis models (Salim et al. 2009).

For each galaxy the observed fluxes are compared to those in the model library, and the goodness of fit (χ^2) determines the probability weight of a given model. The average of the probability distribution of each fitted parameter is the nominal estimate of that parameter and its width is used to estimate the errors and confidence intervals. The majority of galaxies in the sample are well fit and the median χ^2 per degree of freedom of the best-fitting SED models is close to unity. In the target redshift range ($0.77 < z < 0.83$), 23 objects are excluded from the sample due to poor fits (i.e., if χ^2_{ν} of the best-fitting model is >10), leaving 255. Another 118 non-AGN objects lack u -band (rest-frame FUV) photometry.

The stellar masses and their uncertainties are given in Table 3. The uncertainties include errors from input photometry and parameter degeneracy (e.g., with respect to SFH and dust). Additional systematic uncertainties may arise from the models themselves and the choice of IMF (e.g., Maraston 2005; Conroy et al. 2009; Taylor et al. 2011).

The distribution of derived stellar masses and their uncertainties are shown in Figure 2. AGN are included in the stellar mass sample, but 25 sources (2 are AGN) have poor SED fits and are thus excluded from the original sample size of 299, leaving 274 sources. The mean (median) of the sample is $10^{9.9}$ ($10^{9.8}$) M_{\odot} , with an average uncertainty of $\sigma = 0.11$ dex. There are a few galaxies with masses as low as $10^{8.9}$ M_{\odot} , and as high as $10^{11.8}$ M_{\odot} .

3.2. Star Formation Rates

The SFRs used in our analysis are measured using two independent methods that are sensitive to different timescales of star formation. First, as with stellar masses, we use the SED fitting to provide a measurement of the recent SFR. The rest-frame FUV continuum provides the main constraint on the SFR in the SED modeling, since it primarily originates from the photospheres of O- through late B-type stars ($M \gtrsim 3 M_{\odot}$), and measures star formation averaged over a timescale of ~ 100 Myr (e.g., Kennicutt 1998; Lee et al. 2011). The SED modeling also provides constraints on the attenuation by dust internal to the galaxy, and thus yields dust-corrected SFRs.

The distribution of SED-modeled SFRs and their uncertainties are shown in Figure 3. As with Figure 2, the 21 AGN are included in the sample. However, 125 sources lacked u -band observations, leaving a sample size of 174. The SED-modeled dust-corrected SFRs have a

¹⁴ Up to 8 bands are available. Coverage in the u -band is available for 160 of 278 galaxies, or 57.6% of our sample (see Figure 1).

¹⁵ Derived using MAGPHYS package available at <http://www.iap.fr/magphys/>.

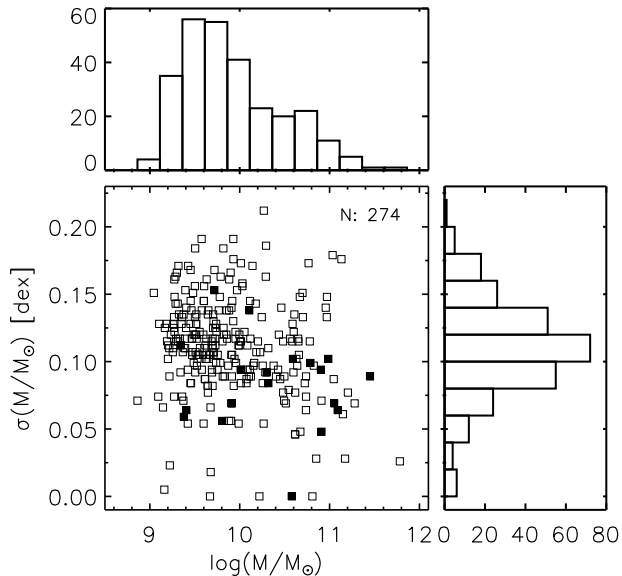


FIG. 2.— Top: Distribution of stellar masses. Center: Measurement error in stellar mass vs. stellar mass (filled points mark AGN). Right: Distribution of stellar mass uncertainties.

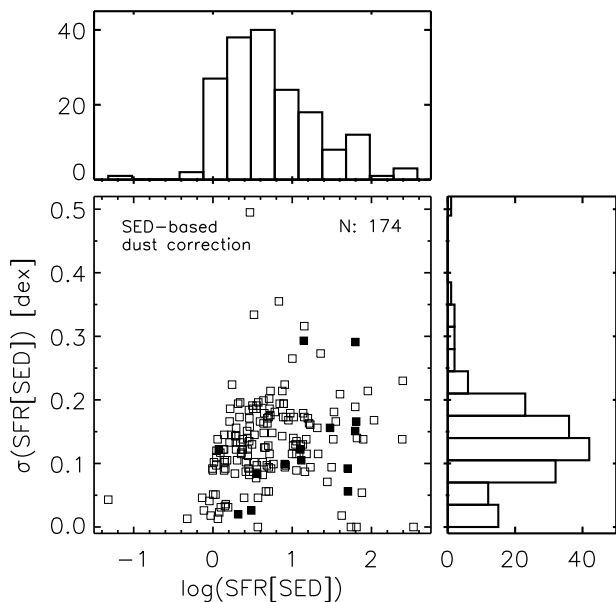


FIG. 3.— Top: Distribution of dust-corrected UV-based (i.e., from SED fitting) SFRs. Center: Measurement error in SFR vs. SFR (filled points mark AGN). Right: Distribution of SFR uncertainties.

mean (median) of $10^{0.72}$ ($10^{0.64}$) $M_{\odot} \text{ yr}^{-1}$, ranging from $10^{-1.3}$ to $10^{2.5}$ $M_{\odot} \text{ yr}^{-1}$ with an average uncertainty of $\sigma = 0.13$ dex.

Second, we compute SFRs using the $H\alpha$ luminosities derived from the NEWFIRM narrowband photometry. $H\alpha$ nebular emission directly arises from the recombination of H II gas ionized by the most massive O- and early B-type stars ($M \gtrsim 10 M_{\odot}$), and therefore traces star formation over the lifetimes of these stars, which is on the order of a few million years (e.g., Kennicutt 1998). The $H\alpha$ SFRs are computed as follows. $H\alpha + [N \text{ II}]$ fluxes are first calculated from the J and NB118 photometry, as described in Ly et al. (2011a). The fluxes are converted to luminosities using the spectroscopic redshifts. Cor-

rections must then be applied for: (1) the contribution of the $[N \text{ II}] \lambda\lambda 6548, 6583^{16}$ lines, and (2) attenuation by dust internal to the galaxy.

N II contamination. The NB118 bandpass is wide enough to include flux from the $[N \text{ II}]$ emission lines for $H\alpha$ excess emitters. To correct for this, we estimate the $[N \text{ II}]/H\alpha$ ratio with the R_{23} flux ratio (Pagel et al. 1979),

$$R_{23} \equiv \frac{[\text{O II}] \lambda\lambda 3726, 3729 + [\text{O III}] \lambda\lambda 4959, 5007}{H\beta}. \quad (1)$$

We follow this empirical approach since both the $[N \text{ II}] \lambda 6583/H\alpha$ and R_{23} are often used to determine metallicity (e.g., Pettini & Pagel 2004; Kewley & Ellison 2008, see Section 3.3 for further discussion), so a tight correlation is expected. To calibrate this method, we begin with the largest spectroscopic sample, the SDSS MPA-JHU Data Release 7 (DR7; Abazajian et al. 2009) catalog.¹⁷ We require that $[\text{O III}] \lambda 5007$, $H\beta$, $H\alpha$, and both the $[\text{O II}]$ lines to be detected at a minimum of 3σ . This restriction limits the DR7 sample to 165,622 galaxies. We do not apply a restriction on $[N \text{ II}]$, as the line is intrinsically weak, so a required detection will bias the correction against metal-poor galaxies. We then use the Baldwin et al. (1981) “BPT” diagnostic diagram to exclude AGN. Here we adopt the Kauffmann et al. (2003) selection for star-forming galaxies, which limits the sample further to 140,101 galaxies. We illustrate the $[N \text{ II}] \lambda 6583/H\alpha$ and R_{23} ratios for these galaxies in Figure 4(a). It can be seen that the two ratios are well-correlated with $[N \text{ II}] \lambda 6583/H\alpha$ reaching a maximum of ≈ 0.4 . To correct for $[N \text{ II}]/H\alpha$, we use the mean values, which are shown as solid filled squares in Figure 4(a). We also factor in the dispersion of this correlation, which is typically $\sigma \lesssim 0.1$ dex. Since the $[N \text{ II}] \lambda 6583$ is the stronger of the two $[N \text{ II}]$ lines, we also assume $\lambda 6583/\lambda 6548 = 3$. For our sample, the $[N \text{ II}]$ correction is between $\log([N \text{ II}]/H\alpha) = -1.36$ and -0.29 , with an average of -0.55 .

We note that for a subset of our galaxies ($N = 168$), the emission lines used for computing R_{23} are not well measured ($< 3\sigma$). To correct these galaxies for their $[N \text{ II}]$ contamination, we follow previous efforts that use the $H\alpha + [N \text{ II}]$ equivalent width (EW). This method was first implemented by Villar et al. (2008). One problem with the previous calibration was the inclusion of AGN and LINERs (Heckman 1980), which significantly biased the $[N \text{ II}]$ correction. Here, we therefore reproduce the relation of Villar et al. (2008) with only star-forming galaxies. We emphasize that the AGN contribution is low in our sample, and we have utilized various empirical methods to identify and remove AGN from our sample (see Section 2.2). The EW correlation of $[N \text{ II}]/H\alpha$ is illustrated in Figure 4(b).

We find that both the R_{23} - and EW-based methods yield fairly consistent $[N \text{ II}]$ corrections for the sample with R_{23} emission lines ($[\text{O II}]$, $[\text{O III}]$, and $H\beta$) detected at $\geq 3\sigma$; the EW-based $[N \text{ II}]$ corrections are higher than the R_{23} $[N \text{ II}]$ corrections by ~ 0.05 dex, with a dispersion of ~ 0.03 dex. We also find that the EW approach suffers from greater dispersion. This is not a surprise since

¹⁶ Hereafter, “[N II]” refers to the sum of the two nitrogen emission lines, unless otherwise indicated.

¹⁷ <http://www.mpa-garching.mpg.de/SDSS/DR7/>.

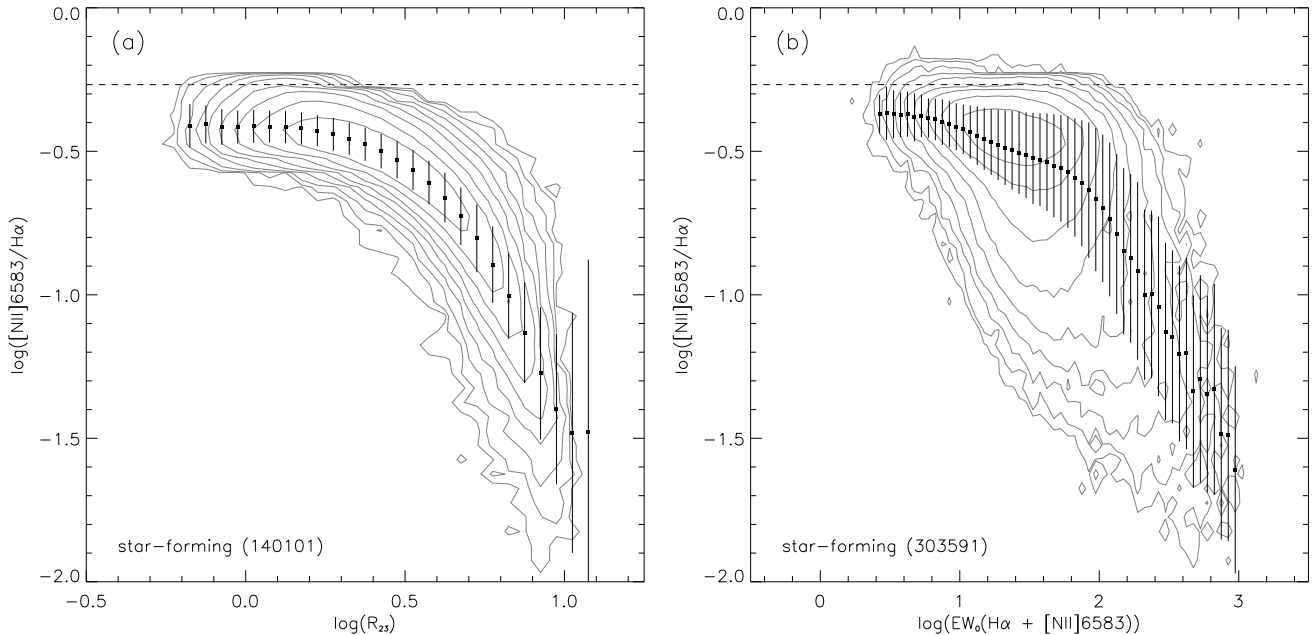


FIG. 4.— $[\text{N II}] \lambda 6583/\text{H}\alpha$ as a function of (a) $\log(R_{23})$ and (b) $\log(\text{EW}_o(\text{H}\alpha + [\text{N II}] \lambda 6583))$ from the SDSS DR7 sample. Contour levels are on a logarithmic scale. The average and $1\text{-}\sigma$ dispersion are shown by the filled squares and errorbars. The dashed lines refer to the maximum $[\text{N II}] \lambda 6583/\text{H}\alpha$ ratio of 0.54 for star-forming galaxies (Kennicutt et al. 2008). These correlations are used to remove contamination of $[\text{N II}]$ in our NB118 bandpass to yield $\text{H}\alpha$ -based SFRs.

a tight correlation is not expected between the specific SFR (SFR per unit stellar mass; SFR/M_*) of galaxies, as measured from the $\text{H}\alpha$ EW, and their metallicity, as measured from $[\text{N II}] \lambda 6583/\text{H}\alpha$. Since previous studies (e.g., Sobral et al. 2009) used the Villar et al. (2008) calibration, we note that their $\text{H}\alpha$ measurements are underestimated due to a systematically larger correction for $[\text{N II}]$.

We note that adopting local measurements to correct for $[\text{N II}]$ contribution in the NB filter has its limitations, particularly since a few studies of strongly star-forming galaxies have seen nitrogen abundance enhancements relative to oxygen (Amorín et al. 2010; Masters et al. 2014). This result is not too surprising since nitrogen has a secondary production source. Given this recent evidence, it is therefore likely that we are underestimating the $[\text{N II}]$ contribution, and thus overestimating the $\text{H}\alpha$ flux. For the purpose of our analyses, we defer on this issue, as we plan to revisit it in future work.

Dust attenuation. The $\text{H}\alpha$ emission-line luminosities are corrected for dust reddening in two ways: using both the Balmer decrement ($\text{H}\gamma/\text{H}\beta$) from spectroscopy and the estimate of nebular attenuation from SED fitting. Since the $\text{H}\gamma$ line is intrinsically weak for much of our sample, the majority of the following analysis is based on dereddening based on SED-derived attenuation.

Finally, we use the prescription of Kennicutt (1998) to derive SFRs from $\text{H}\alpha$ luminosities. We divide by a factor of 1.8 to convert the SFRs from a Salpeter (1955) to a Chabrier IMF. The distribution of dust-corrected $\text{H}\alpha$ -based SFR (corrected using SED results and the extinction formalism of Charlot & Fall 2000) is shown in Figure 5. AGN are again included in this sample; however, 90 sources with $< 3\sigma$ NB118 excess flux are removed and 8 more sources without SED fits, leaving a sample size of 201. The mean (median) of the sample is $10^{0.74}$ ($10^{0.67}$) $M_\odot \text{ yr}^{-1}$, and the average uncertainty is $\sigma = 0.33$ dex.

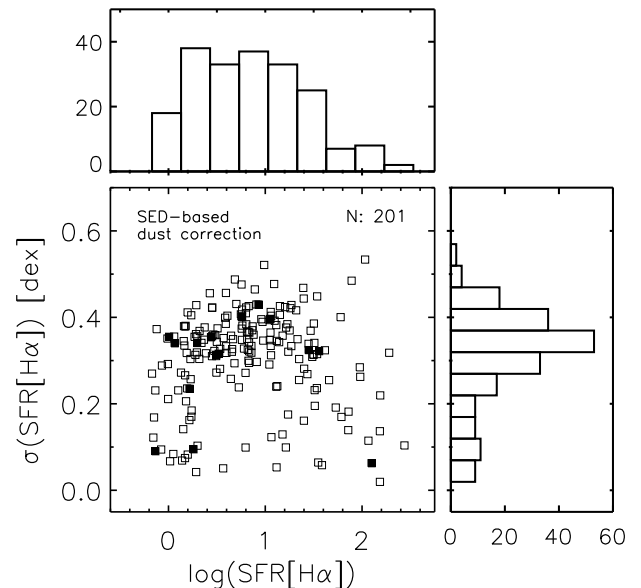


FIG. 5.— Top: Distribution of dust-corrected $\text{H}\alpha$ -based SFRs. Center: Measurement error in SFR vs. SFR (filled points mark AGN). Right: Distribution of SFR uncertainties.

There are a few galaxies with SFRs as low as $10^{-0.4} M_\odot \text{ yr}^{-1}$, and as high as $10^{2.4} M_\odot \text{ yr}^{-1}$. SFRs based on the SED-fitting and $\text{H}\alpha$ luminosities are reported in Table 3.

3.3. Gas-Phase Metallicities

Various metallicity calibrations have been developed for over two decades, yet the absolute metallicity scale is still uncertain, as demonstrated by Kewley & Ellison (2008). In general, oxygen abundance is used as a proxy for global gas-phase metallicity and expressed as a dimensionless quantity, $Z \equiv 12 + \log(\text{O}/\text{H})$. On this scale, $Z_\odot = 8.76$ (Caffau et al. 2011).

The “direct” method of determining Z is to measure

the ratio of the weak [O III] $\lambda 4363$ line to a lower excitation line, which gives an estimate of the electron temperature T_e that is inversely related to the gas metallicity. While efforts have measured direct metal abundances (e.g., Kakazu et al. 2007; Brown et al. 2008; Hu et al. 2009; Berg et al. 2012; Ly et al. 2014), [O III] $\lambda 4363$ is very difficult to robustly detect. As a result, strong-line calibrations based on the empirical relationship between T_e -based metallicities and strong-line ratios (e.g., R_{23}) have been developed (e.g., Nagao et al. 2006). Other calibrations use population synthesis and photoionization models to calculate theoretical strong-line ratios for various input metallicities (e.g., Zaritsky et al. 1994; McGaugh 1991; Kobulnicky & Kewley 2004, hereafter Z94, M91 and KK04, respectively). Finally, Bayesian fitting has been used to find the photoionization model that best explains the observed fluxes of all the most prominent rest-frame optical emission lines (T04).

Metallicities determined from the direct and empirical methods based on T_e have been shown to be systematically lower than those determined from the theoretical methods based on photoionization models (Kewley & Ellison 2008). While this discrepancy is unresolved, problems with photoionization models, or temperature gradients/inhomogeneities may cause T_e methods to underestimate true metallicities (Kewley & Ellison 2008). Also, recent efforts have suggested that non-Maxwellian energy distributions in the ISM may be the culprit for many systematic differences (Nicholls et al. 2012, 2013; Dopita et al. 2013). Regardless of what is responsible for the discrepancies, it is clear that a consistent use of a single metallicity calibration is required to obtain a self-consistent M_\star - Z -SFR relation and to study its evolution.

For completeness and to aid direct comparisons in future work, we have determined metallicity using multiple calibrations. In Tables 4 and 5, we present these metallicities, calculated using the nebular emission lines reported in Table 2, with dust attenuation correction derived from the SED fitting and the Balmer decrement ($H\gamma/H\beta$), respectively. The transformation from observed line ratios to gas metallicity is summarized in the Appendix of Kewley & Ellison (2008).

Note that several calibrations rely on the R_{23} line ratio (Pagel et al. 1979). The M91 and KK04 calibrations also use the O_{32} line ratio: $O_{32} \equiv [\text{O III}] \lambda\lambda 4959,5007 / [\text{O II}] \lambda\lambda 3726,3729$, as an estimate of the ionization state of the gas. This measurement helps to resolve the degeneracy between ionization state and metallicity (see e.g., Figures 3 and 12 of KK04 and M91, respectively). For this reason, we choose to use the M91 calibration in analyzing the M_\star - Z relation and comparing our work with previous results (Section 4.3). For instances where a different metallicity calibration was used, we converted to M91-based metallicity using the relations defined in Table 3 of Kewley & Ellison (2008).

For the M_\star - Z -SFR relation (Section 4.4), previous studies have used the T04 calibration rather than M91 (e.g., Lar10; Yat12). To aid in direct comparisons, we analyze the M_\star - Z -SFR relation using metallicities scaled with respect to the photoionization models derived by T04; however, supplementary results using M91 metallicities are provided. When computing T04-based metallicities, we use the following empirical R_{23} - Z relation

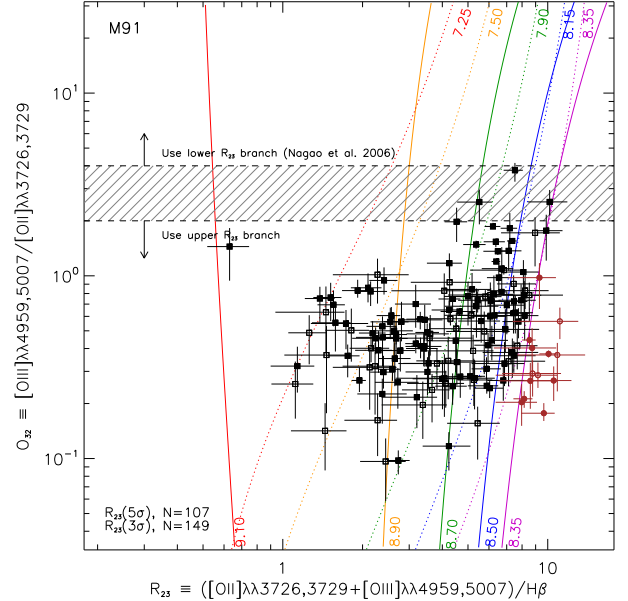


FIG. 6.— Metallicity-sensitive (R_{23}) and ionization parameter-sensitive (O_{32}) emission-line ratios for the $z = 0.8$ NewH α sample. We limit the sample to galaxies that are not AGN, as well as, galaxies that have reliable SED fits (i.e., these galaxies are later used to construct the M_\star - Z relation). Filled points show the $R_{23}(5\sigma)$ sample with additional sources from the $R_{23}(3\sigma)$ sample as unfilled points. Circles (brown in the color version) indicate galaxies with high R_{23} values such that the upper branch metallicity is less than the lower branch metallicity. Photoionization models from M91 are overlaid in colors for metallicities between $12 + \log(\text{O}/\text{H}) = 7.25$ and $12 + \log(\text{O}/\text{H}) = 9.1$. Solid (dotted) curves are for metallicities on the upper (lower) R_{23} branch. Based on the empirical relations of Nagao et al. (2006), the dashed horizontal lines distinguish between upper and lower R_{23} branch with a region of ambiguity (shaded). Given these R_{23} and O_{32} values, we adopt the upper branch.

provided by T04:

$$12 + \log(\text{O}/\text{H}) = 9.185 - 0.313x - 0.264x^2 - 0.321x^3, \quad (2)$$

where $x \equiv \log(R_{23})$.

The relationship between R_{23} and O/H is double-valued, and so a given value of R_{23} may correspond to low or high metallicity (“lower branch” and “upper branch”, respectively), and additional line ratios are needed to break the degeneracy. One such ratio is $[\text{N II}] \lambda 6583 / \text{H}\alpha$ (Kewley & Ellison 2008); however, this requires medium-resolution infrared spectroscopy for our galaxies, which we currently do not have. An alternative line ratio that can distinguish between the upper and lower branch is the O_{32} ratio (e.g., Nagao et al. 2006; Maiolino et al. 2008). We illustrate the dust-corrected R_{23} and O_{32} ratios in Figure 6, which demonstrates that the majority of our sources follow the upper R_{23} branch. There are a few sources with line ratios such that the choice in upper or lower branch is ambiguous (shaded region in Figure 6). Adopting either branch does not impact the primary results of our M_\star - Z -(SFR) analysis.

The distribution of M91 upper-branch metallicities and their errors (corrected using SED results and the extinction formalism of Charlot & Fall 2000) are shown in Figure 7. AGN are included in this figure, but the sample is restricted to the 137 sources where [O II], [O III], and H β are all detected at $\geq 5\sigma$. We refer to this sample as “ $R_{23}(5\sigma)$ ” for brevity. This naming convention should

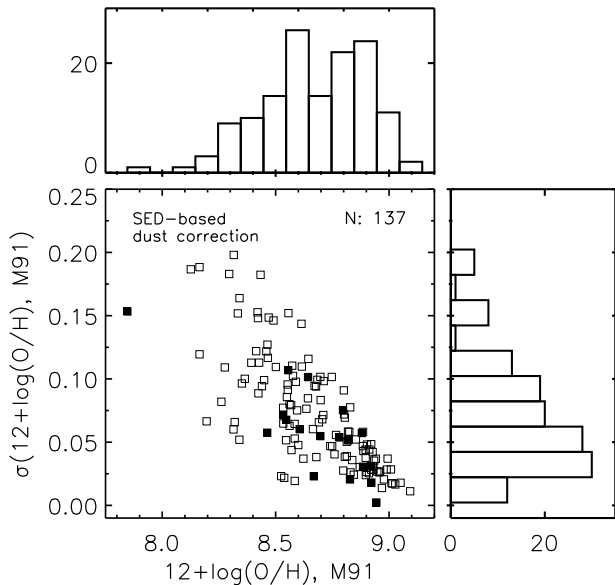


FIG. 7.— Top: Distribution of **M91** upper-branch metallicities. Center: Measurement error in **M91** upper-branch metallicity vs. **M91** upper-branch metallicity (filled points mark AGN). Right: Distribution of **M91** upper-branch metallicities uncertainties. Only galaxies with [O II], [O III], and H β $> 5\sigma$ are shown here.

not be interpreted as a 5σ detection limit on R_{23} , rather on the emission lines for the line ratio. A larger sample of 187 galaxies, selected at 3σ , is also constructed, hereafter “ $R_{23}(3\sigma)$ ”. The mean (median) of the sample is $12 + \log(\text{O}/\text{H}) = 8.67$ (8.68), and the average uncertainty is 0.07 dex. There are a few galaxies with metallicities as low as 7.85, and as high as 9.09.

4. RESULTS AND ANALYSIS

In our analysis, we first compare the two measures of the SFR computed above, those based upon the H α flux, and those derived from the SED modeling of rest-frame FUV to R -band photometry, as a check on the relative reliability of the methods (Section 4.1). We then compare the stellar mass, SFR, and metallicity measurements for the NewH α sample to other measurements in the literature, as studied within the framework of the star-formation sequence (Section 4.2) and the M_\star - Z relation (Section 4.3). Finally, we combine these two relations to investigate the M_\star - Z -SFR relation at $z \approx 0.8$ (Section 4.4).

In each analysis, we use various combinations of sample restrictions. For convenience, the sample cuts used and the subsample sizes are compiled in Table 6.

4.1. Comparison of SFR Tracers

In order to compare SFR measurements from different tracers, we do not consider AGN. From the remaining sample of 278 galaxies, only those with an NB118 excess line flux $\geq 3\sigma$ and good SED fits ($\chi_\nu^2 < 10$) with u -band photometry are included, leaving a sample size of 114.

We illustrate the SED- and H α -based SFRs in Figure 8. Since the SED modeling constrains the dust attenuation, we also correct the H α measurements with the SED-based dust extinction estimates for each of our galaxies, $A(\text{H}\alpha) = 0.96\tau_V$. We find that the SED-based SFRs are higher than the H α -based SFRs by ~ 0.09 dex in the median, well within the scatter of 0.24 dex. In addition,

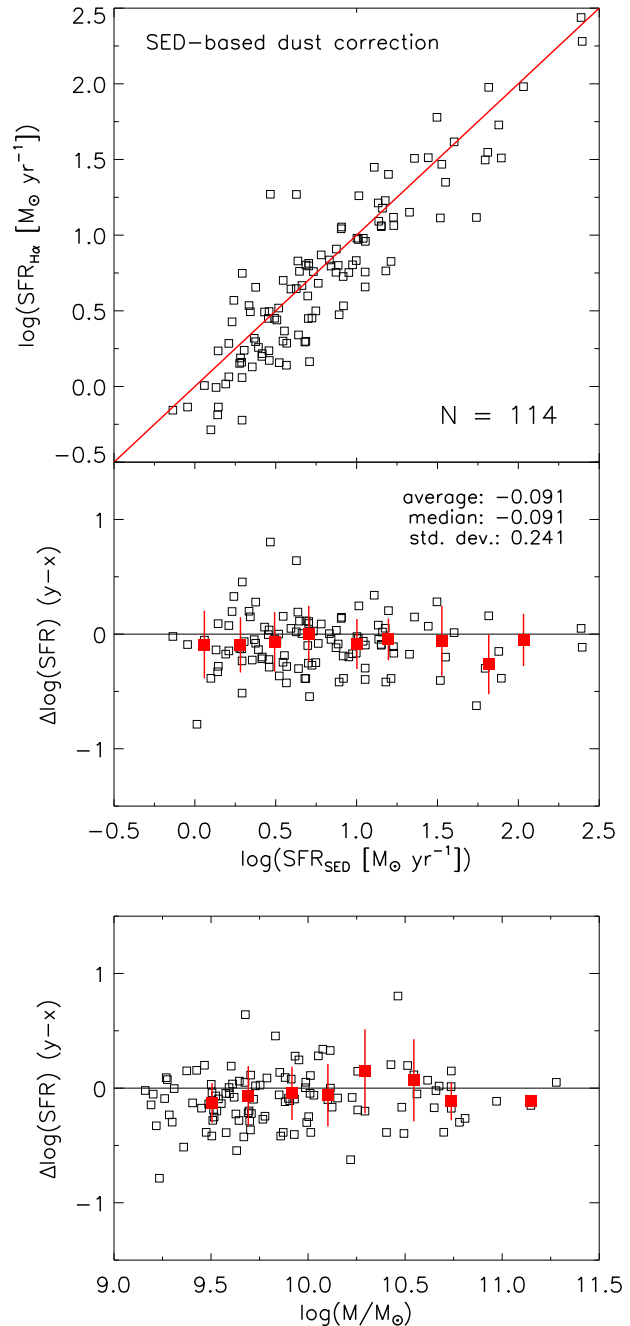


FIG. 8.— Comparison of SED-based and H α -based SFRs, both corrected for extinction using SED results and the extinction law of [Charlot & Fall \(2000\)](#). Solid lines (red in online version) indicate one-to-one. Filled points (red in online version) in the middle and bottom panels indicate median values within SED-based SFR and mass bins, respectively, while the errorbars represent the 1σ scatter in the residuals.

we find that there is no mass dependence of the residual, and that these two measurements even agree at high SFRs ($\gtrsim 100 M_\odot \text{ yr}^{-1}$). We note that similar results on the SFR comparison are found using Balmer decrements (H γ /H β , obtained from spectroscopy; Section 2.2) for dust attenuation. However, only 27 galaxies have deep enough spectra (H γ SN ≥ 10) to yield individual decrements that are reliable at $\Delta(E_{B-V}) = 0.2$ mag.

These results are roughly consistent with other comparisons of SFR tracers at similar or lower redshifts. For

example, Villar et al. (2011) compared H α - and FUV-based SFRs at $z \sim 0.84$. While Villar et al. (2011) found that observed H α -based SFRs were systematically higher than FUV-based SFRs, they also found that correcting for dust caused the two SFR tracers to agree at the level of 0.05 dex with a dispersion of ≈ 0.2 – 0.25 dex. Also, Ly et al. (2012) have compared SED-based SFRs against H α SFRs in $z = 0.4$ – 0.5 H α -selected galaxies, and also find good agreement with low dispersion (~ 0.2 dex) with corrections for dust attenuation based on estimates from SED fits.

Since the H α -based SFRs are more robust to the effects of dust attenuation compared to the SED-based SFRs, we hereafter use H α SFRs, corrected for dust attenuation determined from SED fitting.

4.2. The Star-Formation Sequence

The relation between SFR and M_* , commonly referred to as the “star-forming sequence” (Salim et al. 2007) or the “main sequence of star-forming galaxies” (Noeske et al. 2007), has been well studied at low (e.g., Brinchmann et al. 2004; Salim et al. 2007) and intermediate (e.g., Noeske et al. 2007; Villar et al. 2011; Whitaker et al. 2012) redshifts, with general agreement among different literature results. It manifests as a relatively tight ($\sigma \sim 0.3$ dex) relationship usually parameterized as $\text{SFR} \propto M_*^\beta$, although some recent works have suggested that the M_* –SFR relation is not a simple power law at high redshifts (Whitaker et al. 2014). The evolution of the form of the M_* –SFR relation over cosmic time can provide constraints on the characteristic star formation history of galaxies and the significance of episodic bursts of activity in building up the stellar mass (e.g., Noeske et al. 2007). In this section, we compare our NewH α results with other studies at $z \sim 0.8$.

The top panel in Figure 9 plots the NewH α M_* –SFR data and a least-squares linear fit to our 3σ sample (i.e., NB118 excess flux $\geq 3\sigma$). We find the resulting best-fit power law to be:

$$\log\left(\frac{\text{SFR}_{\text{H}\alpha}}{M_\odot \text{ yr}^{-1}}\right) = (0.75 \pm 0.07) \log\left(\frac{M_*}{M_\odot}\right) - (6.73 \pm 0.67). \quad (3)$$

The bottom panel compares this linear fit (red line with average measured scatter of 0.47 dex) against literature star-formation sequences and estimated intrinsic scatters determined by Noeske et al. (2007) and Elbaz et al. (2007) (compiled by Dutton et al. 2010), as well as Villar et al. (2011) and Whitaker et al. (2012). The medians of the NewH α data binned by mass (black points) are provided in Table 7. When necessary, stellar masses and SFRs have been converted to a Chabrier IMF from a Salpeter (1955) IMF by dividing by 1.8 (e.g. González et al. 2010). The local star-formation sequence (Salim et al. 2007; Salim & Lee 2012, solid orange band) has also been plotted for comparison.

Despite small variations, the NewH α M_* –SFR relation and literature relations at similar redshift are all systematically higher than the local relation (Salim et al. 2007). This is consistent with studies that generally find that galaxies at higher redshift tend to have higher SFRs at fixed stellar mass compared to galaxies in the local universe.

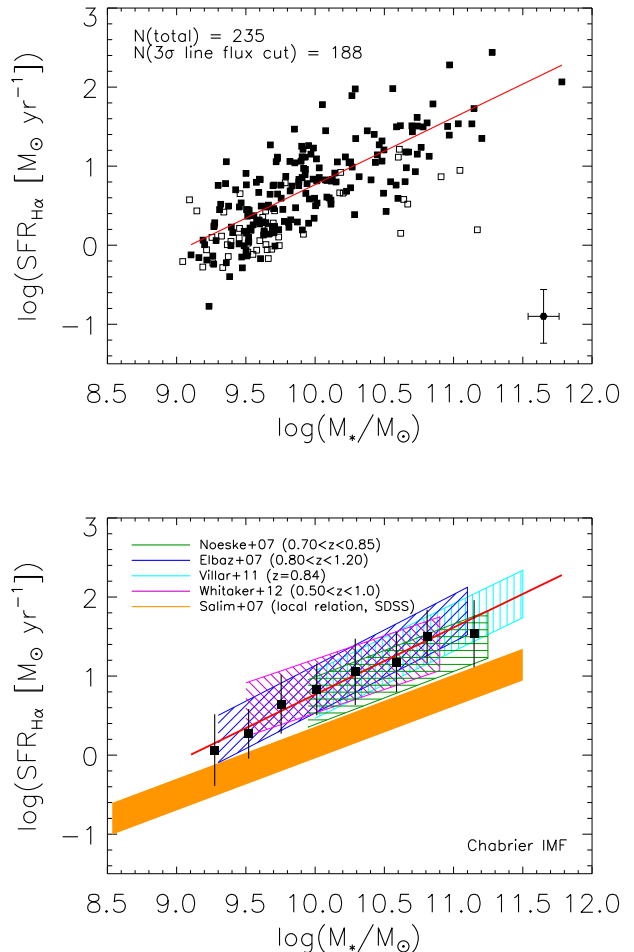


FIG. 9.— Top: Comparison of the NewH α M_* –SFR data (black squares) with a linear fit (solid line, red in the online version). Filled (open) squares mark sources for which the NB118 excess flux is $> 3\sigma$ ($< 3\sigma$); the linear fit uses the $> 3\sigma$ points. Bottom: Comparison of the NewH α M_* –SFR linear relation with literature relations. Black points denote medians of NewH α data binned by mass, with errorbars representing standard deviations. Note that the linear fit covers the entire mass range, while the black points only mark mass bins with more than one data point.

As noted in Section 3.1, the NewH α survey covers a stellar mass range of $10^{8.9}$ to $10^{11.8} M_\odot$ with an average mass of $10^{9.9} M_\odot$. At similar redshifts, Noeske et al. (2007) investigated a limited stellar mass range of $\sim 10^{10.0}$ – $10^{11.3} M_\odot$, while Elbaz et al. (2007) covered a mass range of $\sim 10^{9.3}$ – $10^{11.1} M_\odot$ and Whitaker et al. (2012) covered a mass range of $\sim 10^{9.5}$ – $10^{11.0} M_\odot$. It is notable that despite varying mass ranges, sample selection methods and SFR determinations, Noeske et al. (2007), Elbaz et al. (2007), and Whitaker et al. (2012) each find best-fit power-law relationships that are all fairly consistent with each other. The NewH α fit also agrees well with these relations, with some minor variations.

The Noeske et al. (2007) relation (green band horizontally cross-hatched) is $\log(\text{SFR}/(M_\odot \text{ yr}^{-1})) = (0.67 \pm 0.08) \log(M_*/M_\odot) - (5.96 \pm 0.78)$ (using the relation compiled by Dutton et al. 2010). It therefore has a shallower slope than the NewH α relation. However, the NewH α fit lies within the scatter of the Noeske et al. (2007) relation (~ 0.3 dex). The slope of the Elbaz et

al. (2007) relation (blue band cross-hatched diagonally upwards right) is 0.90, rising more steeply than our fit, but its intercept is much lower (-8.17 , again using the relation compiled by Dutton et al. 2010). This could simply be due to the fact that Elbaz et al. (2007) study galaxies at a slightly higher median redshift and wider redshift range ($0.80 < z < 1.20$). Despite this offset, the NewH α fit is within the scatter of the Elbaz et al. (2007) relation (~ 0.3 dex). On the other hand, the Whitaker et al. (2012) relation (pink band cross-hatched diagonally downwards right) has a shallower slope, with a functional form of $\log(\text{SFR}/(M_{\odot} \text{ yr}^{-1})) = 0.6 \log(M_{\star}/M_{\odot}) - 5.09$ at $z \sim 0.8$ (uncertainties not given). This is more likely due to incompleteness at masses below $10^{9.8} M_{\odot}$, as shown in Figure 1 of Whitaker et al. (2012). Above this mass-completeness limit, the NewH α relation is well within the scatter derived by Whitaker et al. (2012) (~ 0.34 dex).

Villar et al. (2011) use a narrowband selection similar to that used in the NewH α survey and study 153 H α emitters at $z \sim 0.84$ in the EGS and GOODS-North fields. This survey covered a mass range of $10^{10.0-10^{11.5}} M_{\odot}$. Villar et al. (2011) do not provide a functional form for their M_{\star} -SFR relation; however, when we calculated our own least-squares linear fit for the Villar et al. (2011) data points (light-blue band cross-hatched vertically), we found a fit of $\log(\text{SFR}/(M_{\odot} \text{ yr}^{-1})) = (0.51 \pm 0.15) \log(M_{\star}/M_{\odot}) - (4.11 \pm 1.61)$. Although both the Villar et al. (2011) slope and intercept are systematically lower than the NewH α slope and intercept, the NewH α relation is consistent with the Villar et al. (2011) relation at overlapping mass bins (i.e., above $10^{10} M_{\odot}$).

Since our sample is selected by H α emission, we expected our galaxies to be biased toward higher SFRs, which would result in a M_{\star} -SFR relation systematically higher than those found using mass- and luminosity-limited surveys. However, that is not the case, as demonstrated in Figure 9. This is because our H α survey is reasonably deep with a 50% completeness limit that corresponds to an observed H α SFR of $0.4 M_{\odot} \text{ yr}^{-1}$ (Ly et al. 2011a). Our greater observational limitation is on the amount of excess flux (i.e., the H α EW) that we can measure, which corresponds to the specific SFR. Previous Monte Carlo simulations suggest that the low-EW population that we are missing amounts to $\approx 20\%$ at high masses and increases to 50% near our sensitivity limits (Ly et al. 2011a). These selection limitations, however, do not appear to bias our sample any more than mass- and luminosity-limited surveys. We note that Henry et al. (2013b), who used a sample of emission-line galaxies selected from grism spectroscopy, have also found good agreement with other M_{\star} -SFR studies.

We also note that despite the consistency between the NewH α data with literature M_{\star} -SFR relations, the upper panel of Figure 9 shows that a line does not perfectly fit the NewH α M_{\star} -SFR data. This may be evidence that the M_{\star} -SFR relation is not a simple power law at higher redshifts, as recently suggested by Whitaker et al. (2014). However, the observed curvature in the M_{\star} -SFR relation may be the result of selection bias (i.e., missing more dust-obscured galaxies) or because the dust attenuation correction is underestimated.

4.3. The Mass–Metallicity Relation

Several previous studies have examined the M_{\star} - Z relation at $z \sim 0.8$. However, these studies used samples with different ranges of stellar mass and metallicity, as well as, different treatments of systematic effects like dust extinction (for some analysis, see Moustakas et al. 2011; Zahid et al. 2011). We therefore aim to supplement and compare previous results with our large spectroscopically-selected NewH α sample.

As before, we fit the NewH α data with a linear relation using least-squares. We plot both $R_{23}(3\sigma)$ and $R_{23}(5\sigma)$ metallicity detections, but for the linear fit, we use the $R_{23}(5\sigma)$ sample. Using the 5σ cut did not significantly bias the sample, as the top panel of Figure 10 shows. We also remove 9 sources for which the calculated upper-branch metallicity is lower than the lower-branch metallicity, leaving a 5σ sample size of 98¹⁸. Using the M91 metallicity calibration, we find the resulting linear relation to be

$$12 + \log(\text{O}/\text{H}) = (0.25 \pm 0.03) \log\left(\frac{M_{\star}}{M_{\odot}}\right) + (6.23 \pm 0.33), \quad (4)$$

with an intrinsic scatter of 0.16 dex.

The top plot in Figure 10 shows this linear relation, while the bottom plot compares this linear fit to other M_{\star} - Z relation determinations at similar redshifts. The means of the NewH α data binned by mass are also plotted, and their values are provided in Table 7. All stellar masses are converted to be consistent with a Chabrier IMF, and all metallicities are made to be consistent with the M91 upper-branch calibration using the conversions in Kewley & Ellison (2008).

We find that the NewH α M_{\star} - Z relation is generally consistent with literature relations, and all these relations at higher redshifts are systematically lower than the local M_{\star} - Z relation of T04 (dark blue solid curved line), once it has been converted to the same metallicity calibration.¹⁹ This result is consistent with previous studies of metallicity evolution with redshift.

Savaglio et al. (2005) used galaxies from the Gemini Deep Deep Survey and the Canada France Redshift Survey to investigate the M_{\star} - Z relation at $z = 0.4-0.98$. A final sample of 56 galaxies was selected by the existence of rest-frame optical emission lines with a 3σ detection limit of $(0.6-3.2) \times 10^{-18} \text{ erg s}^{-1} \text{ cm}^{-2}$. Metallicities were calculated using the R_{23} line flux ratio and KK04 calibration. The pink dashed-triple dot line in Figure 10 marks the Savaglio et al. (2005) linear bisector fit, which does not agree with the NewH α data (nor other higher redshift studies). However, the small sample size, lack of selection criteria (i.e., no color selection, no S/N threshold for the R_{23} emission lines), and different fitting method for the Savaglio et al. (2005) data all prevent us from directly comparing the two relations.

Lamareille et al. (2009) examined two subsets of ~ 3000 $z = 0.7-0.9$ galaxies from the VIMOS VLT Deep

¹⁸ These 9 galaxies have R_{23} values that are higher than the limit of many of these metallicity calibrations (see Section 3.3 and Figure 6). Zahid et al. (2011) removed such galaxies as well, believing them to be AGN.

¹⁹ Again, we use the Kewley & Ellison (2008) relation to transform to M91-based metallicities.

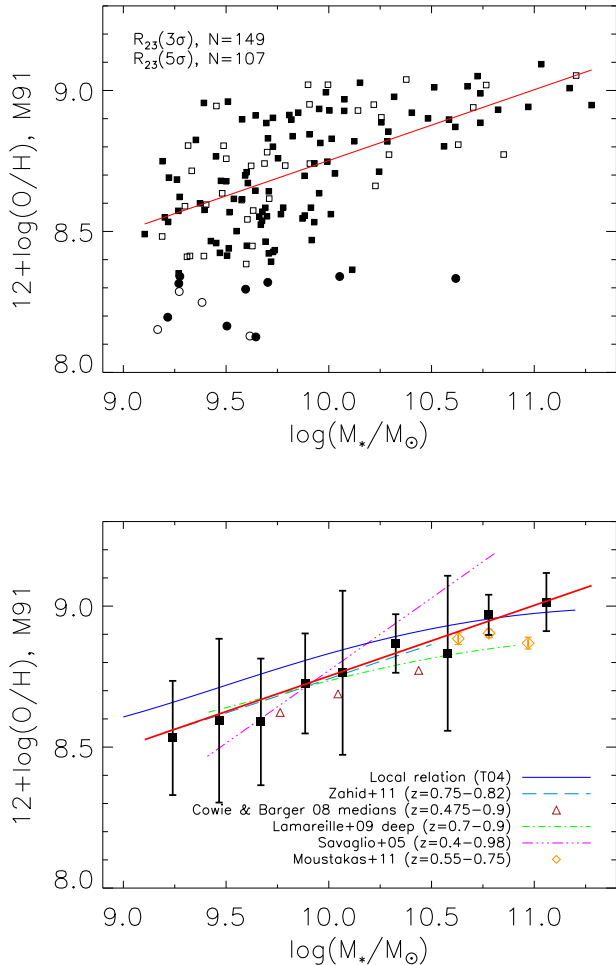


FIG. 10.— Top: Comparison of the NewH α M_* - Z data with a linear fit (solid line, red in online version). Filled points mark sources for which R_{23} lines ([O II], [O III], and H β) are at least detected at 5σ with additional sources from the 3σ sample (unfilled). Circles indicate galaxies with high R_{23} values such that the upper branch metallicity is less than the lower branch metallicity. Bottom: Comparison of the NewH α M_* - Z linear fit with literature relations. All metallicities have been converted to the M91 calibration using the relations of Kewley & Ellison (2008); for the local relation, we transformed from T04. Filled squares denote means of NewH α data binned by mass, with errorbars representing standard deviations.

Survey—a wide-shallow sample (6.1 deg^2 and $17.5 \leq I_{\text{AB}} \leq 22.5$) and a narrow-deep sample (0.61 deg^2 and $17.5 \leq I \leq 24$, green dot-dashed line in Figure 10). Metallicities were calculated from rest-frame optical emission lines using the R_{23} line flux ratio and the T04 metallicity calibration. Because the wide sample has shallower magnitude limits and is biased towards massive galaxies, we choose to compare the NewH α M_* - Z relation against the deep sample ($N \sim 40$ for $0.7 < z < 0.9$). Figure 10 shows that this sample is well within the intrinsic scatter of the NewH α relation. Lamareille et al. (2009) observed that the M_* - Z relation evolves towards lower overall metallicities more quickly for more massive galaxies. However, low spectral resolution ($R_s \approx 230$ or a large error domain on AGN classification could also have an effect on both the Lamareille et al. (2009) samples; in particular, contamination from AGN would falsely lower metallicity results, since photoionization by AGN can produce rest-frame optical emission-line ratios that ap-

pear similar to metal-poor star-forming galaxies (Moustakas et al. 2011).

Cowie & Barger (2008) used a sample of 154 galaxies from the 145 arcmin^2 GOODS-N field, selected by rest-frame NIR bolometric flux (the limiting flux corresponding roughly to an NIR magnitude of $K_s = 23.4$). Metallicities were calculated using the R_{23} line ratio and both the KK04 and T04 calibrations, although equivalent widths (EWs) were used rather than emission-line fluxes. Zahid et al. (2011) noted a systematic error in the Cowie & Barger (2008) relation as a result of the fitting procedure used—the R_{23} metallicity diagnostic is less sensitive at the R_{23} local maximum at $12 + \log(\text{O}/\text{H}) \sim 8.4$, which leads to asymmetric metallicity errors that influence the least-squares fit. We therefore follow the example of Zahid et al. (2011) and plot the median metallicities (red triangles in Figure 10) rather than the functional form prescribed by the mean metallicities. The median metallicities are within the scatter of the NewH α relation.

Zahid et al. (2011) studied galaxies from the DEEP2 survey (Davis et al. 2003), which covers a fairly large field of 3.5 deg^2 . Out of 31,656 objects in the DEEP2 survey with well-measured redshifts, only sources with spectra covering the wavelength range of $3720\text{--}5020 \text{ \AA}$ (bracketing the rest-frame optical emission lines required for R_{23} , see Section 3.3) and emission lines that could be fit were considered in analysis. Further sample cuts included thresholds on H β S/N, H β EW, combined R_{23} errors, continuum fits, and the removal of sources with $\log R_{23} > 1$ (considered AGN), leaving a final sample size of $\approx 1,600$. As in Cowie & Barger (2008), metallicities were calculated with the R_{23} ratio formula, using emission line EWs and the KK04 calibration. Insufficient sample cuts for AGN, color contamination from red non-SF galaxies, and a lack of S/N cut on [O II] and [O III] lines would all tend to underestimate metallicity, but we find that the Zahid et al. (2011) relation (light blue dashed line in Figure 10) is extremely consistent with the NewH α data at overlapping mass bins.

Finally, Moustakas et al. (2011) used a large (~ 3000 galaxies) sample from the AGN and Galaxy Evolution Survey, which covers 7.9 deg^2 . The survey is magnitude-limited ($I_{\text{AB}} < 20.45$), and emission-line galaxies were selected with the criteria that H β line flux is above $3 \times 10^{17} \text{ erg s}^{-1} \text{ cm}^{-2}$ and $\log([\text{O II}]/\text{H}\beta) > -0.3$. Metallicities are computed using the EW formulas for the line ratios R_{23} and O_{32} and the M91, KK04, and T04 calibrations. The Moustakas et al. (2011) and NewH α samples are complementary: the former is mass-incomplete below $10^{10.7} M_\odot$ at $z \sim 0.8$ as a result of the survey flux limit, while the NewH α mass completeness drops off below $\sim 10^{9.5} M_\odot$ because our data are emission-line selected. Therefore, disregarding the NewH α data above an upper mass-completeness limit ($\sim 10^{10.5} M_\odot$), the Moustakas et al. (2011) M_* - Z relation (orange diamonds in Figure 10) appears to be a smooth extension of the NewH α relation to higher masses.

4.4. The Mass–Metallicity–SFR Relation

Combining the stellar mass, metallicity, and SFR measurements for the NewH α sample, we now consider the correlation between all three derived properties. As discussed in the introduction, residuals from the M_* - Z re-

lation have been found to correlate with the SFR in local galaxy samples. We aim to test whether a similar secondary dependence on the SFR also exists in galaxies at $z \sim 0.8$ as sampled by the NewH α dataset.

The NewH α survey is one of the first surveys to offer both spectroscopic measurements of the strong oxygen emission lines and H α narrowband fluxes at intermediate redshifts, enabling more robust constraints on the nebular abundances and instantaneous SFRs. These measurement methods are also commonly used at local redshifts, and allow a more self-consistent test of whether the M_\star - Z -SFR relation remains the same over cosmic time. To investigate the M_\star - Z -SFR relation, we first remove all AGN, sources with poor SED fits ($\chi_\nu^2 > 10$), sources with an NB118 excess flux below 3σ , and limit the dataset to the $R_{23}(3\sigma)$ sample. These restrictions remove 180 galaxies from the sample, leaving 119 galaxies for the following analysis. We note that the $R_{23}(3\sigma)$ cut removed the majority of galaxies ($N=120$).

Different parameterizations have been used to describe the local M_\star - Z -SFR relation (see e.g., Man10; Lar10). Some studies (Lar13; Hunt et al. 2012) have assumed that this relation can be accurately described by a plane. In particular, Lar13 argued that this may in fact be the best functional representation of the M_\star - Z -SFR relation, and refer to it as a “fundamental plane.” In contrast, Man10 used a higher order parameterization (dubbed the “fundamental metallicity relation”), which is motivated by the flattening at high stellar masses in the M_\star - Z relation (e.g., T04; Moustakas et al. 2011). In addition, many studies (e.g., Richard et al. 2011; Xia et al. 2012; Belli et al. 2013; Stott et al. 2013; Henry et al. 2013a,b; Zahid et al. 2013b; Ly et al. 2014; Yabe et al. 2014) have compared their samples against the fundamental metallicity relation to determine if it holds at higher redshifts.

To enable direct comparison to Lar10 and Lar13, we begin by assuming that our relation can be accurately described by a plane. Since commonly adopted methods for determining the best-fit plane may lead to different results and interpretation, we use multiple techniques as described below: (1) principal component analysis (PCA), (2) two-parameter regression, and (3) three-dimensional χ^2 minimization.

We then explore a higher order parameterization of the data following the methodology of Man10. We later compare our analyses with previous works in Section 5, and revisit the assumed plane parameterization in Section 5.3 and discuss possible implications.

We note that all the results that follow are based on metallicities determined using the T04 calibration, in order to facilitate direct comparison with previous studies. Another metallicity calibration (M91 as used previously for the M_\star - Z relation) has been used, and we find that to first order, the M_\star - Z -SFR relation does not significantly differ. The results of our planar fits with different metallicity calibrations (T04 and M91) are summarized in Tables 8, 9, and 10.

4.4.1. Principal Component Analysis

First, we conduct a PCA for our NewH α dataset. This approach determines the eigenvectors (called V1, V2, and V3), formed from linear combinations of the input parameters, that are orthogonal to one another. One of

the advantages of the technique is the ability to examine correlated measurements. This is important for the M_\star - Z -SFR relation, since the metallicity and SFR measurements are strongly correlated with the derived stellar mass. Given these correlations, the application of the PCA technique allows us to examine if a tilt in the direction of the SFR is present for a plane parameterization. This technique has been used by Lar13 and Hunt et al. (2012) to determine the best-fit planar description for the M_\star - Z -SFR relation. We conduct our PCA analysis on the covariance matrix of our dataset with three variables:

$$\begin{aligned} x_1 &\equiv \log\left(\frac{M_\star}{M_\odot}\right), \\ x_2 &\equiv 12 + \log(\text{O}/\text{H}), \text{ and} \\ x_3 &\equiv \log\left[\frac{\text{SFR}_{\text{H}\alpha}}{M_\odot \text{ yr}^{-1}}\right]. \end{aligned} \quad (5)$$

To account for measurement uncertainties in the PCA, we conduct Monte Carlo realizations of our data, where the stellar mass, SFR, and oxygen abundance for each galaxy in the sample are drawn 100,000 times from a Gaussian probability distribution defined by the 1σ errors in each parameter. We then fit each simulated sample of 119 galaxies using the PCA code available through the NASA IDL Astronomy User’s Library.

We find that the first two principal components account for $78.8\% \pm 1.6\%$ and $15.2\% \pm 1.5\%$ of the variance, respectively. The first principal component, which has the largest variance, is $V1 = (0.610, 0.183, 0.771)$. The other two eigenvectors are $V2 = (0.690, 0.352, -0.629)$, and $V3 = (-0.384, 0.923, 0.087)$. In Figure 11, the data are projected in the planes defined by these principal components.

Since V1 and V2 have the largest dispersions, they can be interpreted as vectors that lie along the best-fit plane, while V3 is the vector that is orthogonal to the plane. Figure 11 illustrates that V3 has the least amount of variance with an rms of ≈ 0.18 dex. This low dispersion is critical, as it suggests that V3 provides a mathematical description for the best-fit plane such that a combination of stellar mass, SFR, and metallicity yields a constant:

$$\alpha x_1 + \beta x_2 + \gamma x_3 = \delta, \quad (6)$$

with $(\alpha, \beta, \gamma, \delta) = (-0.384_{-0.04}^{+0.03}, 0.923 \pm 0.02, 0.087_{-0.03}^{+0.04}, +4.301_{-0.46}^{+0.57})$. The V3 results from our Monte Carlo realization are shown in Figure 12. A summary of our PCA results, using different metallicity calibrations (M91; T04) and sample selections, can be found in Table 8.

Assuming that our data can be described by a plane, γ can be interpreted to signify the importance of the SFR in the correlation. The PCA shows that γ is non-zero ($\approx 3\sigma$ significance), suggesting that the plane which best describes our dataset is moderately tilted in the SFR dimension.

4.4.2. Two-Parameter Regression

Another approach for finding the best-fit plane is linear regression, whereby one parameter is modeled in terms of two other parameters. We consider a plane parameterization used to describe local galaxies (Lar10), where

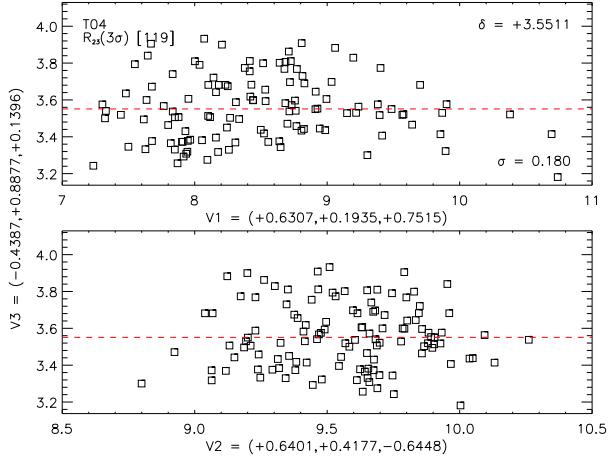


FIG. 11.— PCA of our $R_{23}(3\sigma)$ sample with metallicities determined using the T04 calibration. The first and second principal components (V1 and V2) are shown in the top and bottom panels, compared with the third component (V3) with the least amount of variance. The dashed line represents the average of V3. Our sample can be described by Equation (6) with $(\alpha, \beta, \gamma) \approx (-0.384, 0.923, 0.087)$. The PCA results from our Monte Carlo realizations are provided in Figure 12.

the stellar mass is treated as the dependent variable:

$$\log\left(\frac{M_\star}{M_\odot}\right) = \beta_M Z + \gamma_M \log\left(\frac{\text{SFR}_{\text{H}\alpha}}{M_\odot \text{ yr}^{-1}}\right) + \delta_M, \quad (7)$$

where $Z \equiv 12 + \log(\text{O}/\text{H})$. We conduct the regression using the IDL routine MPFIT (Markwardt 2009), which uses the Levenberg-Marquardt least-squares minimization technique. As with the PCA, we also perform a Monte Carlo simulation to determine the uncertainties in the fit. Here, the Gaussian randomization only occurs in the two independent variables (SFR and metallicity) and measured uncertainties in the dependent variable (stellar mass) are accounted for in the least-squares minimization. The results of our Monte Carlo simulation are shown in Figure 13, and are reported in Table 9 using two different metallicity calibrations (T04; M91). The best fitting parameters that describe the NewH α sample are $\beta_M = 0.67^{+0.13}_{-0.11}$, $\gamma_M = 0.50^{+0.04}_{-0.05}$, and $\delta_M = 3.75^{+1.02}_{-1.01}$.

While Equation (7) was reported to yield the lowest χ^2 in all three observables for local SDSS galaxies (Lar13), it can be viewed as counter-intuitive²⁰. A better description of the plane, which is a simple extension of the M_\star - Z relation, is:

$$Z = \alpha_Z \log\left(\frac{M_\star}{M_\odot}\right) + \gamma_Z \log\left(\frac{\text{SFR}_{\text{H}\alpha}}{M_\odot \text{ yr}^{-1}}\right) + \delta_Z. \quad (8)$$

The regression fitting for our sample using this projection, as shown in Figure 13, yielded $\alpha_Z = 0.23 \pm 0.02$, $\gamma_Z = 0.01^{+0.02}_{-0.03}$, and $\delta_Z = 6.61^{+0.18}_{-0.12}$ for T04 metallicities. The results of our $Z = f(M, \text{SFR})$ regression are consistent with our previous M_\star - Z least-squares fitting, which found a slope (α_Z) of 0.25 and a constant offset (δ_Z) of 6.23 (Section 4.3). This regression analysis demonstrates that a strong secondary dependence on the SFR for a M_\star - Z -SFR plane is *not* present in our dataset. We

²⁰ Other galaxy properties have been extensively compared against the stellar mass (i.e., the latter is treated as the independent variable).

summarize our $Z = f(M, \text{SFR})$ regression results for T04 and M91 in Table 10.

4.4.3. Three-Dimensional χ^2 Minimization

One of the limitations of the two-parameter regression approach—used to study the SDSS sample by Lar10 and Lar13—is the arbitrary choice of the independent and dependent variables, as we have discussed. To address this, we consider a three-parameter fit that simultaneously minimizes χ^2 in all three dimensions. We assume that the data can be described by a plane as given by Equation (6). This method complements the PCA, since it is less susceptible to outliers that directly affect the covariance matrix, and hence the principal components (see Section 5.2 for further discussion). It is a three-dimensional extension of the χ^2 estimator used by Tremaine et al. (2002), for example. To obtain meaningful errors, we scale our measurement uncertainties to yield a reduced χ^2 of 1. We find a best fit of $(\alpha, \beta, \gamma, \delta) = (-0.37 \pm 0.05, 0.92 \pm 0.02, 0.10 \pm 0.05, 4.54 \pm 0.64)$. These values are similar to those determined from PCA, again suggesting that there is at most a moderate dependence of metallicity on the SFR for H α -selected galaxies from the NewH α survey.

4.4.4. Non-planar Formalism of Mannucci et al. (2010)

As previously stated, a curved-surface parameterization may be a better representation of the M_\star - Z -SFR relation. With this in mind, we split our sample into low-mass and high-mass subsamples and perform PCA. The results are summarized in Table 8. We find that the planes which best fit the low-mass sample are significantly different from those that best fit the high-mass sample.

We therefore consider a non-planar fit between the three derived properties following Man10, who determined a curved-surface representation of the M_\star - Z -SFR relation at local redshifts. Man10 calculated metallicities for local SDSS galaxies with two separate emission-line flux ratio measurements—the Nagao et al. (2006) [N II] $\lambda 6583/\text{H}\alpha$ calibration and the Maiolino et al. (2008) R_{23} calibration. In cases where both measurements agree within 0.25 dex, an average of the two was used. Since [N II]/H α measurements do not exist for our sample, direct comparison of the NewH α sample to Man10 is difficult. In particular, while we could examine whether the M_\star - Z -SFR relation exists in our sample using *only* R_{23} -based metallicities estimated from the Maiolino et al. (2008) calibration, we note that this approach has yet to be conducted with SDSS galaxies (i.e., excluding [N II]/H α measurements). A Maiolino et al. (2008) R_{23} -based M_\star - Z -SFR relation is beyond the scope of this paper. Therefore, we choose to compare to the relation determined by Yat12, who followed the same procedure as Man10 but used T04 metallicities.

We determine a second-order polynomial fit of metallicity as a function of a linear combination of mass and SFR:

$$\mu_\alpha = \log\left(\frac{M_\star}{M_\odot}\right) - \alpha \log\left(\frac{\text{SFR}}{M_\odot \text{ yr}^{-1}}\right), \quad (9)$$

where α is a free parameter chosen to minimize the scatter of metallicity. Here, $\alpha = 0$ corresponds to the M_\star - Z

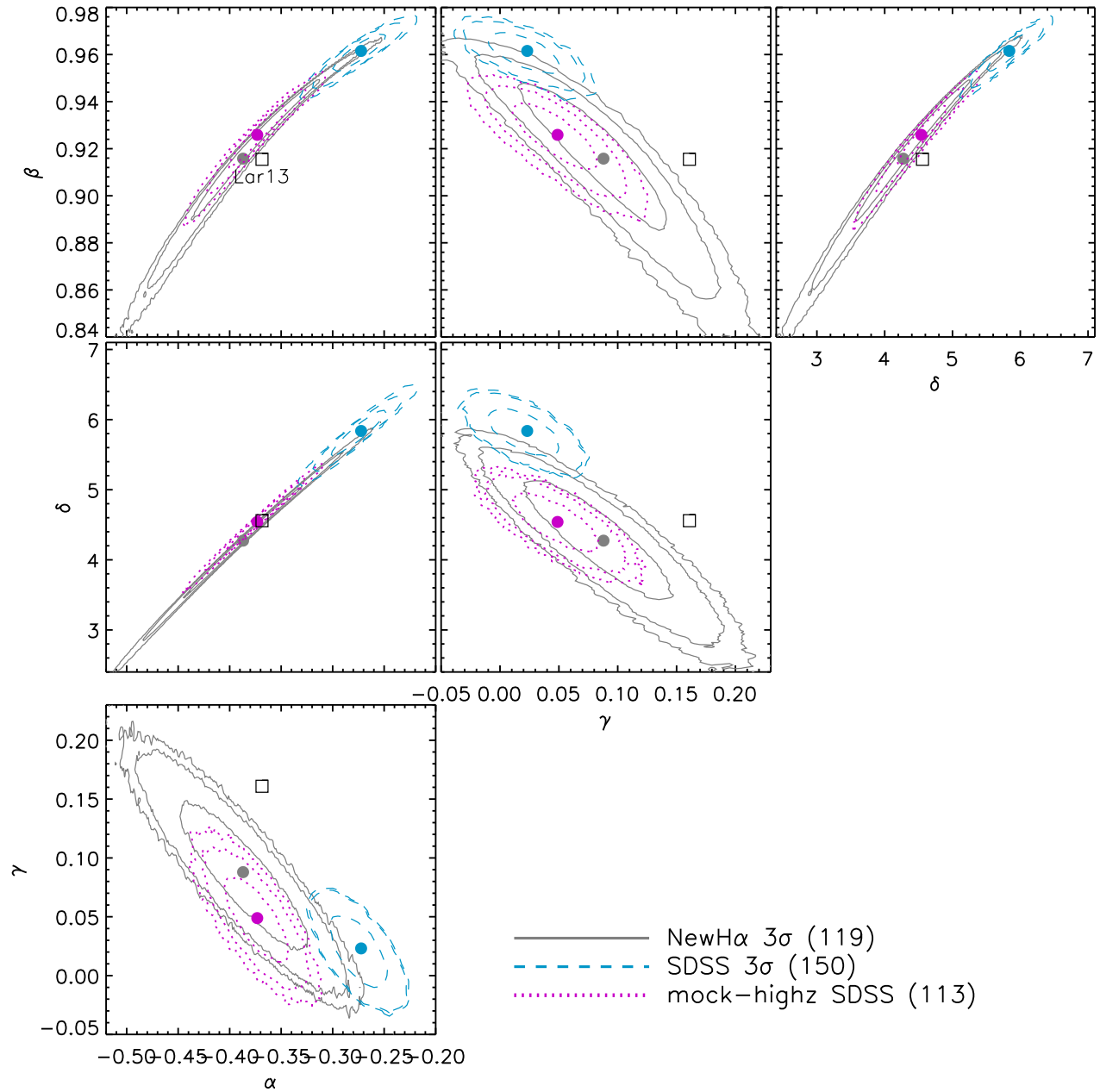


FIG. 12.— Results of Monte Carlo PCA fitting to the NewH α $R_{23}(3\sigma)$ sample of 119 galaxies (grey solid lines) compared to 150 randomly-selected local galaxies from the SDSS (blue dashed lines). We also overlay a sample (“mock-highz SDSS”; see Section 5.1) selected from the SDSS to have similar stellar masses and SFRs to NewH α galaxies (purple dotted lines). Coefficients α , β , γ , and δ describe a plane as given in Equation (6). Contours at 68%, 95%, and 99% confidence are shown. These contours demonstrate that the best-fitting PCA plane for the NewH α sample is consistent with fits to SDSS galaxy samples with similar sample size. The standard PCA fit of Lar13 is shown by the open squares.

relation while $\alpha = 1$ refers to metallicity having an inverse dependence with the specific SFR.

We consider a range of α values, and illustrate in Figure 14 the dispersion of the best-fit second-order polynomial. This result demonstrates that scatter in metallicity is minimized at $\alpha \sim 0.05$ (i.e., suggesting weak dependence on the SFR). High values of α ($\gtrsim 0.5$) can be excluded, suggesting that a strong dependence on SFR does not exist. However, we cannot exclude moderate dependence (e.g., $\alpha = 0.19$ for local galaxies as determined by Yat12), since the scatter in metallicity does not significantly change for $\alpha \lesssim 0.5$. This result is illustrated in

Figure 15, where we plot the best-fit second-order polynomial for both $\alpha = 0.05$ and $\alpha = 0.19$.

5. DISCUSSION

As discussed in the introduction, the detailed relation between galaxy stellar mass, SFR, and gas-phase metallicity is important for understanding inflows and outflows of gas, and the chemical evolution of galaxies. The shape of this relation and the degree to which it does or does not evolve with redshift can provide insights into whether the processes governing the interaction between galaxies and their surrounding medium are “fundamental” in the sense that they may not differ substantially at various

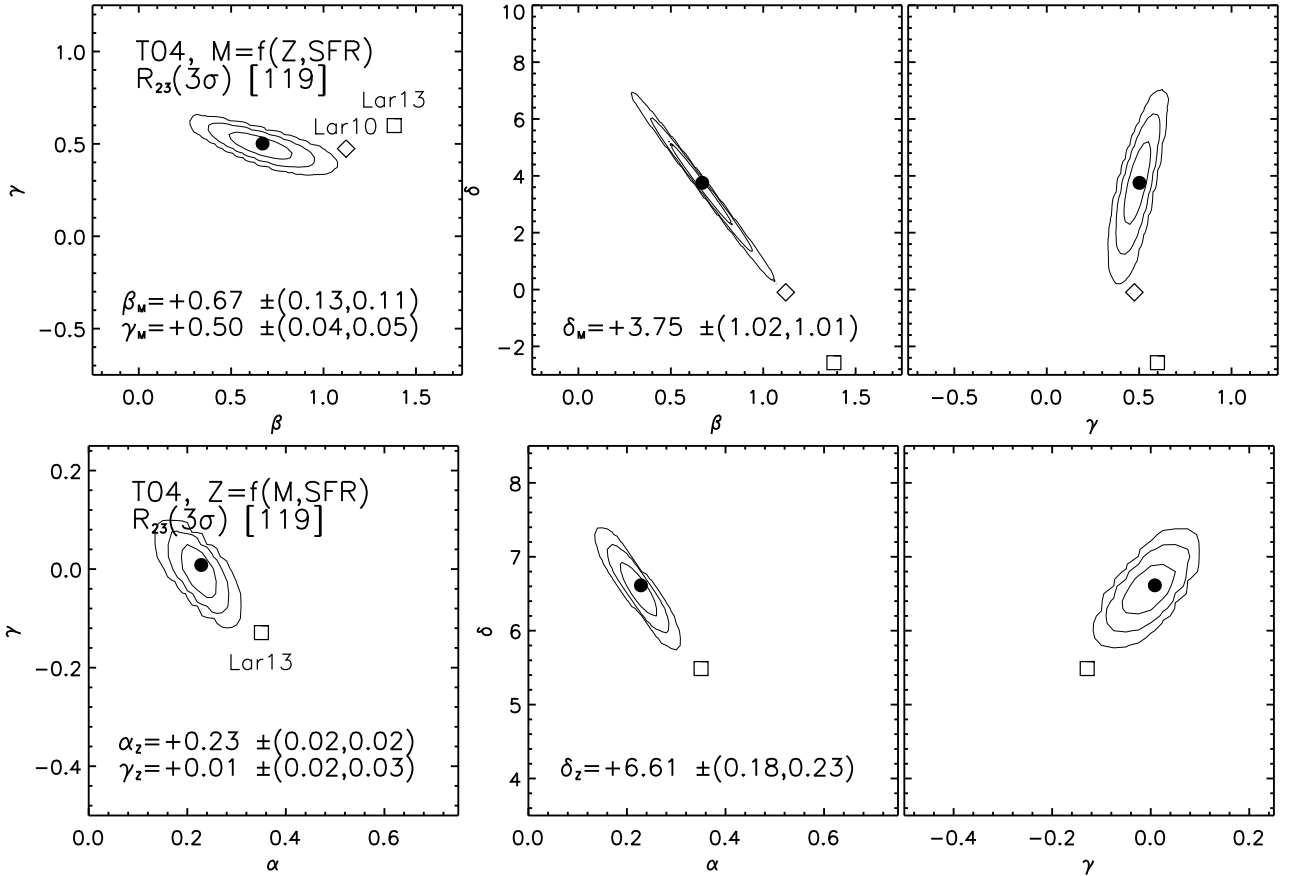


FIG. 13.— Results of our Monte Carlo simulations for regression-based plane fitting. The top panels show the fitting conducted with stellar mass as the dependent variable, $M = f(Z, \text{SFR})$, while the bottom panels consider $Z = f(M, \text{SFR})$. Metallicities are based on the T04 calibration. The regression fits of Lar10 and Lar13 are shown as open diamonds and squares, respectively.

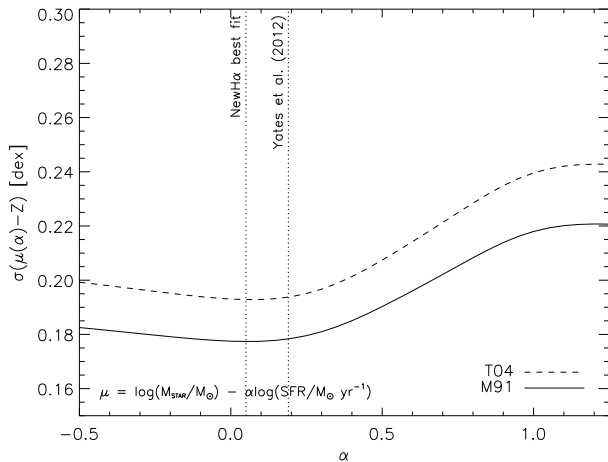


FIG. 14.— Dispersion in oxygen abundances for different projections of the M_{*} - Z -SFR relation using a curved-surface least-squares fitting approach with $\mu = \log\left(\frac{M_{*}}{M_{\odot}}\right) - \alpha \log\left(\frac{\text{SFR}}{M_{\odot} \text{ yr}^{-1}}\right)$. Calculations were conducted using M91- (solid line) and T04-based (dashed line) metallicities. The analyses show that a strong secondary dependence on SFR does not exist, consistent with planar fitting approaches; however, the data cannot exclude or distinguish between zero and weak dependence ($\alpha = 0.19$; Yat12).

points in cosmic time.

Several studies (e.g. Man10; Lar10; Lar13) have reported that along with the well-established strong correlation between mass and metallicity, there is a moderate, but significant correlation with the SFR. Further-

more, a number of studies, including Man10 and Hunt et al. (2012), have indeed found that galaxies at redshifts up to $z \sim 3$ can be described by the same M_{*} - Z -SFR relation. However, contradictory results have recently been reported: Sánchez et al. (2013) and Hughes et al. (2013) were unable to find a significant correlation with the SFR, and argue that previous results based on the SDSS dataset were spurious due to aperture effects (for further discussion, see Section 4 of Sánchez et al. 2013). Also, Zahid et al. (2013b) found evidence for redshift evolution in the M_{*} - Z -SFR relation.

In Section 4.4 of this paper, we examined if the M_{*} - Z -SFR relation at $z \sim 0.8$ exists using the NewH α dataset—and if it does, to determine if it is consistent with previous analyses of local galaxies from the SDSS dataset. To facilitate comparison to local results, we followed previous approaches by assuming that the M_{*} - Z -SFR relation can be described by a plane or a surface. For the planar description, we used PCA, two-parameter regression, and χ^2 minimization with metallicities calibrated against T04. We found that the NewH α data show a moderate dependence ($\gamma \approx 0.1$) of the M_{*} - Z relation on SFR. This is slightly lower than the dependence found in the local universe ($\gamma \approx 0.16$; Lar13). For the curved-surface parameterization, we use least squares fitting to describe a second-order polynomial between metallicity and a combination of mass and SFR. This analysis excludes a strong dependence of the M_{*} - Z relation on SFR; however, it cannot distinguish between

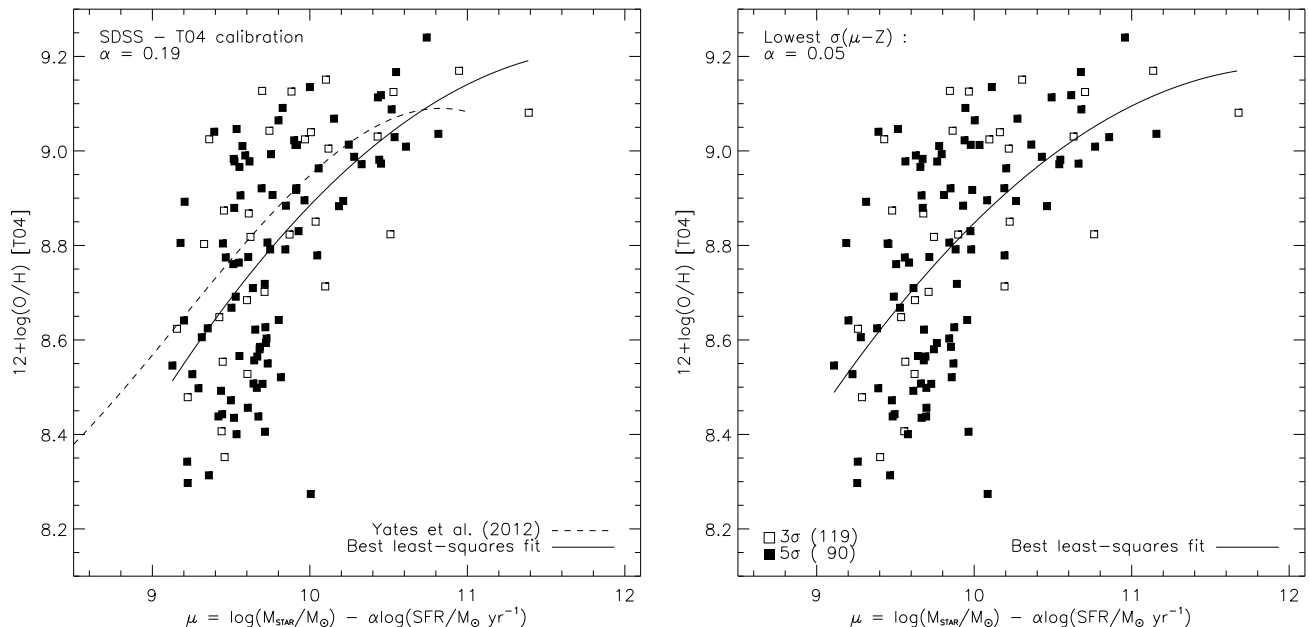


FIG. 15.— M_* - Z -SFR relation following the projection (μ - Z) of Man10. Here we illustrate best-fit projection for local SDSS galaxies (left, $\alpha = 0.19$; Yat12) and the projection with the lowest dispersion for the NewH α sample (right, $\alpha = 0.05$). The best-fitting third-order polynomial of Yat12 is shown by the dashed line while our best fits are shown by the solid lines. Filled squares show the $R_{23}(5\sigma)$ sample with additional sources in the $R_{23}(3\sigma)$ sample (opened squares). For direct comparisons to Yat12, we use T04-based metallicities.

moderate and no dependence.

How do we interpret our results, and where do they fit in within the current debate on the M_* - Z -SFR relation? We address these questions by first investigating whether some limitation(s) of our analyses or dataset may obscure the true underlying relationship. We ask:

1. Is our result biased or affected by some limitation of the NewH α dataset? (Section 5.1)
2. Is our result biased or affected by the chosen plane-fitting techniques? (Section 5.2)
3. Finally, is our result biased or affected by our assumed parameterizations of the dataset? (Section 5.3)

5.1. Limitations of the NewH α Dataset

The following sample limitations may, individually or in combination, bias our measurement of the SFR dependence of the M_* - Z -SFR relation: (1) small sample size, (2) measurement uncertainties, and (3) restricted coverage of parameter space. These limitations apply generally to any study attempting to construct a M_* - Z -SFR relation.

In this work, we focus on the first possible limitation: the small size of the NewH α sample (119 galaxies) used for studying the M_* - Z -SFR relation. To understand the effects of sample size we construct “mock” samples from the SDSS DR7 sample. Here, the MPA-JHU catalog provides total stellar masses from fitting the $u'g'r'i'z'$ photometry (Salim et al. 2007), total SFRs primarily from Balmer emission lines (Brinchmann et al. 2004), and metallicity within the optical fibers following T04. Restricting our sample to galaxies²¹ with estimates of

²¹ Selected by the Baldwin et al. (1981) diagnostic selection following Kauffmann et al. (2003) with at least a 3σ detection for H α , [N II], [O III] λ 5007, and H β .

stellar mass, metallicity, and SFR, and redshift between $z = 0.07$ and $z = 0.30$, we have a working SDSS sample of 90,686 galaxies.

We therefore begin with a randomly-selected subsample of 150 galaxies and then consider improvements to our base sample by increasing the sample size. We fit each SDSS subsample with a plane using the PCA technique, as discussed in Section 4.4.1, for direct comparisons with our NewH α results. For the smallest subsample, we find little dependence on the SFR, with $\gamma \approx 0.02$. We then increase the sample size in increments of 150 galaxies, with the expectation that the larger sample size will provide more definitive constraints on SFR dependence. However, even with a sample of 1950 galaxies (13 times larger than the base sample), γ remains at or below 0.05. Extending the PCA analysis to the largest sample possible ($N = 90,686$), we find that a surprisingly weak dependence exists on the SFR ($\gamma = 0.02$) for a planar description of the M_* - Z -SFR relation. This dependence is roughly three to eight times weaker than that found by Lar13, but consistent (within errors) with results from the analysis based on the NewH α dataset reported here ($\gamma \approx 0.087^{+0.04}_{-0.03}$). This is best demonstrated in Figure 12 where the mock SDSS sample, with similar sample size ($N = 150$) to the NewH α sample, is shown by the dashed (blue) line contours.

How can the results of our experiments with mock SDSS samples be reconciled with the results of Lar13? The sample used by Lar13 used stricter selection cuts. Their strictest constraint is on the S/N for the [O III] λ 5007, H β , H α , and [N II] emission lines (requiring at least 8σ). The H α restriction biases their sample toward higher SFRs, while the [O III] restriction preferentially selects against metal-rich galaxies, leaving metal-poor galaxies with higher SFRs in the sample. Interestingly, we do find that a S/N restriction of 8 on the nebular emission lines yielded a higher SFR coefficient ($\gamma \approx 0.08$ –0.14

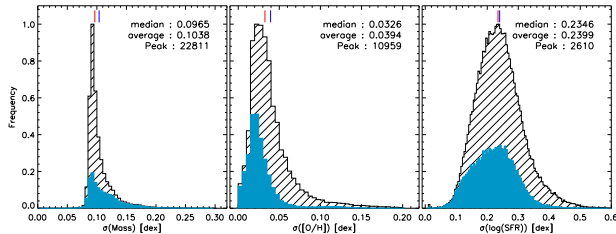


FIG. 16.— Distribution of measurement uncertainties for stellar mass (left), metallicity (middle) and SFR (right) of the SDSS sample. The full sample of 90,686 galaxies is shown cross-hatched, while a smaller sample with restrictions on the [O III], H β , H α , and [N II] lines ($S/N \geq 8$) is shown filled-in (blue in online version).

with the standard PCA) based on sample sizes that span 150 to 31,477 galaxies.

The mock SDSS samples used in the analysis described in this section, on the other hand, were constrained by similar emission-line restrictions (3σ detection) used for the NewH α dataset, and achieved results more consistent with the NewH α results. To further demonstrate this point, we also selected from the SDSS galaxies with similar (≤ 0.1 dex) stellar masses and SFRs to those in the NewH α sample (hereafter “mock-highz SDSS”). Because local galaxies have lower SFRs, six of 119 NewH α galaxies do not have a “local analog.” The results of the PCA for the mock-highz SDSS sample are shown as dotted (purple) line contours in Figure 12, and are in better agreement with the NewH α PCA results. These comparison results suggest that the differences in sample selection may therefore produce the observed discrepancy between the results of NewH α and the results of Lar13.

5.2. Limitations of Principal Component Analysis

Another potential issue with our investigation is our reliance on the PCA technique to find the plane that best describes the M_\star - Z -SFR relation, and to compare to results based on local galaxy samples. This technique has shortcomings, particularly in its sensitivity to outliers.

PCA finds eigenvectors (or principal components) formed from linear combinations of input parameters (M_\star , Z , and SFR). Since variance-dependent calculations are used to determine the principal components, outliers may strongly skew PCA results. Considering the uncertainties of derived quantities and large size of the SDSS sample, there are significant numbers of (true) outliers in the sample that would suggest that the PCA technique is unreliable for the SDSS.

This is particularly demonstrated when we account for measurement uncertainties through Monte Carlo techniques in the PCA fitting (see Section 4.4.1). We find a different best-fit plane (albeit one that still has a low γ) when compared to a standard PCA (i.e., without considering uncertainties). This is expected because of the uncertainties on the SFRs: at least 32% of the SDSS sample deviates significantly (≥ 0.22 dex; see Figure 16) from what is likely the best-fitting plane. When performing the same analysis with an SDSS sample similar to that of Lar13, we also find a different result for γ , ~ 0.12 versus the reported result of 0.16.

We suggest that instead of PCA, three-dimensional χ^2 minimization (see Section 4.4.3) should be the preferred method of parameterizing the M_\star - Z -SFR relation as a plane. The three-dimensional χ^2 minimization technique fits all three observables simultaneously and is

less susceptible to outliers: galaxies with more uncertain measurements are downweighted relative to those with more precise measurements. In the case of the NewH α dataset, our results are consistent between PCA and three-dimensional χ^2 fitting, suggesting that our sample is not as severely affected by the PCA analysis. Nevertheless, we recommend caution when proceeding with PCA analysis without understanding the effects of outliers.

5.3. Limitations of the Parameterization of the M_\star - Z -SFR Relation

In much of our analysis—including our investigation of potential sample size and PCA technique limitations—we have adopted a plane to describe our data. However, as noted in Section 4.4.4, this assumption may be wrong. If there is in fact a M_\star - Z -SFR relation which is fundamental (i.e., universally describes galaxies at all redshifts), and there is curvature in that relation, studies which assume a plane parameterization in their analysis may mistakenly infer evolution in the relation. That is, evolution in a planar relation may actually be a result of sampling different parts of the curved surface relation with respect to redshift. At $z \sim 0.8$, the NewH α sample has lower average metallicity and higher average SFR than the local SDSS sample does. Furthermore, if the M_\star - Z -SFR relation is curved, the results from a plane fit can be different if the sample is limited in parameter space. This is demonstrated in Section 4.4.4 when we split our sample into low-mass and high-mass subsamples. The plane that best fits the low-mass sample is significantly different from the one that fits the high-mass sample. This implies that our sample follows a non-planar projection—a discrepancy is unsurprising if there is no truly “good” planar fit.

With this in mind, we follow the procedure of Man10 and Yat12 to find the projection of least scatter, as described in Section 4.4.4. In this projection, the parameter α describes the dependence of the M_\star - Z relation on the SFR. Our dataset excludes a strong dependence on SFR ($\alpha \gtrsim 0.5$); however, it cannot distinguish between moderate ($\alpha \sim 0.2$) and no dependence. This result is consistent with those reported for local galaxies ($\alpha = 0.19$; Yat12).

We note that although several M_\star - Z -SFR studies have followed the methods of Man10 (Yates et al. 2012; Andrews & Martini 2013), the effects of binning the SDSS sample by both mass and SFR have been a point of some contention, as Lar13 have argued that the grid adopted for data binning can effectively change the shape of the curved-surface M_\star - Z -SFR relation. In addition, this method of projection of least scatter relies on an initial assumption of a polynomial functional form.

We therefore suggest that future work be done to investigate *non-parametric* methods of fitting the M_\star - Z -SFR relation. For instance, the Kolmogorov-Smirnov (K-S) test is used to compare a one-dimensional sample with a reference probability distribution. An extension of the K-S test to three dimensions would be ideal for fitting the M_\star - Z -SFR relation while avoiding assumptions about the shape or functional form of the relation.

We have studied the relationships between stellar mass, SFR, and metallicity using a sample of 299 galaxies at $z \sim 0.8$ selected by the presence of H α emission in a narrow bandpass filter. Deep optical spectra obtained with Magellan IMACS enable us to measure gas-phase metal abundances with various theoretical and empirical oxygen-based calibrations, and to compare them to SFRs estimated from the H α luminosity and stellar masses from SED modeling.

Our emission-line galaxy sample spans stellar masses from $\sim 10^9$ to $6 \times 10^{11} M_{\odot}$, H α -based SFRs between 0.4 and $270 M_{\odot} \text{ yr}^{-1}$, and metallicities from $12 + \log(\text{O}/\text{H}) = 8.3$ to 9.1 ($Z/Z_{\odot} = 0.4$ – 2.6) on a metallicity scale based on the M91 calibration.

We compared H α -based SFRs with SFRs estimated from SED fitting (i.e. FUV-based SFRs). We found that once both measures were corrected for dust attenuation with optical depths computed from SEDs, the two measures agreed well (median offset of ~ 0.09 dex) with low dispersion (~ 0.2 dex). In addition, this agreement holds for the full range of stellar mass and for high SFRs ($\gtrsim 100 M_{\odot} \text{ yr}^{-1}$).

Based on a linear least-squares fit over stellar masses between $10^{9.1} M_{\odot}$ and $10^{11.7} M_{\odot}$, the M_{\star} - Z relation for our sample is $12 + \log(\text{O}/\text{H}) = (0.25 \pm 0.03) \log\left(\frac{M_{\star}}{M_{\odot}}\right) + (6.23 \pm 0.33)$. This is consistent with previously reported results for galaxy samples at similar redshifts. At fixed stellar mass, the M_{\star} - Z relation for our sample is systematically lower by 0.1 dex in metallicity than the local SDSS relation of T04.

Similarly, we found a NewH α M_{\star} -SFR relation of $\log\left(\frac{\text{SFR}_{\text{H}\alpha}}{M_{\odot} \text{ yr}^{-1}}\right) = (0.75 \pm 0.07) \log\left(\frac{M_{\star}}{M_{\odot}}\right) - (6.73 \pm 0.67)$, which is consistent with literature results at similar redshifts (within 0.15 dex in SFR of previous results). This consistency is somewhat surprising given that the NewH α sample is H α selected, which might bias our relation toward higher SFR. However, this suggests that our sample is in fact relatively complete down to low EWs.

We then calculated the best-fit plane describing the stellar masses, SFRs, and metallicities of the NewH α sample using three methods: principal component analysis, two-parameter regression, and three-dimensional χ^2 minimization. The fits resulting from all these analyses at $z \sim 0.8$ showed only a moderate secondary dependence on the SFR weaker than that reported by Lar13 and Lar13. In addition, we considered a curved-surface parameterization following Man10, and found that the NewH α sample is consistent with local studies (i.e., a weak dependence of the M_{\star} - Z relation on SFR; Yat12), and excludes a strong SFR dependence.

To better understand the possible implications of these results, we asked whether some limitation of our dataset and/or analysis may obscure a stronger or weaker dependence on the SFR by using mock samples drawn from the SDSS.

We started by examining possible issues associated with the small size of our sample. Using a randomly-selected subsample of 150 SDSS DR7 galaxies using the PCA technique, we found a dependence on the SFR that

was three to eight times weaker than the SDSS study of Lar13. Somewhat surprisingly however, increasing the sample size did not significantly change this result, even using the largest possible sample ($N \approx 90,000$). We learned that differences in the adopted signal-to-noise cuts may lead to apparently significant differences in the level of the second parameter dependence on the SFR. By imposing cuts on the mock sample that were more similar to the ones used to form the NewH α dataset, we found a weaker SFR dependence more consistent with the one reported here. Further work is needed to reconcile these results with recent studies based on IFU and drift-scan observations of local galaxies which find that there is no secondary dependence on the SFR (Sánchez et al. 2013; Hughes et al. 2013).

We also examined potential issues in our fitting analysis, and the lessons learned here are of use for future M_{\star} - Z -SFR studies. For example, we find that the PCA technique is highly sensitive to outliers and measurement uncertainties, and three-dimensional χ^2 minimization may be preferred as a more robust plane-fitting technique. This is particularly true for the sample size analysis described above, as there are significant numbers of true outliers in the SDSS dataset.

We conclude that future work should include the following. Locally, the SDSS galaxies excluded by the Lar13 analysis should be examined more closely, and potential systematics in SFR and Z measurements due to SDSS aperture effects can be verified directly with forthcoming integral field spectroscopic surveys (e.g., MaNGA and SAMI). Future works, particularly those based on higher redshift samples, should also account for dataset limitations in constraining a possible weak secondary dependence in the SFR. Here, we have addressed the effects of small sample size, but limited coverage of parameter space and relatively large measurement uncertainties may also have biasing effects. Finally, we stress the need for a non-parametric method of fitting a three-dimensional dataset in order to truly determine an M_{\star} - Z -SFR relation without making assumptions about the shape or functional form of the relation.

This work is based on observations obtained with MegaPrime/MegaCam, a joint project of CFHT and CEA/DAPNIA, at the CFHT, which is operated by the National Research Council of Canada, the Institut National des Science de l'Univers of the Centre National de la Recherche Scientifique of France, and the University of Hawaii. We thank Sebastien Foucaud for facilitating access to publicly available CFHT u -band data in the SXDS field, Victor Villar for providing data from his paper, and Robert Yates for providing their best-fit projection for their local fundamental metallicity relation. We also thank Brett A. Andrews for his insightful comments and discussion. Our work is based in part on observations made with the NASA's GALEX mission. We acknowledge support for this work from the GALEX Guest Investigator program under NASA grants NNG09EG72I and NNX10AF04G.

Facilities: Mayall (NEWFIRM), Subaru (Suprime-Cam), Magellan (IMACS), GALEX.

REFERENCES

- Andrews, B. H., & Martini, P. 2013, *ApJ*, 765, 140
- Autry, R. G., Probst, R. G., Starr, B. M., et al. 2003, *Proc. SPIE*, 4841, 525
- Baldwin, J. A., Phillips, M. M., & Terlevich, R. 1981, *PASP*, 93, 5
- Belli, S., Jones, T., Ellis, R. S., & Richard, J. 2013, *ApJ*, 772, 141
- Berg, D. A., Skillman, E. D., Marble, A. R., et al. 2012, *ApJ*, 754, 98
- Bertin, E., & Arnouts, S. 1996, *A&AS*, 117, 393
- Boulaide, O., Charlot, X., Abbon, P., et al. 2003, *Proc. SPIE*, 4841, 72
- Brinchmann, J., Charlot, S., White, S. D. M., et al. 2004, *MNRAS*, 351, 1151
- Brown, W. R., Kewley, L. J., & Geller, M. J. 2008, *AJ*, 135, 92
- Bruzual, G., & Charlot, S. 2003, *MNRAS*, 344, 1000
- Caffau, E., Ludwig, H.-G., Steffen, M., Freytag, B., & Bonifacio, P. 2011, *Sol. Phys.*, 268, 255
- Calzetti, D., Kinney, A. L., & Storchi-Bergmann, T. 1994, *ApJ*, 429, 582
- Chabrier, G. 2003, *PASP*, 115, 763 ([Chabrier](#))
- Charlot, S., & Fall, S. M. 2000, *ApJ*, 539, 718
- Conroy, C., Gunn, J. E., & White, M. 2009, *ApJ*, 699, 486
- Cowie, L. L., & Barger, A. J. 2008, *ApJ*, 686, 72
- Cresci, G., Mannucci, F., Sommariva, V., et al. 2012, *MNRAS*, 421, 262
- da Cunha, E., Charlot, S., & Elbaz, D. 2008, *MNRAS*, 388, 1595
- Davé, R., Finlator, K., & Oppenheimer, B. D. 2011, *MNRAS*, 416, 1354
- Davis, M., Faber, S. M., Newman, J., et al. 2003, *Proc. SPIE*, 4834, 161
- Dopita, M. A., Sutherland, R. S., Nicholls, D. C., Kewley, L. J., & Vogt, F. P. A. 2013, *ApJS*, 208, 10
- Dressler, A., Hare, T., Bigelow, B. C., & Osip, D. J. 2006, *Proc. SPIE*, 6269
- Dutton, A. A., van den Bosch, F. C., & Dekel, A. 2010, *MNRAS*, 405, 1690
- Elbaz, D., et al. 2007, *A&A*, 468, 33
- Ellison, S. L., Patton, D. R., Simard, L., & McConnachie, A. W. 2008, *ApJ*, 672, L107
- Erb, D. K., Shapley, A. E., Pettini, M., et al. 2006, *ApJ*, 644, 813
- Forbes, J. C., Krumholz, M. R., Burkert, A., & Dekel, A. 2014, *MNRAS*, 438, 1552
- Förster Schreiber, N. M., Genzel, R., Bouché, N., et al. 2009, *ApJ*, 706, 1364
- Fujita, S. S., Ajiki, M., Shioya, Y., et al. 2003, *ApJ*, 586, L115
- Furusawa, H., Kosugi, G., Akiyama, M., et al. 2008, *ApJS*, 176, 1
- González, V., Labbé, I., Bouwens, R. J., et al. 2010, *ApJ*, 713, 115
- Heckman, T. M. 1980, *A&A*, 87, 152
- Henry, A., Martin, C. L., Finlator, K., & Dressler, A. 2013a, *ApJ*, 769, 148
- Henry, A., Scarlata, C., Domínguez, A., et al. 2013b, *ApJ*, 776, L27
- Hu, E. M., Cowie, L. L., Kakazu, Y., & Barger, A. J. 2009, *ApJ*, 698, 2014
- Hughes, T. M., Cortese, L., Boselli, A., Gavazzi, G., & Davies, J. I. 2013, *A&A*, 550, A115
- Hunt, L., Magrini, L., Galli, D., et al. 2012, *MNRAS*, 427, 906
- Juneau, S., Dickinson, M., Alexander, D. M., & Salim, S. 2011, *ApJ*, 736, 104
- Kakazu, Y., Cowie, L. L., & Hu, E. M. 2007, *ApJ*, 668, 853
- Kauffmann, G., Heckman, T. M., Tremonti, C., et al. 2003, *MNRAS*, 346, 1055
- Kennicutt, R. C., Jr. 1998, *ARA&A*, 36, 189
- Kennicutt, R. C., Jr., Lee, J. C., Funes, S. J., José G., Sakai, S., & Akiyama, S. 2008, *ApJS*, 178, 247
- Kewley, L. J., Ellison, S. L. 2008, *ApJ*, 681, 1183
- Kobulnicky, H. A., & Kewley, L. J. 2004, *ApJ*, 617, 240 ([KK04](#))
- Komatsu, E., Smith, K. M., Dunkley, J., et al. 2011, *ApJS*, 192, 18
- Kong, X., Charlot, S., Brinchmann, J., & Fall, S. M. 2004, *MNRAS*, 349, 769
- Lamareille, F., Brinchmann, J., Contini, T., et al. 2009, *A&A*, 495, 53
- Lara-López, M. A., et al. 2010, *A&A*, 521, L53 ([Lar10](#))
- Lara-López, M. A., López-Sánchez, A. R., Hopkins, A. M. 2013, *ApJ*, 764, 178 ([Lar13](#))
- Lee, J. C., Gil de Paz, A., Kennicutt, R. C., Jr., et al. 2011, *ApJS*, 192, 6
- Lee, J. C., Ly, C., Spitler, L., et al. 2012, *PASP*, 124, 782
- Lilly, S. J., Carollo, C. M., Pipino, A., Renzini, A., & Peng, Y. 2013, *ApJ*, 772, 119
- Ly, C., Lee, J. C., Dale, D. A., et al. 2011a, *ApJ*, 726, 109
- Ly, C., Malkan, M. A., Hayashi, M., et al. 2011b, *ApJ*, 735, 91
- Ly, C., Malkan, M. A., Kashikawa, N., et al. 2007, *ApJ*, 657, 738
- Ly, C., Malkan, M. A., Kashikawa, N., et al. 2012, *ApJ*, 747, L16
- Ly, C., Malkan, M. A., Nagao, T., et al. 2014, *ApJ*, 780, 122
- Ly, C., Malkan, M. A., Treu, T., et al. 2009, *ApJ*, 697, 1410
- Madau, P. 1995, *ApJ*, 441, 18
- Maiolino, R., Nagao, T., Grazian, A., et al. 2008, *A&A*, 488, 463
- Mannucci, F., Cresci, G., Maiolino, R., et al. 2009, *MNRAS*, 398, 1915
- Mannucci, F., Cresci, G., Maiolino, R., Marconi, A., Gnerucci, A. 2010, *MNRAS*, 408, 2115 ([Man10](#))
- Mannucci, F., Salvaterra, R., & Campisi, M. A. 2011, *MNRAS*, 414, 1263
- Maraston, C. 2005, *MNRAS*, 362, 799
- Markwardt, C. B. 2009, in *ASP Conf. Ser. 411, Astrophysical Data Analysis Software and Systems XVIII*, ed. D. A. Bohlender, D. Durand, & P. Dowler (San Francisco, CA: ASP), 251
- Martin, D. C., Fanson, J., Schiminovich, D., et al. 2005, *ApJ*, 619, L1
- Masters, D., McCarthy, P., Siana, B., et al. 2014, *ApJ*, 785, 153
- McGaugh, S. S. 1991, *ApJ*, 380, 140 ([M91](#))
- Miyazaki, S., Komiya, Y., Sekiguchi, M., et al. 2002, *PASJ*, 54, 833
- Momcheva, I. G., Lee, J. C., Ly, C., et al. 2013, *AJ*, 145, 47
- Morrissey, P., Conrow, T., Barlow, T. A., et al. 2007, *ApJS*, 173, 682
- Moustakas, J., et al. 2011, *ApJ*, submitted (arXiv:1112.3300)
- Nagao, T., Maiolino, R., & Marconi, A. 2006, *A&A*, 459, 85
- Nicholls, D. C., Dopita, M. A., & Sutherland, R. S. 2012, *ApJ*, 752, 148
- Nicholls, D. C., Dopita, M. A., Sutherland, R. S., Kewley, L. J., & Palay, E. 2013, *ApJS*, 207, 21
- Noeske, K. G., Weiner, B. J., Faber, S. M., et al. 2007, *ApJ*, 660, L43
- O'Donnell, J. E. 1994, *ApJ*, 422, 158
- Oke, J. B. 1974, *ApJS*, 27, 21
- Pagel, B. E. J., Edmunds, M. G., Blackwell, D. E., Chun, M. S., & Smith, G. 1979, *MNRAS*, 189, 95
- Peeples, M. S., Pogge, R. W., & Stanek, K. Z. 2008, *ApJ*, 685, 904
- Peeples, M. S., & Shankar, F. 2011, *MNRAS*, 417, 2962
- Peeples, M. S., Werk, J. K., Tumlinson, J., et al. 2014, *ApJ*, 786, 54
- Pérez-Montero, E., Contini, T., Lamareille, F., et al. 2013, *A&A*, 549, A25
- Persson, S. E., Barkhouser, R., Birk, C., et al. 2008, *Proc. SPIE*, 7014, 70142V
- Pettini, M., & Pagel, B. E. J. 2004, *MNRAS*, 348, L59
- Probst, R. G., George, J. R., Daly, P. N., Don, K., & Ellis, M. 2008, *Proc. SPIE*, 7014
- Reddy, N. A., Steidel, C. C., Pettini, M., et al. 2008, *ApJS*, 175, 48
- Richard, J., Jones, T., Ellis, R., et al. 2011, *MNRAS*, 413, 643
- Rodrigues, M., Hammer, F., Flores, H., et al. 2008, *A&A*, 492, 371
- Salim, S., Dickinson, M., Michael Rich, R., et al. 2009, *ApJ*, 700, 161
- Salim, S., & Lee, J. C. 2012, *ApJ*, 758, 134
- Salim, S., Rich, R. M., Charlot, S., et al. 2007, *ApJS*, 173, 267
- Salpeter, E. E. 1955, *ApJ*, 121, 161
- Sánchez, S. F., Rosales-Ortega, F. F., Jungwiert, B., et al. 2013, *A&A*, 554, A58
- Savaglio, S., Glazebrook, K., Le Borgne, D., et al. 2005, *ApJ*, 635, 260
- Schlegel, D. J., Finkbeiner, D. P., & Davis, M. 1998, *ApJ*, 500, 525
- Shioya, Y., Taniguchi, Y., Sasaki, S. S., et al. 2008, *ApJS*, 175, 128
- Sobral, D., Best, P. N., Geach, J. E., et al. 2009, *MNRAS*, 398, 75
- Stott, J. P., Sobral, D., Bower, R., et al. 2013, *MNRAS*, 2311
- Taylor, E. N., Hopkins, A. M., Baldry, I. K., et al. 2011, *MNRAS*, 418, 1587
- Torrey, P., Cox, T. J., Kewley, L., & Hernquist, L. 2012, *ApJ*, 746, 108

- Tremaine, S., Gebhardt, K., Bender, R., et al. 2002, ApJ, 574, 740
 Tremonti, C., et al. 2004, ApJ, 613, 898 (T04)
 Vibert, D., Zamojski, M., Conseil, S., et al. 2009, Proc. SPIE, 7246
 Villar, V., Gallego, J., Pérez-González, P. G., et al. 2008, ApJ, 677, 169
 Villar, V., Gallego, J., Pérez-González, P. G., et al. 2011, ApJ, 740, 47
 Whitaker, K. E., van Dokkum, P. G., Brammer, G., Franx, M. 2012, ApJ, 754, L29
 Whitaker, K. E., Franx, M., Leja, J., et al. 2014, ApJ, submitted (arXiv:1407.1843)
 Xia, L., Malhotra, S., Rhoads, J., et al. 2012, AJ, 144, 28
 Yabe, K., Ohta, K., Iwamuro, F., et al. 2012, PASJ, 64, 60
 Yabe, K., Ohta, K., Iwamuro, F., et al. 2014, MNRAS, 437, 3647
 Yates, R. M., Kauffmann, G., Guo, Q. 2012, MNRAS, 422, 215 (Yat12)
 York, D. G., Adelman, J., Anderson, J. E., Jr., et al. 2000, AJ, 120, 1579
 Zahid, H. J., Kewley, L. J., & Bresolin, F. 2011, ApJ, 730, 137
 Zahid, H. J., Geller, M. J., Kewley, L. J., et al. 2013a, ApJ, 771, L19
 Zahid, H. J., Kashino, D., Silverman, J. D., et al. 2013b, ApJ, in press (arXiv:1310.4950)
 Zaritsky, D., Kennicutt, R. C., Jr., & Huchra, J. P. 1994, ApJ, 420, 87 (Z94)

TABLE 1
 NEWFIRM PHOTOMETRY OF H α -SELECTED $z = 0.8$ GALAXIES

ID (1)	R.A. (J2000) (2)	Dec. (J2000) (3)	z (4)	m_J (5)	m_{NB118} (6)	Line flux (7)	NB EW (8)	[N II]/H α (9)	$\log(L_{\text{H}\alpha})$ (10)
SXDSN-12615	2 17 17.7	-4 45 18.9	0.796	21.46±0.07	20.79±0.05	19.6±2.0	56±17	0.27	41.660
SXDSN-14848	2 18 09.7	-4 42 25.1	0.805	22.96±0.24	21.83±0.09	10.6±1.7	125±94	0.40	41.364
SXDSN-17153	2 17 29.1	-4 47 11.4	0.797	20.56±0.02	19.90±0.01	41.5±1.5	48±5	0.38	41.953
SXDSN-17287	2 18 11.5	-4 47 01.0	0.805	22.75±0.22	21.99±0.13	7.2±1.9	68±62	0.35	41.213
SXDSN-18372	2 18 11.6	-4 46 17.3	0.804	21.52±0.07	20.94±0.05	14.8±1.9	43±16	0.31	41.537
SXDSN-18643	2 18 20.5	-4 46 06.6	0.804	21.18±0.04	20.71±0.03	15.3±1.7	32±9	0.41	41.519
SXDSN-18689	2 18 05.2	-4 46 05.9	0.805	21.67±0.06	21.03±0.04	15.4±1.4	53±15	0.37	41.536
SXDSN-18825	2 17 24.3	-4 45 55.8	0.797	22.70±0.16	22.22±0.12	3.5±1.6	29±33	0.31	40.908
SXDSN-19419	2 18 20.1	-4 36 46.9	0.806	21.14±0.05	20.73±0.04	13.2±2.0	26±10	0.41	41.459
SXDSN-19725	2 18 18.3	-4 36 28.1	0.805	21.16±0.05	20.13±0.02	48.2±1.8	108±17	0.33	42.044
SXDSN-19822	2 17 43.0	-4 36 25.0	0.783	18.63	18.23	116.3±1.9	22	0.49	42.349
SXDSN-20554	2 18 49.0	-4 35 21.6	0.807	23.06±0.24	22.06±0.11	8.1±1.5	106±85	0.47	41.231
SXDSN-20774	2 17 49.4	-4 44 23.3	0.811	23.20±0.25	22.21±0.11	6.9±1.4	97±84	0.42	41.177
SXDSN-20874	2 17 39.8	-4 34 56.1	0.802	22.44±0.12	21.62±0.06	10.2±1.4	69±33	0.39	41.345
SXDSN-22048	2 18 13.1	-4 43 31.1	0.804	22.55±0.18	21.53±0.09	12.8±2.0	98±63	0.19	41.515
SXDSN-22485	2 18 43.2	-4 32 35.7	0.800	21.33±0.05	20.81±0.03	15.3±1.5	37±10	0.37	41.526
SXDSN-23784	2 18 07.1	-4 30 49.3	0.799	21.47±0.05	20.82±0.03	18.3±1.4	51±12	0.37	41.603
SXDSN-23860	2 18 12.3	-4 42 00.3	0.808	22.40±0.16	21.22±0.06	19.4±1.9	142±69	0.45	41.615
SXDSN-24371	2 18 48.6	-4 41 43.4	0.806	20.71±0.03	19.71±0.01	67.6±1.7	94±9	0.50	42.142
SXDSN-24458	2 18 48.6	-4 41 34.6	0.807	22.05±0.10	20.89±0.04	25.1±1.7	124±39	0.42	41.736
SXDSN-24652	2 18 11.5	-4 41 22.9	0.808	>23.51	22.29±0.16	7.4±3.1	>151	0.07	41.326
SXDSN-24723	2 19 01.1	-4 41 27.1	0.805	22.13±0.10	21.61±0.07	6.7±1.7	32±21	0.39	41.167
SXDSN-24979	2 18 21.1	-4 41 09.2	0.805	23.00±0.23	22.47±0.16	2.8±1.7	29±45	0.38	40.798
SXDSN-25202	2 18 09.0	-4 40 56.5	0.808	22.01±0.09	21.25±0.05	14.1±1.6	67±25	0.24	41.544
SXDSN-26559	2 18 06.7	-4 39 48.2	0.817	21.99±0.08	21.52±0.06	7.5±1.4	34±17	0.48	41.210
SXDSN-26798	2 18 23.5	-4 39 35.0	0.813	>23.38	22.54±0.17	4.5±2.9	>75	0.20	41.076
SXDSN-26828	2 18 24.8	-4 39 35.8	0.814	22.88±0.20	22.14±0.12	5.4±1.7	50±48	0.22	41.145
SXDSN-27037	2 18 07.4	-4 39 22.3	0.813	22.22±0.11	21.48±0.06	11.4±1.4	66±28	0.51	41.374
SXDSN-28032	2 18 03.0	-4 38 31.2	0.804	22.09±0.09	21.05±0.04	20.0±1.5	99±30	0.12	41.736
SXDSN-28267	2 18 03.2	-4 38 19.5	0.805	21.92±0.08	20.46±0.02	43.6±1.5	221±49	0.15	42.066
SXDSN-29887	2 19 01.2	-4 37 15.2	0.807	22.37±0.19	21.89±0.13	4.9±2.4	29±37	0.33	41.049
SXDSN-30551	2 17 46.9	-4 36 40.1	0.803	21.61±0.07	20.85±0.04	20.4±1.8	68±19	0.29	41.683
SXDSN-31207	2 18 51.0	-4 36 06.3	0.807	21.58±0.08	20.72±0.04	24.8±2.0	78±22	0.51	41.703
SXDSN-31304	2 18 51.2	-4 36 06.4	0.806	19.88±0.02	19.26±0.01	64.1±2.1	37±3	0.50	42.119
SXDSN-31331	2 18 52.2	-4 36 09.5	0.807	20.25±0.12	20.02±0.11	14.9±11.3	13±21	0.51	41.484
SXDSN-31929	2 17 54.6	-4 35 16.9	0.807
SXDSN-32915	2 17 37.6	-4 34 08.1	0.801	22.73±0.16	22.07±0.09	6.0±1.4	55±40	0.38	41.120
SXDSN-33371	2 19 03.3	-4 33 38.3	0.805	21.75±0.08	21.43±0.06	5.6±1.7	19±14	0.23	41.142
SXDSN-34057	2 17 41.3	-4 32 39.0	0.810	>23.55	22.51±0.15	5.2±1.8	>99	0.39	41.067
SXDSN-34591	2 18 47.4	-4 32 06.2	0.807	22.46±0.13	21.84±0.08	7.1±1.4	50±31	0.41	41.190
SXDSN-34643	2 18 01.2	-4 31 60.0	0.816	22.83±0.17	22.13±0.10	5.3±1.5	47±40	0.26	41.123
SXDSN-34925	2 18 59.8	-4 31 45.2	0.805	21.84±0.07	21.30±0.05	9.9±1.5	38±16	0.19	41.407
SXDSN-35304	2 17 37.5	-4 31 17.5	0.803	22.44±0.12	21.61±0.06	10.8±1.4	77±35	0.22	41.430
SXDSN-35455	2 18 10.4	-4 31 09.9	0.800	22.13±0.11	21.35±0.06	13.0±1.7	68±31	0.37	41.456
SXDSN-35945	2 18 22.5	-4 30 36.1	0.823	21.00±0.19	20.74±0.23	9.0±10.2	16±41	0.46	41.302
SXDSN-36476	2 17 58.1	-4 29 53.2	0.798	22.85±0.17	22.24±0.11	4.8±1.4	48±42	0.18	41.083
SXDSN-37348	2 17 59.2	-4 28 46.8	0.800	23.02±0.14	22.13±0.15	6.9±1.4	83±56	0.28	41.214
SXDSN-37430	2 18 13.6	-4 28 43.4	0.804	22.41±0.14	21.52±0.07	12.5±1.7	88±46	0.41	41.433
SXDSN-38796	2 18 36.4	-4 27 13.9	0.792	19.84±0.01	19.58±0.01	27.8±1.6	17±2	0.52	41.732
SXDSN-39242	2 18 16.6	-4 26 34.4	0.803	>23.48	21.94±0.09	11.4±1.7	>249	0.15	41.479
SXDSN-39615	2 17 35.2	-4 26 07.9	0.791	22.00±0.08	21.63±0.06	5.0±1.5	22±15	0.18	41.097
SXDSN-39807	2 17 24.8	-4 25 52.1	0.791	22.69±0.16	22.17±0.11	4.5±1.4	39±34	0.27	41.020
SXDSN-41162	2 18 25.6	-4 24 13.9	0.802	23.01±0.23	21.70±0.08	13.0±1.6	166±112	0.10	41.553
SXDSN-41683	2 17 31.5	-4 23 39.8	0.790	21.73±0.07	21.39±0.05	6.4±1.5	22±12	0.37	41.135
SXDSN-41684	2 17 45.6	-4 23 31.7	0.785
SXDSS-8347	2 18 19.9	-5 28 55.3	0.805
SXDSS-12333	2 17 36.9	-5 26 47.5	0.802

TABLE 1 — *Continued*

ID (1)	R.A. (J2000) (2)	Dec. (J2000) (3)	z (4)	m_J (5)	m_{NB118} (6)	Line flux (7)	NB EW (8)	[N II]/H α (9)	$\log(L_{\text{H}\alpha})$ (10)
SXDSS-12862	2 17 18.7	-5 26 30.4	0.803	21.35±0.06	20.81±0.05	12.8±2.4	28±13	0.51	41.410
SXDSS-14115	2 17 51.8	-5 25 37.5	0.802	22.20±0.15	21.34±0.09	13.7±2.4	75±45	0.36	41.487
SXDSS-14438	2 17 30.3	-5 25 15.1	0.809
SXDSS-14722	2 17 37.7	-5 25 01.6	0.817
SXDSS-15629	2 17 28.8	-5 24 21.1	0.807	22.79±0.24	22.09±0.18	5.4±2.3	46±59	0.33	41.094
SXDSS-15945	2 18 29.5	-5 24 07.3	0.807	22.49±0.20	21.93±0.16	4.6±2.6	29±42	0.30	41.041
SXDSS-16362	2 16 43.0	-5 23 52.0	0.789
SXDSS-16423	2 16 59.8	-5 23 39.3	0.802	23.14	22.89	1.0	12	0.29	40.368
SXDSS-16739	2 18 34.0	-5 23 27.5	0.807	20.81±0.05	20.46±0.06	12.1±3.3	16±10	0.29	41.460
SXDSS-16866	2 17 25.4	-5 23 11.0	0.809	>23.14	>22.61	2.7±5.7	>32	0.29	40.809
SXDSS-17510	2 16 51.4	-5 22 42.3	0.800	22.31±0.16	21.92±0.16	3.2±2.6	17±31	0.18	40.914
SXDSS-17705	2 17 02.6	-5 22 27.0	0.803	22.89±0.30	21.82±0.14	10.0±2.5	104±108	0.14	41.426
SXDSS-17733	2 16 52.5	-5 22 30.5	0.802	20.66±0.04	20.11±0.03	29.0±2.4	37±8	0.33	41.819
SXDSS-17787	2 16 43.1	-5 22 22.9	0.794
SXDSS-17924	2 16 51.3	-5 22 17.8	0.801	22.52±0.20	21.52±0.11	11.6±2.5	76±58	0.26	41.445
SXDSS-17941	2 16 46.3	-5 22 15.9	0.795
SXDSS-17958	2 17 18.6	-5 22 16.0	0.809	22.97±0.28	21.81±0.13	10.7±2.2	123±114	0.18	41.451
SXDSS-18093	2 16 50.9	-5 22 04.2	0.802
SXDSS-18211	2 17 33.4	-5 22 02.7	0.809	21.13±0.03	20.81±0.04	8.9±1.8	17±7	0.29	41.327
SXDSS-18370	2 16 45.6	-5 21 58.5	0.794	20.96±0.06	20.67±0.06	9.3±2.9	15±10	0.11	41.394
SXDSS-18554	2 17 19.2	-5 21 42.3	0.808	>23.14	22.29±0.21	5.6±3.0	>73	0.18	41.168
SXDSS-18604	2 16 49.0	-5 21 38.4	0.802
SXDSS-18617	2 16 49.5	-5 21 39.0	0.795	23.14	22.36	4.8	59	0.13	41.095
SXDSS-18709	2 16 45.8	-5 21 32.6	0.802	23.14±0.09	23.41±0.10
SXDSS-19166	2 16 50.9	-5 21 15.1	0.802	20.75±0.04	20.28±0.04	21.1±2.6	28±9	0.43	41.652
SXDSS-19596	2 16 46.7	-5 20 50.0	0.794	21.61±0.09	21.10±0.08	11.2±2.6	34±21	0.29	41.409
SXDSS-20389	2 17 14.3	-5 20 01.0	0.801	23.14±0.06	22.97±0.09
SXDSS-20452	2 17 16.6	-5 20 04.5	0.809	21.23±0.06	20.55±0.04	22.2±2.3	46±14	0.51	41.659
SXDSS-20675	2 16 53.9	-5 19 49.0	0.805	22.27±0.14	21.52±0.10	9.2±2.3	47±35	0.51	41.271
SXDSS-21192	2 17 11.5	-5 19 16.3	0.803	23.14±0.27	22.70±0.22	2.2±1.8	27±55	0.12	40.771
SXDSS-21634	2 17 29.8	-5 19 06.7	0.808	22.27±0.14	21.44±0.09	11.8±2.2	66±41	0.11	41.518
SXDSS-21685	2 16 52.9	-5 18 59.3	0.798	20.57±0.03	20.23±0.03	16.4±2.4	19±6	0.29	41.580
SXDSS-21861	2 16 46.1	-5 18 41.7	0.801	22.56±0.21	21.27±0.09	19.1±2.5	157±102	0.24	41.665
SXDSS-21905	2 16 48.4	-5 18 42.5	0.801	20.39±0.03	19.90±0.02	25.9±2.5	23±5	0.46	41.730
SXDSS-22205	2 16 43.9	-5 18 26.6	0.801	22.28±0.22	21.37±0.11	13.4±3.1	77±65	0.30	41.494
SXDSS-22262	2 16 48.0	-5 18 23.5	0.802	20.95±0.12	20.75±0.16	3.8±7.6	5±23	0.29	40.948
SXDSS-22277	2 17 03.6	-5 18 19.4	0.801	22.65±0.20	21.90±0.14	6.7±2.2	51±51	0.25	41.212
SXDSS-22355	2 17 09.1	-5 18 18.0	0.801	21.10±0.05	20.55±0.04	18.3±2.3	33±11	0.35	41.612
SXDSS-22389	2 16 47.4	-5 18 14.0	0.800	22.22±0.14	21.51±0.11	10.1±2.3	55±38	0.29	41.372
SXDSS-22452	2 16 56.8	-5 18 10.5	0.800	22.27±0.14	21.53±0.10	9.7±2.2	54±37	0.04	41.449
SXDSS-22538	2 17 08.6	-5 18 08.1	0.809	22.03±0.12	21.11±0.07	16.5±2.3	71±34	0.48	41.538
SXDSS-22557	2 16 47.8	-5 18 01.6	0.799	>23.14	>22.45	3.6±13.5	>41	...	40.931
SXDSS-22717	2 16 46.0	-5 17 55.6	0.801	22.36±0.18	21.54±0.11	10.5±2.5	64±49	0.29	41.391
SXDSS-22728	2 16 45.2	-5 18 03.5	0.801	20.21±0.03	19.27±0.02	96.3±2.7	82±8	0.37	42.327
SXDSS-22887	2 17 50.8	-5 17 43.5	0.805	>23.05	22.23±0.20	5.9±2.6	>71	0.29	41.148
SXDSS-22991	2 16 43.1	-5 17 51.7	0.801
SXDSS-23082	2 17 06.7	-5 17 35.8	0.810	22.63±0.08	22.86±0.11
SXDSS-23167	2 17 07.7	-5 17 27.2	0.809	23.14±0.07	22.41±0.10	4.1±0.8	49±25	0.21	41.026
SXDSS-23384	2 17 21.9	-5 17 19.6	0.802	22.60±0.20	21.41±0.09	15.0±2.3	113±74	0.29	41.548
SXDSS-23393	2 17 21.8	-5 17 24.4	0.802	20.76±0.04	19.57±0.02	85.7±2.3	130±15	0.38	42.274
SXDSS-23571	2 16 52.8	-5 17 09.3	0.805	21.84±0.10	21.20±0.08	10.7±2.3	37±22	0.29	41.404
SXDSS-23647	2 16 53.1	-5 17 06.7	0.801	21.66±0.08	20.62±0.05	29.5±2.2	97±29	0.33	41.826
SXDSS-23665	2 16 51.5	-5 17 04.8	0.806	21.94±0.11	20.88±0.06	22.2±2.3	87±34	0.29	41.722
SXDSS-23667	2 16 54.0	-5 17 07.4	0.803	21.77±0.09	20.98±0.06	16.8±2.2	58±24	0.45	41.549
SXDSS-23807	2 17 36.6	-5 16 56.4	0.801
SXDSS-24027	2 17 05.4	-5 16 45.9	0.808	22.14±0.13	21.17±0.08	17.4±2.2	91±45	0.16	41.668
SXDSS-24055	2 17 48.6	-5 16 41.4	0.804	22.66±0.23	21.85±0.15	8.2±2.3	69±67	0.29	41.289
SXDSS-24177	2 17 13.3	-5 16 34.7	0.815	22.19±0.15	21.67±0.12	6.6±2.4	34±33	0.29	41.206
SXDSS-24469	2 16 52.2	-5 16 14.6	0.803
SXDSS-24527	2 17 17.7	-5 16 14.6	0.815	21.72±0.10	21.38±0.10	5.5±2.7	18±21	0.29	41.131
SXDSS-24609	2 16 53.9	-5 16 15.7	0.804	20.59±0.04	19.63±0.02	70.1±2.6	86±11	0.46	42.165
SXDSS-26461	2 17 02.6	-5 15 10.5	0.804	22.82±0.07	21.89±0.09	8.2±1.1	76±30	0.29	41.290
SXDSS-26565	2 16 54.1	-5 15 08.4	0.803	>22.88	22.02±0.20	7.3±3.2	>74	0.09	41.304
SXDSS-26597	2 16 59.9	-5 15 08.0	0.808	21.83±0.16	21.19±0.10	12.3±3.4	46±38	0.38	41.441
SXDSS-26724	2 16 55.3	-5 15 04.4	0.803	>22.78	21.57±0.14	13.3±3.5	>120	0.31	41.491
SXDSS-27335	2 16 56.3	-5 14 35.7	0.802	>23.12	21.95±0.15	9.3±2.5	>117	0.27	41.347
SXDSS-27364	2 16 56.1	-5 14 32.4	0.802
SXDSS-27425	2 16 45.4	-5 14 30.2	0.802	>23.12	21.83±0.16	11.3±3.4	>155	0.29	41.424
SXDSS-27514	2 17 31.0	-5 14 26.7	0.816	21.46±0.15	21.29±0.19	2.3±5.6	5±28	0.29	40.753
SXDSS-27584	2 16 45.7	-5 14 23.2	0.802	21.67±0.12	21.21±0.08	6.7±3.1	19±20	0.29	41.198
SXDSS-27730	2 17 26.6	-5 14 21.4	0.823	21.20±0.02	21.18±0.02
SXDSS-27769	2 16 59.2	-5 14 17.5	0.808	21.66±0.09	20.76±0.05	23.8±2.3	78±28	0.29	41.756
SXDSS-27865	2 17 03.2	-5 14 08.8	0.803	21.85±0.11	21.38±0.08	7.8±2.3	29±23	0.29	41.265
SXDSS-27927	2 17 25.4	-5 14 02.2	0.803	22.73±0.23	21.94±0.13	6.9±2.1	57±58	0.29	41.211
SXDSS-28010	2 17 03.8	-5 13 56.4	0.803	22.86	22.38	2.9	26	0.29	40.838

TABLE 1 — *Continued*

ID (1)	R.A. (J2000) (2)	Dec. (J2000) (3)	z (4)	m_J (5)	m_{NB118} (6)	Line flux (7)	NB EW (8)	[N II]/H α (9)	$\log(L_{\text{H}\alpha})$ (10)
SXDSS-28369	2 16 55.0	-5 13 44.0	0.802	21.36±0.07	20.75±0.04	17.7±2.1	43±15	0.49	41.556
SXDSS-28490	2 17 17.0	-5 13 31.6	0.802	22.41±0.17	22.13±0.15	1.9±2.3	11±28	0.29	40.640
SXDSS-28526	2 17 04.1	-5 13 32.8	0.804	21.91±0.11	21.18±0.07	12.6±2.3	48±26	0.34	41.457
SXDSS-28810	2 16 56.1	-5 13 21.9	0.803	20.72±0.04	20.35±0.03	15.9±2.2	21±7	0.29	41.576
SXDSS-28845	2 16 55.3	-5 13 20.0	0.803	20.56±0.03	19.91±0.02	37.6±2.2	41±7	0.29	41.948
SXDSS-28926	2 17 17.5	-5 13 07.1	0.802	23.12±0.03	22.63±0.03
SXDSS-29206	2 17 04.6	-5 12 55.3	0.813	>23.01	22.19±0.18	6.0±2.2	>68	0.19	41.197
SXDSS-29259	2 16 53.8	-5 12 52.6	0.808
SXDSS-29322	2 16 51.9	-5 12 55.7	0.808	20.70±0.07	20.47±0.06	7.4±4.4	9±11	0.29	41.250
SXDSS-29327	2 16 51.7	-5 12 51.2	0.811	21.16±0.05	20.74±0.04	11.3±2.3	21±10	0.49	41.374
SXDSS-29607	2 16 52.2	-5 12 34.9	0.806	21.92±0.11	21.59±0.09	4.5±2.2	17±20	0.29	41.028
SXDSS-29646	2 16 48.7	-5 12 35.7	0.805	21.67±0.09	21.09±0.06	11.3±2.3	34±18	0.29	41.429
SXDSS-29754	2 17 15.0	-5 12 29.2	0.802	21.14±0.05	20.66±0.04	15.6±2.2	30±11	0.29	41.564
SXDSS-29859	2 17 59.1	-5 12 21.9	0.801	>23.18	22.15±0.16	7.5±2.3	>105	0.14	41.296
SXDSS-29972	2 16 51.6	-5 12 14.5	0.803	22.98±0.28	22.19±0.16	5.8±2.1	63±76	0.29	41.135
SXDSS-30051	2 17 44.9	-5 12 20.0	0.802	20.64±0.03	19.92±0.02	44.9±2.1	58±8	0.50	41.959
SXDSS-30124	2 18 08.5	-5 12 05.8	0.797	23.00±0.16	22.58±0.14	2.5±1.2	27±34	0.06	40.842
SXDSS-30142	2 17 17.0	-5 12 11.9	0.802	20.29±0.02	19.56±0.01	61.6±2.1	56±6	0.47	42.106
SXDSS-30295	2 18 20.1	-5 11 53.3	0.796	22.59±0.19	21.90±0.13	6.8±2.1	53±49	0.14	41.250
SXDSS-31496	2 16 51.7	-5 10 44.8	0.808	22.39±0.11	21.75±0.11	6.8±2.2	40±38	0.42	41.171
SXDSS-32097	2 17 58.0	-5 10 18.9	0.800	21.25±0.06	20.24±0.03	42.6±2.1	101±20	0.41	41.959
SXDSS-32132	2 17 17.6	-5 10 15.0	0.798	>21.17	20.78±0.17	8.7±15.6	>16	0.28	41.310
SXDSS-32277	2 17 21.3	-5 10 09.9	0.802	21.54±0.08	20.22±0.03	48.7±2.3	143±34	0.32	42.048
SXDSS-32372	2 17 44.3	-5 10 04.5	0.801	21.60±0.08	21.19±0.07	6.9±2.4	19±15	0.29	41.209
SXDSS-33021	2 17 28.6	-5 09 25.1	0.802	22.13±0.13	21.67±0.10	5.8±2.1	28±27	0.28	41.136
SXDSS-33298	2 18 01.2	-5 09 18.1	0.800	21.11±0.05	20.07±0.03	50.3±2.2	105±18	0.41	42.031
SXDSS-33303	2 17 44.1	-5 09 13.7	0.804	21.98±0.12	20.97±0.06	21.2±2.2	95±39	0.29	41.701
SXDSS-33787	2 18 09.0	-5 08 41.2	0.799	23.06±0.30	22.22±0.18	6.0±2.1	74±89	0.16	41.195
SXDSS-35437	2 17 39.8	-5 07 17.2	0.803	21.75±0.13	21.00±0.07	15.4±3.0	50±30	0.51	41.490
SXDSS-35468	2 17 08.9	-5 07 15.5	0.803	22.02±0.12	21.34±0.08	10.8±2.3	47±29	0.29	41.407
SXDSS-35702	2 17 28.7	-5 07 02.9	0.801	22.68±0.22	21.32±0.07	18.4±2.2	164±106	0.29	41.634
SXDSS-35926	2 17 38.4	-5 06 47.9	0.804	22.46±0.22	21.35±0.09	15.1±2.7	98±73	0.29	41.553
SXDSS-36006	2 17 38.3	-5 06 47.5	0.803	22.10±0.16	20.81±0.06	28.4±2.8	145±71	0.40	41.792
SXDSS-36019	2 16 46.5	-5 06 48.9	0.804	21.48±0.08	20.36±0.04	38.5±2.5	104±28	0.29	41.958
SXDSS-36053	2 16 50.3	-5 06 39.8	0.805	22.71±0.22	21.75±0.11	9.7±2.2	82±69	0.40	41.328
SXDSS-36054	2 17 43.7	-5 06 42.2	0.804	21.93±0.12	21.24±0.08	12.8±2.2	54±29	0.29	41.480
SXDSS-36609	2 17 37.1	-5 06 22.2	0.803	20.36±0.03	19.21±0.01	111.5±2.7	104±10	0.43	42.376
SXDSS-36655	2 17 42.1	-5 06 11.9	0.798	21.87±0.12	21.28±0.08	10.3±2.5	39±26	0.40	41.342
SXDSS-36770	2 17 41.6	-5 06 04.3	0.799	21.78±0.12	21.00±0.06	17.5±2.5	65±31	0.46	41.556
SXDSS-36865	2 17 40.9	-5 05 57.6	0.801	22.27±0.19	21.13±0.07	19.7±2.6	118±72	0.40	41.629
SXDSS-36954	2 17 23.6	-5 05 50.4	0.800	23.12±0.06	22.61±0.07	2.3±0.5	26±14	0.06	40.818
SXDSS-36995	2 17 38.0	-5 05 54.6	0.803	21.07±0.05	20.80±0.05	5.0±2.5	8±8	0.29	41.073
SXDSS-37057	2 17 41.4	-5 05 44.5	0.800	>23.13	22.09±0.17	7.9±2.5	>106	0.30	41.260
SXDSS-37189	2 17 00.6	-5 05 35.8	0.804
SXDSS-37234	2 17 30.3	-5 05 33.9	0.800	23.00±0.29	22.15±0.15	5.6±2.2	56±71	0.05	41.208
SXDSS-37285	2 16 57.9	-5 05 39.4	0.802	21.56±0.08	20.37±0.03	40.6±2.3	122±31	0.42	41.939
SXDSS-37540	2 17 48.7	-5 05 22.6	0.799	21.81±0.10	21.09±0.07	15.4±2.2	59±27	0.38	41.526
SXDSS-37564	2 16 55.5	-5 05 18.2	0.804	22.42±0.17	21.89±0.12	4.9±2.2	29±35	0.23	41.083
SXDSS-37774	2 17 49.3	-5 05 08.6	0.799	22.07±0.13	21.15±0.07	17.4±2.2	88±42	0.44	41.561
SXDSS-37799	2 17 49.1	-5 05 08.1	0.799	21.84±0.11	21.44±0.09	6.5±2.3	25±21	0.29	41.183
SXDSS-37947	2 17 49.2	-5 04 54.4	0.801	22.46±0.19	21.88±0.13	5.4±2.3	34±39	0.29	41.104
SXDSS-37948	2 17 00.4	-5 04 51.9	0.799
SXDSS-38003	2 17 16.8	-5 04 49.0	0.804
SXDSS-38307	2 17 36.9	-5 04 34.1	0.803	23.12	22.31	4.9	58	0.47	41.007
SXDSS-38485	2 17 36.2	-5 04 33.2	0.798	21.71±0.10	21.15±0.07	11.2±2.4	37±21	0.29	41.414
SXDSS-38541	2 18 06.7	-5 04 28.5	0.801	21.83±0.10	20.95±0.06	19.3±2.2	73±29	0.46	41.601
SXDSS-38602	2 17 34.1	-5 04 24.8	0.799	21.13±0.05	20.64±0.04	15.6±2.2	29±11	0.29	41.559
SXDSS-38698	2 17 35.9	-5 04 25.8	0.800	20.34±0.03	19.37±0.01	91.4±2.4	92±9	0.51	42.260
SXDSS-38754	2 18 23.5	-5 04 11.4	0.800
SXDSS-38784	2 17 36.4	-5 04 14.4	0.799	21.33±0.07	20.79±0.05	14.5±2.5	33±15	0.29	41.527
SXDSS-39016	2 17 54.7	-5 04 05.2	0.799	21.57±0.08	20.60±0.04	28.4±2.2	84±24	0.40	41.785
SXDSS-39160	2 17 42.6	-5 03 51.5	0.802	23.18±0.05	22.41±0.04	4.8±0.4	65±15	0.42	41.008
SXDSS-39161	2 17 35.6	-5 03 55.3	0.802	20.95±0.05	20.47±0.04	18.5±2.3	30±10	0.29	41.638
SXDSS-39226	2 17 31.2	-5 03 49.3	0.802	22.00±0.12	21.10±0.06	16.9±2.1	74±33	0.51	41.531
SXDSS-39288	2 17 21.9	-5 03 49.2	0.804	21.42±0.07	20.37±0.03	37.6±2.2	100±23	0.22	41.974
SXDSS-39308	2 18 26.6	-5 03 46.4	0.799	22.97±0.23	22.17±0.31	5.5±2.9	56±83	0.19	41.144
SXDSS-39501	2 17 43.2	-5 03 31.2	0.801	23.09±0.12	22.57±0.12	2.5±1.0	27±27	0.29	40.766
SXDSS-39548	2 17 30.0	-5 03 29.5	0.799	21.84±0.10	21.28±0.07	9.3±2.2	34±21	0.15	41.384
SXDSS-39672	2 17 31.2	-5 03 18.8	0.800	22.42±0.17	21.93±0.13	4.0±2.3	23±32	0.29	40.971
SXDSS-40071	2 16 44.9	-5 03 03.1	0.802	20.69±0.05	20.22±0.03	21.0±2.9	26±9	0.50	41.629
SXDSS-40327	2 18 08.4	-5 02 36.4	0.799	22.97±0.29	22.12±0.17	6.2±2.2	65±79	0.29	41.162
SXDSS-40667	2 17 12.7	-5 02 16.1	0.806	21.92±0.12	21.63±0.08	3.1±2.3	11±18	0.43	40.822
SXDSS-41193	2 18 07.7	-5 01 47.7	0.800	22.41±0.24	21.47±0.13	12.7±3.1	82±76	0.15	41.521
SXDSS-41546	2 17 31.0	-5 01 39.6	0.799	20.46±0.04	19.95±0.03	30.2±2.9	31±7	0.29	41.848
SXDSSW-8210	2 16 51.7	-5 10 44.6	0.808	22.30±0.13	21.82±0.10	5.8±1.8	34±29	0.26	41.150

TABLE 1 — *Continued*

ID (1)	R.A. (J2000) (2)	Dec. (J2000) (3)	z (4)	m_J (5)	m_{NB118} (6)	Line flux (7)	NB EW (8)	[N II]/H α (9)	$\log(L_{H\alpha})$ (10)
SXDSW-9136	2 16 33.9	-5 10 14.8	0.806	23.24±0.28	22.01±0.11	9.3±1.6	140±123	0.18	41.384
SXDSW-10296	2 15 51.8	-5 09 47.7	0.800	21.56±0.05	20.66±0.03	26.8±1.4	84±16	0.23	41.817
SXDSW-11479	2 16 45.0	-5 09 00.2	0.804	23.44±0.31	22.08±0.10	9.4±1.5	183±167	0.30	41.344
SXDSW-11971	2 16 46.5	-5 06 49.0	0.804	21.44±0.05	20.37±0.02	39.3±1.5	114±19	0.23	41.990
SXDSW-12128	2 16 31.1	-5 08 43.8	0.805	21.79±0.09	20.58±0.04	34.4±2.0	135±39	0.20	41.944
SXDSW-12844	2 16 43.8	-5 07 54.1	0.804	23.26±0.26	22.18±0.11	7.3±1.5	106±93	0.45	41.184
SXDSW-12890	2 16 57.9	-5 05 39.5	0.801	21.63±0.06	20.38±0.02	42.6±1.6	150±28	0.40	41.964
SXDSW-12994	2 16 30.3	-5 07 59.7	0.806	20.99±0.04	20.48±0.03	17.7±2.0	29±8	0.29	41.625
SXDSW-13080	2 16 55.5	-5 05 18.5	0.804	22.51±0.13	21.75±0.08	8.5±1.5	61±35	0.29	41.303
SXDSW-13103	2 16 23.8	-5 07 42.3	0.811	22.09±0.08	21.81±0.08	2.9±1.5	13±15	0.05	40.936
SXDSW-13564	2 17 08.9	-5 07 15.6	0.803	22.00±0.11	21.44±0.08	9.2±1.9	42±25	0.51	41.269
SXDSW-13607	2 15 43.5	-5 04 36.8	0.799	22.39±0.13	21.58±0.07	10.9±1.6	73±36	0.29	41.403
SXDSW-13984	2 16 40.5	-5 06 51.9	0.804	23.12±0.23	22.32±0.13	5.1±1.5	63±62	0.34	41.067
SXDSW-14140	2 16 50.3	-5 06 39.9	0.804	22.95±0.20	21.91±0.09	9.3±1.5	105±73	0.36	41.322
SXDSW-14401	2 17 00.3	-5 06 22.4	0.811	22.64±0.15	22.21±0.12	3.1±1.6	23±30	0.12	40.934
SXDSW-14539	2 16 19.1	-5 06 14.4	0.810	>23.59	22.43±0.14	6.2±1.6	>132	0.29	41.174
SXDSW-14721	2 15 35.7	-5 06 09.4	0.796	20.92±0.04	20.43±0.03	20.5±1.9	34±8	0.44	41.627
SXDSW-14768	2 16 29.9	-5 06 08.3	0.797	22.02±0.10	21.41±0.08	10.1±1.9	47±26	0.14	41.423
SXDSW-15154	2 16 36.8	-5 05 54.0	0.804	20.26±0.02	19.11±0.01	125.7±1.6	114±6	0.43	42.427
SXDSW-15503	2 16 26.2	-5 05 20.3	0.805	22.22±0.10	21.50±0.06	9.2±1.5	46±23	0.45	41.291
SXDSW-15809	2 16 26.7	-5 05 05.8	0.805	21.25±0.04	20.47±0.03	27.9±1.5	62±11	0.51	41.753
SXDSW-16014	2 17 16.8	-5 04 49.2	0.803
SXDSW-16198	2 16 14.2	-5 00 59.7	0.809	22.47±0.12	21.60±0.07	10.5±1.4	70±34	0.29	41.399
SXDSW-16925	2 16 29.9	-5 03 53.2	0.803	>23.59	22.70±0.24	4.1±2.0	>83	0.41	40.943
SXDSW-17066	2 17 16.3	-4 59 57.4	0.808	20.88±0.03	19.50±0.01	100.1±1.7	174±16	0.29	42.379
SXDSW-17078	2 16 53.2	-4 59 49.2	0.807	>23.48	22.05±0.10	9.8±3.6	>194	0.19	41.404
SXDSW-17122	2 17 21.9	-5 03 49.0	0.804	21.56±0.06	20.58±0.03	30.3±1.6	93±19	0.33	41.843
SXDSW-17661	2 16 04.3	-4 59 04.7	0.804	21.49±0.05	20.98±0.04	12.0±1.4	32±10	0.29	41.453
SXDSW-17713	2 16 11.8	-5 03 10.8	0.805	22.20±0.10	21.62±0.07	7.2±1.5	36±21	0.42	41.190
SXDSW-17857	2 16 28.5	-5 03 02.1	0.803	20.96±0.04	20.18±0.02	38.4±1.7	68±10	0.47	41.900
SXDSW-17950	2 16 44.9	-5 03 02.9	0.802	20.82±0.03	20.17±0.02	33.2±1.5	51±7	0.51	41.823
SXDSW-18358	2 16 47.9	-4 58 05.7	0.802	21.70±0.08	20.84±0.04	22.1±1.8	79±23	0.29	41.716
SXDSW-18531	2 17 12.6	-5 02 16.1	0.807	22.07±0.09	21.45±0.06	9.9±1.5	48±21	0.34	41.356
SXDSW-18825	2 16 15.2	-5 01 56.4	0.806	22.98±0.19	21.58±0.06	14.7±1.5	173±96	0.12	41.606
SXDSW-19290	2 16 40.4	-5 01 32.4	0.803	21.22±0.04	20.59±0.03	20.7±1.5	44±9	0.35	41.669
SXDSW-19359	2 16 04.4	-5 01 21.5	0.800	22.86±0.17	22.28±0.12	4.1±1.4	39±38	0.41	40.942
SXDSW-19641	2 17 19.5	-5 01 05.8	0.807	21.40±0.05	21.05±0.04	8.9±1.6	22±10	0.51	41.257
SXDSW-20331	2 16 37.4	-5 00 23.3	0.802	>23.48	22.25±0.12	7.4±1.5	>138	0.46	41.187
SXDSW-20516	2 17 06.8	-5 00 18.2	0.804	22.30±0.12	21.10±0.05	21.6±1.6	142±52	0.28	41.710
SXDSW-20939	2 16 06.9	-4 59 46.2	0.806	22.23±0.09	21.23±0.05	17.0±1.4	99±33	0.43	41.560
SXDSW-20960	2 17 18.6	-4 59 47.5	0.800	22.23±0.11	21.47±0.07	11.2±1.6	64±30	0.30	41.415
SXDSW-21422	2 15 59.9	-4 59 18.2	0.813	21.48±0.05	21.01±0.04	11.4±1.4	31±10	0.45	41.392
SXDSW-21499	2 16 36.7	-4 59 11.1	0.802	23.19±0.24	22.25±0.12	6.1±1.5	80±73	0.50	41.089
SXDSW-21553	2 16 45.2	-4 59 08.0	0.802	21.77±0.07	21.01±0.04	17.5±1.5	66±18	0.39	41.583
SXDSW-21649	2 16 55.3	-4 59 04.2	0.807	21.45±0.05	20.57±0.03	27.7±1.5	75±15	0.29	41.820
SXDSW-22444	2 16 47.5	-4 58 09.2	0.800	23.48±0.05	22.56±0.07	4.5±0.4	79±22	0.20	41.058
SXDSW-22739	2 16 01.7	-4 57 57.2	0.803	22.91±0.24	22.21±0.15	5.2±1.8	52±59	0.29	41.084
SXDSW-23533	2 16 15.8	-4 57 32.0	0.807	21.53±0.07	20.33±0.03	43.6±2.0	139±31	0.33	42.005
SXDSW-23680	2 16 31.7	-4 57 25.5	0.803	22.25±0.18	20.93±0.06	26.1±2.7	157±87	0.14	41.844
SXDSW-24515	2 16 09.2	-4 56 31.0	0.799	23.02±0.18	21.91±0.08	9.6±1.3	116±70	0.11	41.415
SXDSW-24564	2 15 53.3	-4 56 27.0	0.802	23.58±0.30	21.93±0.08	11.8±1.4	270±236	0.29	41.442
SXDSW-24653	2 16 41.2	-4 56 22.3	0.801	21.99±0.08	21.26±0.05	13.4±1.4	61±21	0.44	41.451
SXDSW-24734	2 17 04.1	-4 56 17.4	0.801	22.56±0.12	21.83±0.07	8.0±1.3	63±33	0.40	41.238
SXDSW-24830	2 16 41.5	-4 56 13.0	0.802	21.04±0.03	20.49±0.02	21.9±1.4	41±7	0.52	41.642
SXDSW-25068	2 17 09.9	-4 55 56.7	0.797	22.37±0.11	21.08±0.04	22.7±1.3	161±51	0.13	41.778
SXDSW-25191	2 16 01.6	-4 55 45.7	0.807	>23.63	22.74±0.19	3.9±1.4	>82	0.46	40.918
SXDSW-25629	2 15 46.3	-4 55 18.7	0.801	22.90±0.16	21.86±0.08	9.9±1.3	110±60	0.21	41.389
SXDSW-25713	2 16 43.3	-4 55 11.9	0.801	23.07±0.20	22.07±0.09	7.7±1.3	97±67	0.41	41.222
SXDSW-25776	2 16 36.0	-4 55 05.6	0.805	23.47±0.29	22.25±0.10	7.4±1.3	137±122	0.24	41.262
SXDSW-26008	2 17 01.3	-4 54 52.6	0.802	23.12±0.21	21.89±0.08	10.2±1.4	132±86	0.29	41.380
SXDSW-26127	2 16 07.7	-4 54 43.1	0.809	23.39±0.26	22.05±0.09	9.6±1.3	179±137	0.29	41.365
SXDSW-26406	2 17 07.4	-4 54 29.0	0.802	20.92±0.03	19.88±0.01	61.9±1.3	113±10	0.44	42.116
SXDSW-26551	2 15 41.8	-4 54 14.8	0.810	23.07±0.20	22.32±0.12	5.0±1.3	60±52	0.19	41.117
SXDSW-26690	2 15 48.4	-4 54 06.1	0.807	22.74±0.14	22.07±0.09	6.0±1.3	54±36	0.41	41.116
SXDSW-26823	2 15 40.4	-4 54 00.4	0.810	21.87±0.06	21.34±0.05	8.7±1.4	32±13	0.47	41.264
SXDSW-26847	2 15 48.4	-4 53 55.9	0.808	20.52±0.02	20.13±0.02	22.5±1.3	25±3	0.47	41.673
SXDSW-26877	2 16 12.2	-4 53 49.8	0.810	22.81±0.16	21.89±0.08	8.0±1.4	70±43	0.23	41.306
SXDSW-26991	2 16 11.3	-4 53 36.9	0.811	23.03±0.19	22.25±0.11	5.6±1.3	66±52	0.13	41.185
SXDSW-27153	2 16 10.2	-4 53 30.5	0.810	20.89±0.03	19.81±0.01	63.3±1.4	100±9	0.51	42.113
SXDSW-27756	2 16 13.1	-4 52 46.9	0.810	21.38±0.04	20.72±0.03	20.3±1.3	52±10	0.43	41.645
SXDSW-28087	2 15 34.3	-4 52 23.4	0.800	21.35±0.07	20.74±0.04	19.1±2.1	48±15	0.48	41.589
SXDSW-28260	2 17 11.3	-4 52 04.7	0.797	22.89±0.17	21.98±0.08	8.0±1.3	86±53	0.19	41.306
SXDSW-28609	2 16 31.7	-4 51 38.8	0.803	>23.40	22.03±0.11	9.6±1.7	>166	0.08	41.432
SXDSW-29408	2 16 39.1	-4 50 38.5	0.808
SXDSW-30365	2 16 59.6	-4 49 30.8	0.797	22.30±0.10	21.69±0.06	7.4±1.3	43±22	0.30	41.231

TABLE 1 — *Continued*

ID (1)	R.A. (J2000) (2)	Dec. (J2000) (3)	z (4)	m_J (5)	m_{NB118} (6)	Line flux (7)	NB EW (8)	[N II]/H α (9)	$\log(L_{\text{H}\alpha})$ (10)
SXDSW-31064	2 17 02.7	-4 48 39.0	0.796	22.04±0.08	21.56±0.06	6.9±1.3	31±16	0.47	41.146
SXDSW-31476	2 15 56.9	-4 48 13.6	0.797	21.19±0.04	20.72±0.03	15.4±1.4	33±8	0.29	41.554
SXDSW-31483	2 17 16.2	-4 48 12.1	0.796	21.88±0.07	21.28±0.05	10.9±1.4	43±15	0.05	41.489
SXDSW-31939	2 15 55.8	-4 47 33.2	0.799	22.43±0.11	21.55±0.06	11.4±1.4	77±33	0.38	41.394
SXDSW-31979	2 16 02.4	-4 47 31.3	0.796	23.39±0.26	21.93±0.08	10.7±1.4	180±138	0.21	41.419
SXDSW-32006	2 15 46.4	-4 47 26.9	0.798	22.79±0.15	22.04±0.09	6.6±1.3	63±41	0.34	41.170
SXDSW-32621	2 16 25.2	-4 46 41.9	0.798	23.33±0.25	22.61±0.16	3.6±1.3	54±63	0.30	40.919
SXDSW-32712	2 15 45.6	-4 46 41.5	0.797	20.94±0.03	20.47±0.02	19.4±1.3	33±6	0.29	41.652
SXDSW-32738	2 16 21.4	-4 46 32.4	0.797	>23.63	22.50±0.14	5.7±1.3	>124	0.06	41.209
SXDSW-32770	2 15 49.1	-4 46 33.0	0.798	22.83±0.15	21.80±0.07	9.8±1.3	95±51	0.29	41.359
SXDSW-32847	2 16 03.7	-4 46 24.4	0.798	22.50±0.12	21.93±0.08	6.0±1.3	43±27	0.37	41.114
SXDSW-33128	2 16 14.7	-4 46 05.3	0.799	21.34±0.04	20.47±0.02	30.6±1.3	76±12	0.04	41.945
SXDSW-33233	2 17 24.2	-4 45 55.0	0.797	22.70±0.13	22.22±0.14	3.8±1.5	31±33	0.23	40.962
SXDSW-33555	2 16 13.9	-4 45 28.0	0.807	23.65±0.02	22.73±0.02	3.9±0.1	82±7	0.34	40.957
SXDSW-33802	2 17 17.6	-4 45 18.3	0.796	21.46±0.05	20.93±0.04	14.2±1.6	39±12	0.29	41.515
SXDSW-33968	2 16 09.8	-4 45 02.6	0.797	22.64±0.16	21.68±0.08	10.5±1.6	83±48	0.24	41.402
SXDSW-34130	2 16 10.7	-4 44 49.7	0.797	22.52±0.16	21.73±0.09	9.3±1.7	71±45	0.16	41.378

NOTE. — (1): ID from the NewH α survey catalog. (2): Units of right ascension are hours, minutes, and seconds. (3): Units of declination are degrees, arcminutes, and arcseconds. (4): IMACS spectroscopic redshift. (5): J -band AB magnitude. The conversion from Vega to AB magnitudes is given by $m(\text{AB}) - m(\text{Vega}) = 0.87$ (Ly et al. 2011a). (6): Narrowband AB magnitude. The conversion from Vega to AB magnitudes is given by $m(\text{AB}) - m(\text{Vega}) = 0.95$ (Ly et al. 2011a). (7): Narrowband flux given in units of 10^{-17} erg s $^{-1}$ cm $^{-2}$. (8): Narrowband EW (rest-frame) given in Å. (9): Estimated [N II]/H α flux ratio, calculated using the narrowband EW (refer to Section 3.2 for further details). Here, [N II] refers to the doublet, 6548 and 6583 Å. (10): Log of observed H α luminosity given in units of erg s $^{-1}$. For both flux and luminosity, the amount of foreground extinction is negligible, so we excluded it in our calculations.

TABLE 2
 NEWH α EMISSION-LINE FLUXES FROM MAGELLAN/IMACS

ID (1)	[OII] ^a (2)	[OIII] λ 4959 (3)	[OIII] λ 5007 (4)	H β (5)	H γ (6)	H δ (7)
SXDSN-12615	4.23±0.19	1.35±0.45	2.61±0.56	1.74±0.28	1.73±0.33	1.90±0.36
SXDSN-14848	6.02±0.21	1.49±0.42	4.83±0.47	0.96±0.79	1.41±0.25	0.09±0.26
SXDSN-17153	3.83±0.12	1.31±0.36	...	3.81±0.24	2.01±0.24	0.63±0.22
SXDSN-17287	1.67±0.12	1.39±0.40	0.30±0.31	0.83±0.45	0.56±0.18	0.08±0.15
SXDSN-18372	3.80±0.15	1.66±0.34	0.23±0.29	3.79±0.59	0.99±0.17	0.23±0.24
SXDSN-18643	2.24±0.09	1.82±0.27	0.35±0.18	2.82±0.33	0.79±0.11	...
SXDSN-18689	1.65±0.11	0.58±0.33	0.61±0.29	2.40±0.47	0.90±0.17	0.21±0.18
SXDSN-18825	4.46±0.11	1.03±0.30	2.90±0.40	2.09±0.20	1.26±0.18	1.10±0.19
SXDSN-19419
SXDSN-19725	15.14±0.27	1.50±0.29
SXDSN-19822	41.68±0.45	50.93±1.00	122.51±1.13	115.20±0.97	46.62±0.72	17.02±0.65
SXDSN-20554	5.36±0.17	9.64±0.72	3.53±0.45	4.82±0.47	0.67±0.28	0.40±0.17
SXDSN-20774	1.76±0.27	2.31±0.18
SXDSN-20874	2.63±0.25
SXDSN-22048	7.27±0.09	1.31±0.21	2.84±0.21	1.98±0.31	1.10±0.11	0.48±0.13
SXDSN-22485	7.07±0.17	1.07±0.27	2.42±0.24	3.20±0.29	1.51±0.27	0.73±0.16
SXDSN-23784	12.38±0.23	1.60±0.52	5.17±0.36	5.89±0.32	2.81±0.34	1.31±0.21
SXDSN-23860	4.38±0.18	0.80±0.28	2.15±0.33	3.20±0.37	1.78±0.37	0.58±0.17
SXDSN-24371	8.06±0.20	...	4.58±0.46	8.26±0.53	1.21±0.29	1.09±0.20
SXDSN-24458	9.45±0.19	5.42±0.51	4.06±0.44	5.45±0.36	2.18±0.27	0.75±0.17
SXDSN-24652	3.59±0.14	2.63±0.25	5.93±0.37	1.37±0.32	0.75±0.27	0.07±0.13
SXDSN-24723	2.92±0.17	...	0.82±0.34	0.82±0.55	0.68±0.22	0.73±0.18
SXDSN-24979	3.21±0.11	2.60±0.31	1.33±0.27	...	0.78±0.15	...
SXDSN-25202	2.82±0.16	0.89±0.28	1.02±0.34	2.06±0.36	0.75±0.35	0.58±0.16
SXDSN-26559	4.53±0.13	0.55±0.19	1.50±0.29	3.30±0.47	0.51±0.27	0.66±0.13
SXDSN-26798	4.58±0.11	1.14±0.29	4.04±0.24	1.81±0.20	0.72±0.22	0.61±0.15
SXDSN-26828	4.88±0.09	0.23±0.26	1.58±0.18	1.35±0.19	...	0.50±0.11
SXDSN-27037	2.18±0.08	...	0.55±0.18	2.18±0.19	0.76±0.18	0.44±0.12
SXDSN-28032	10.27±0.10	2.64±0.23	7.74±0.25	3.00±0.34	1.76±0.12	0.94±0.15
SXDSN-28267	13.14±0.15	6.80±0.37	14.15±0.36	5.00±0.50	2.22±0.19	1.71±0.17
SXDSN-29887	1.63±0.26	0.62±0.33	...	0.52±0.30	...	0.09±0.20
SXDSN-30551	11.72±0.12	1.70±0.37	...	4.76±0.47	2.28±0.20	1.35±0.16
SXDSN-31207	2.54±0.09	0.43±0.21	1.04±0.25	3.31±0.24	1.35±0.17	0.51±0.09
SXDSN-31304	6.11±0.32	...	2.71±0.64	5.85±0.70	2.09±0.43	2.74±0.39
SXDSN-31331	3.75±0.10	...	2.24±0.33	5.15±0.32	2.15±0.23	2.90±0.14
SXDSN-31929	0.95±0.19	28.46±0.70	26.30±0.64	2.87±0.69
SXDSN-32915	4.07±0.09	0.61±0.18	2.10±0.18	2.20±0.25	1.53±0.20	0.49±0.11
SXDSN-33371	2.42±0.15	1.14±0.34	2.31±0.34	1.08±0.51	1.13±0.20	0.34±0.19
SXDSN-34057	1.09±0.13	...	0.67±0.24	0.42±0.18	0.42±0.29	0.17±0.16
SXDSN-34591	3.33±0.10	1.23±0.34	0.84±0.28	1.66±0.24	0.55±0.17	0.47±0.10
SXDSN-34643	10.62±0.14	2.41±0.21	5.19±0.27	3.79±0.57	1.15±0.25	0.78±0.12
SXDSN-34925	5.32±0.09	0.92±0.31	3.07±0.24	1.69±0.33	0.88±0.14	0.78±0.12
SXDSN-35304	4.61±0.12	1.42±0.33	1.99±0.20	...	0.82±0.12	0.33±0.18
SXDSN-35455	8.14±0.21	1.28±0.37	3.75±0.35	4.09±0.36	1.75±0.30	0.67±0.22
SXDSN-35945	3.92±0.14	4.04±0.40	11.65±0.29	8.60±0.36	5.08±0.37	2.40±0.25
SXDSN-36476	2.96±0.11	9.35±0.54	1.61±0.19	0.89±0.14	0.49±0.19	0.30±0.11
SXDSN-37348	4.37±0.15	1.33±0.28	0.08±0.22	1.73±0.25	0.97±0.26	0.58±0.16
SXDSN-37430	3.68±0.16	0.13±0.30	0.73±0.35	2.38±0.55	1.04±0.19	0.13±0.23
SXDSN-38796	6.57±0.24	2.22±0.66	2.00±0.44	11.26±0.43	4.09±0.38	2.09±0.30
SXDSN-39242	4.25±0.13	3.67±0.42	10.34±0.30	2.86±0.56	1.62±0.19	1.31±0.20
SXDSN-39615	4.46±0.15	2.21±0.49	1.93±0.26	1.22±0.21	0.85±0.26	0.54±0.19
SXDSN-39807	2.26±0.14	1.66±0.65	1.94±0.24	1.07±0.20	0.40±0.24	0.51±0.16
SXDSN-41162	7.89±0.19	...	6.45±0.33	2.24±0.65	1.47±0.31	0.94±0.23
SXDSN-41683	1.12±0.13	6.73±0.60	0.02±0.23	0.55±0.16
SXDSN-41684	1.27±0.14	...	2.54±0.49	...	0.99±0.35	0.64±0.22
SXDSS-8347	5.63±0.11	1.00±0.42	2.73±0.22	1.19±0.30	0.89±0.15	0.31±0.10
SXDSS-12333	3.67±0.14	0.64±0.27	1.85±0.19	1.01±0.42	0.69±0.20	0.29±0.16
SXDSS-12862	2.01±0.14	0.84±0.32	0.70±0.22	2.31±0.46	0.55±0.16	0.47±0.23
SXDSS-14115	5.57±0.12	0.66±0.31	1.43±0.16	2.19±0.44	1.21±0.16	0.45±0.15
SXDSS-14438	3.02±0.13	1.13±0.19	1.81±0.20	0.91±0.18	0.82±0.34	0.25±0.12
SXDSS-14722	8.27±0.16	1.41±0.17	4.98±0.25	2.85±0.35	1.04±0.23	0.73±0.14
SXDSS-15629	3.47±0.29	0.96±0.18	1.21±0.23	1.35±0.19	0.38±0.14	0.37±0.10
SXDSS-15945	7.61±0.12	1.11±0.21	5.24±0.27	3.50±0.21	1.39±0.16	0.75±0.10
SXDSS-16362	7.80±0.16	5.30±0.24	15.00±0.44	3.51±0.21	1.39±0.17	1.61±0.27
SXDSS-16423	3.54±0.14	1.28±0.26	...	1.68±0.44	1.38±0.24	0.41±0.17
SXDSS-16739	2.96±0.16	...	0.02±0.37	3.44±0.39	1.51±0.31	0.72±0.17
SXDSS-16866	3.77±0.23	3.83±0.59	0.18±0.31
SXDSS-17510	5.87±0.19	0.43±0.32	3.88±0.32	1.91±0.40	0.88±0.37	0.86±0.22
SXDSS-17705	5.53±0.12	1.77±0.32	5.17±0.19	1.92±0.44	1.27±0.15	0.65±0.15
SXDSS-17733	9.10±0.13	1.55±0.24	4.69±0.21	4.13±0.43	2.24±0.21	0.69±0.16
SXDSS-17787	2.55±0.17	0.90±0.19	0.14±0.27	0.34±0.24
SXDSS-17924	4.45±0.13	0.92±0.19	2.89±0.20	1.81±0.30	1.06±0.26	0.26±0.15
SXDSS-17941	3.73±0.12	1.30±0.32	2.21±0.28	1.18±0.14	0.40±0.24	0.05±0.15
SXDSS-17958	8.59±0.13	3.23±0.19	8.02±0.22	3.29±0.17	1.18±0.31	0.78±0.12

TABLE 2 — *Continued*

ID (1)	[OII] ^a (2)	[OIII] λ 4959 (3)	[OIII] λ 5007 (4)	H β (5)	H γ (6)	H δ (7)
SXDSS-18093	1.23±0.12	0.47±0.26	0.68±0.17	...	0.20±0.20	...
SXDSS-18211	1.98±0.17	...	0.04±0.28	1.88±0.30	0.96±0.36	0.88±0.20
SXDSS-18370	2.95±0.15	1.80±0.32	5.33±0.35	1.41±0.19	0.62±0.23	0.67±0.21
SXDSS-18554	6.67±0.14	2.37±0.19	5.27±0.22	2.38±0.20	1.06±0.27	0.61±0.12
SXDSS-18604	3.46±0.13	1.02±0.32	2.59±0.21	0.75±0.51	0.45±0.20	0.14±0.17
SXDSS-18617	4.61±0.12	2.13±0.32	5.68±0.30	1.81±0.15	0.52±0.23	0.72±0.17
SXDSS-18709	0.03±0.14	0.27±0.24	1.22±0.23	0.19±0.18
SXDSS-19166	2.44±0.16	0.59±0.35	2.29±0.27	2.11±0.54	1.34±0.26	0.42±0.21
SXDSS-19596	1.28±0.17	0.50±0.39	0.93±0.39	1.32±0.25	0.32±0.30	0.20±0.27
SXDSS-20389	1.51±0.14	2.14±0.23	4.60±0.25	1.07±0.47	0.10±0.37	0.12±0.19
SXDSS-20452	3.76±0.13	0.19±0.17	0.56±0.17	3.23±0.20	0.97±0.26	0.68±0.12
SXDSS-20675	2.91±0.15	...	1.41±0.29	3.48±0.48	0.87±0.17	0.53±0.19
SXDSS-21192	4.15±0.15	0.47±0.29	3.33±0.25	1.24±0.41	0.61±0.15	0.23±0.19
SXDSS-21634	9.80±0.15	2.79±0.19	7.29±0.26	2.66±0.25	1.76±0.25	0.79±0.13
SXDSS-21685	1.49±0.18	2.74±0.53	0.52±0.43	0.81±0.24	1.20±0.28	0.58±0.24
SXDSS-21861	10.59±0.16	3.69±0.22	9.74±0.24	4.88±0.29	2.26±0.26	0.80±0.17
SXDSS-21905	1.91±0.15	0.38±0.30	1.87±0.27	1.96±0.34	2.14±0.29	0.91±0.19
SXDSS-22205	6.89±0.13	1.66±0.18	4.31±0.19	3.11±0.33	0.95±0.25	0.43±0.14
SXDSS-22262	0.61±0.11	0.15±0.20	0.29±0.18	1.46±0.36	0.48±0.25	0.05±0.15
SXDSS-22277	3.37±0.14	0.75±0.19	1.67±0.18	1.17±0.25	0.99±0.23	0.25±0.15
SXDSS-22355	1.82±0.20	0.07±0.38	1.56±0.33	1.10±0.35	0.45±0.35	0.40±0.24
SXDSS-22389	1.18±0.12	0.04±0.19	0.35±0.15	0.89±0.16	0.47±0.15	0.25±0.11
SXDSS-22452	8.29±0.24	197.49±0.92	377.45±1.00	25.71±0.62
SXDSS-22538	5.13±0.13	0.34±0.17	1.05±0.17	3.39±0.19	1.45±0.26	0.72±0.12
SXDSS-22557	2.25±0.12	0.92±0.31	1.69±0.19	1.01±0.16	0.03±0.18	0.25±0.11
SXDSS-22717	1.13±0.13	0.26±0.21	0.16±0.19	1.21±0.34	0.34±0.26	0.25±0.16
SXDSS-22728	10.43±0.16	2.07±0.25	4.92±0.24	5.16±0.30	2.57±0.26	1.22±0.17
SXDSS-22887	4.13±0.11	...	2.30±0.21	0.67±0.38	0.60±0.15	0.22±0.11
SXDSS-22991	3.73±0.17	0.73±0.24	0.83±0.23	1.92±0.39	1.31±0.32	0.81±0.19
SXDSS-23082
SXDSS-23167	4.13±0.13	1.54±0.16	4.69±0.18	1.94±0.17	0.54±0.26	0.29±0.11
SXDSS-23384	5.93±0.20	...	3.43±0.36	...	1.15±0.33	0.71±0.30
SXDSS-23393	22.60±0.19	3.74±0.32	9.47±0.25	11.26±0.53	4.26±0.31	2.32±0.19
SXDSS-23571	2.23±0.14	0.97±0.29	0.30±0.15	0.45±0.16
SXDSS-23647	15.03±0.17	3.12±0.25	7.41±0.24	6.70±0.44	3.13±0.30	0.95±0.19
SXDSS-23665	9.68±0.17	0.63±0.48	0.40±0.26	1.31±0.30	0.64±0.19	0.37±0.13
SXDSS-23667	4.79±0.13	0.96±0.27	1.97±0.21	3.16±0.42	1.00±0.14	0.44±0.18
SXDSS-23807	2.53±0.12	4.44±0.17	14.15±0.20	0.60±0.33	1.26±0.24	0.49±0.14
SXDSS-24027	10.13±0.14	2.31±0.17	8.20±0.21	3.40±0.20	1.58±0.27	0.92±0.12
SXDSS-24055	7.40±0.17	1.74±0.27	4.17±0.30	...	0.89±0.16	0.65±0.21
SXDSS-24177	...	6.63±0.57	20.82±0.55	16.94±0.65	0.52±0.38	...
SXDSS-24469	3.56±0.16	0.89±0.37	1.38±0.21	1.62±0.52	0.76±0.20	0.22±0.19
SXDSS-24527	4.61±0.19	0.45±0.56	0.50±0.36	5.80±1.18	0.15±0.37	0.45±0.18
SXDSS-24609	10.71±0.18	2.09±0.37	3.27±0.26	6.95±0.55	2.82±0.21	1.77±0.23
SXDSS-26461
SXDSS-26565	6.65±0.16	2.25±0.35	4.91±0.26	1.73±0.46	1.13±0.18	0.78±0.20
SXDSS-26597	4.31±0.14	0.70±0.17	1.26±0.19	1.89±0.24	0.65±0.25	0.22±0.12
SXDSS-26724	3.08±0.11	1.26±0.26	2.44±0.16	1.57±0.35	0.94±0.13	0.47±0.12
SXDSS-27335	4.45±0.14	2.54±0.37	5.30±0.24	2.53±0.56	0.77±0.20	0.31±0.18
SXDSS-27364	2.36±0.11	0.89±0.16	1.89±0.16	0.93±0.33	0.64±0.23	0.31±0.13
SXDSS-27425	4.32±0.14	2.70±0.29	4.00±0.22	0.99±0.44	...	0.45±0.17
SXDSS-27514	0.34±0.14	0.14±0.28	...
SXDSS-27584	0.50±0.10	0.25±0.25	...	0.74±0.39	0.36±0.16	0.06±0.12
SXDSS-27730	1.86±0.13	0.62±0.29	...	1.96±0.31	1.13±0.34	0.27±0.19
SXDSS-27769	12.97±0.14	2.99±0.17	...	5.43±0.21	2.19±0.24	1.11±0.11
SXDSS-27865	2.43±0.19	5.67±0.50	...	5.74±0.67	0.80±0.25	0.13±0.28
SXDSS-27927	...	2.88±0.30	5.42±0.26	3.24±0.40	1.04±0.14	0.26±0.19
SXDSS-28010	3.40±0.12	...	2.99±0.21	0.39±0.35	0.60±0.12	0.22±0.16
SXDSS-28369	1.92±0.14	0.19±0.27	0.66±0.19	1.57±0.45	0.83±0.23	0.41±0.18
SXDSS-28490	...	4.64±0.69	4.88±0.59	4.11±0.81
SXDSS-28526	7.34±0.15	1.31±0.26	3.00±0.21	3.17±0.37	1.24±0.13	0.73±0.18
SXDSS-28810	1.87±0.14	0.79±0.30	0.85±0.23	1.24±0.42	0.64±0.16	0.62±0.20
SXDSS-28845	2.87±0.17	0.66±0.33	0.63±0.24	3.17±0.55	1.50±0.28	0.95±0.22
SXDSS-28926	4.50±0.13	0.43±0.29	2.51±0.21	1.05±0.44	0.67±0.19	0.37±0.16
SXDSS-29206	5.18±0.14	1.83±0.27	4.38±0.19	1.97±0.17	0.86±0.23	0.41±0.16
SXDSS-29259	1.78±0.11	0.51±0.17	1.18±0.19	1.01±0.25	0.09±0.28	0.19±0.10
SXDSS-29322	2.29±0.15	0.13±0.26	0.45±0.27	1.50±0.28	1.59±0.31	0.74±0.16
SXDSS-29327	4.46±0.16	0.58±0.29	1.18±0.23	3.45±0.23	1.44±0.26	0.39±0.18
SXDSS-29607	1.11±0.18	...	0.08±0.37	0.37±0.21
SXDSS-29646	2.80±0.16	0.01±0.37	0.22±0.31	0.78±0.52	...	3.94±0.24
SXDSS-29754	2.30±0.14	0.13±0.29	0.13±0.17	2.43±0.46	0.41±0.19	0.51±0.17
SXDSS-29859	5.97±0.12	2.77±0.18	8.22±0.20	2.56±0.29	1.20±0.25	0.44±0.13
SXDSS-29972	3.01±0.13	0.57±0.32	1.67±0.21	0.62±0.44	0.55±0.15	0.27±0.17
SXDSS-30051	3.88±0.15	1.21±0.27	1.13±0.20	3.17±0.48	1.22±0.26	0.83±0.18
SXDSS-30124	5.39±0.14	1.41±0.29	2.20±0.37	0.91±0.15	0.79±0.15	0.25±0.16
SXDSS-30142	4.38±0.15	0.34±0.33	1.64±0.19	3.08±0.46	1.64±0.19	0.75±0.17

TABLE 2 — *Continued*

ID (1)	[OII] ^a (2)	[OIII] λ 4959 (3)	[OIII] λ 5007 (4)	H β (5)	H γ (6)	H δ (7)
SXDSS-30295	12.44±0.14	6.09±0.25	15.80±0.32	5.17±0.15	2.09±0.20	0.97±0.19
SXDSS-31496	4.93±0.15	0.87±0.20	1.78±0.22	2.72±0.25	1.28±0.30	0.40±0.15
SXDSS-32097	10.40±0.16	1.43±0.22	4.29±0.20	5.72±0.23	2.38±0.20	1.21±0.15
SXDSS-32132	3.46±0.13	2.55±0.50	1.30±0.22	1.19±0.16	0.73±0.19	0.44±0.12
SXDSS-32277	11.74±0.18	2.18±0.31	1.18±0.19	3.48±0.50	1.98±0.26	0.87±0.18
SXDSS-32372	0.80±0.12	0.01±0.16	0.35±0.14	...	0.19±0.20	0.27±0.13
SXDSS-33021	4.86±0.14	...	2.14±0.20	1.79±0.43	0.77±0.21	0.47±0.17
SXDSS-33298	11.73±0.15	1.75±0.18	5.28±0.17	6.72±0.18	2.80±0.15	1.25±0.12
SXDSS-33303	5.39±0.21	...	7.19±0.49	1.16±0.84	1.31±0.23	...
SXDSS-33787	3.56±0.14	1.27±0.24	4.56±0.17	1.56±0.15	0.70±0.16	0.19±0.12
SXDSS-35437	4.72±0.14	0.48±0.30	0.65±0.18	4.69±0.43	1.44±0.16	0.40±0.17
SXDSS-35468	2.17±0.15	0.41±0.34	1.12±0.22	...	0.67±0.18	0.42±0.20
SXDSS-35702	...	3.00±0.16	8.03±0.18	3.94±0.27	1.68±0.23	0.94±0.12
SXDSS-35926	10.55±0.22	2.59±0.50	6.57±0.50	0.22±0.87	1.44±0.26	1.99±0.35
SXDSS-36006	6.24±0.15	0.97±0.30	2.06±0.22	3.03±0.48	1.28±0.17	0.52±0.19
SXDSS-36019	17.27±0.16	...	10.74±0.28	7.56±0.43	2.81±0.15	1.76±0.19
SXDSS-36053	3.10±0.14	...	1.05±0.25	1.53±0.42	0.60±0.15	0.20±0.16
SXDSS-36054	0.24±0.13	0.12±0.28	0.06±0.17	0.16±0.12
SXDSS-36609	16.86±0.20	5.15±0.38	8.88±0.28	10.92±0.52	4.47±0.21	2.94±0.22
SXDSS-36655	1.81±0.12	3.41±0.50	1.35±0.20	1.23±0.15	0.66±0.18	0.28±0.12
SXDSS-36770	4.67±0.13	0.68±0.24	1.18±0.15	2.81±0.15	1.53±0.17	0.54±0.12
SXDSS-36865	6.65±0.15	0.25±0.22	3.67±0.22	4.02±0.42	1.58±0.30	0.59±0.18
SXDSS-36954	3.83±0.11	0.76±0.15	0.89±0.13	0.57±0.16	0.77±0.16	0.55±0.10
SXDSS-36995	0.80±0.16	2.55±0.40	0.28±0.27	1.19±0.60	0.35±0.22	...
SXDSS-37057	4.97±0.13	1.18±0.19	2.66±0.17	2.09±0.18	1.16±0.18	0.56±0.13
SXDSS-37189	3.45±0.12	4.12±0.21	7.66±0.26	2.55±0.35	1.00±0.12	0.13±0.17
SXDSS-37234	2.64±0.12	0.89±0.19	1.81±0.17	0.51±0.16	0.36±0.17	0.29±0.12
SXDSS-37285	8.56±0.16	2.01±0.29	6.10±0.26	6.07±0.49	0.75±0.28	0.56±0.19
SXDSS-37540	6.07±0.16	0.21±0.32	1.97±0.21	2.75±0.20	1.42±0.22	0.79±0.16
SXDSS-37564	6.06±0.15	0.54±0.30	3.56±0.27	2.14±0.42	0.99±0.16	0.68±0.18
SXDSS-37774	3.99±0.13	0.63±0.20	1.60±0.15	2.50±0.15	1.02±0.15	0.47±0.11
SXDSS-37799	0.52±0.10	1.65±0.32	...	0.34±0.12	...	0.10±0.09
SXDSS-37947	1.22±0.12	0.64±0.22	0.51±0.19	2.65±0.43	0.88±0.29	0.25±0.16
SXDSS-37948	1.99±0.13	1.82±0.50	1.01±0.33	0.69±0.16	0.47±0.19	0.45±0.13
SXDSS-38003	3.00±0.11	1.13±0.20	3.40±0.19	1.06±0.30	0.55±0.10	0.34±0.14
SXDSS-38307	1.47±0.13	1.28±0.35	1.49±0.20	1.69±0.46	0.44±0.16	0.49±0.17
SXDSS-38485	0.71±0.11	3.40±0.47	2.21±0.26	0.32±0.12
SXDSS-38541	3.03±0.15	0.81±0.22	0.93±0.20	1.99±0.34	0.88±0.28	0.39±0.17
SXDSS-38602	2.72±0.21	0.17±0.43	0.05±0.31	1.00±0.28	0.16±0.30	...
SXDSS-38698	7.19±0.14	0.42±0.22	1.41±0.18	7.10±0.24	3.01±0.20	1.45±0.13
SXDSS-38754	4.13±0.12	1.83±0.19	6.04±0.17	1.98±0.14	0.69±0.14	0.27±0.11
SXDSS-38784	1.26±0.13	2.46±0.42	0.61±0.21	1.24±0.17	0.64±0.19	0.23±0.13
SXDSS-39016	8.29±0.15	1.05±0.24	2.84±0.19	4.13±0.19	1.58±0.18	0.92±0.14
SXDSS-39160	0.81±0.11	1.98±0.22	4.51±0.21	2.55±0.39	0.34±0.28	0.22±0.16
SXDSS-39161	1.23±0.13	3.05±0.33	0.41±0.17	1.15±0.44	0.38±0.18	0.22±0.15
SXDSS-39226	1.90±0.12	0.41±0.27	1.10±0.16	2.33±0.37	0.49±0.15	0.14±0.14
SXDSS-39288	25.93±0.19	7.35±0.26	21.72±0.29	10.53±0.41	4.29±0.15	1.59±0.20
SXDSS-39308	5.50±0.15	2.26±0.46	4.86±0.29	2.13±0.19	0.63±0.22	0.28±0.16
SXDSS-39501	1.02±0.13	0.62±0.24	0.53±0.20	2.65±0.45	0.51±0.30	0.37±0.18
SXDSS-39548	7.50±0.13	2.98±0.37	6.20±0.18	2.52±0.14	0.83±0.17	0.59±0.11
SXDSS-39672	1.27±0.15	0.59±0.23	0.29±0.19	1.06±0.32	...	0.62±0.18
SXDSS-40071	3.16±0.18	0.27±0.38	1.00±0.28	2.74±0.60	1.64±0.27	0.65±0.25
SXDSS-40327	1.24±0.14	2.20±0.42	0.47±0.21	1.64±0.20	0.57±0.22	0.49±0.15
SXDSS-40667	3.07±0.11	2.83±0.35	3.86±0.25	3.20±0.23	1.00±0.16	0.65±0.10
SXDSS-41193	13.07±0.15	4.17±0.18	12.04±0.20	4.57±0.18	1.76±0.17	0.98±0.12
SXDSS-41546	1.58±0.15	1.00±0.30	0.31±0.22	2.03±0.24	0.50±0.21	0.41±0.16
SXDSS-8210	5.75±0.13	...	0.84±0.19	1.49±0.22	3.01±0.28	0.53±0.12
SXDSS-9136	4.44±0.13	1.51±0.39	2.59±0.25	1.35±0.28	0.86±0.18	0.48±0.12
SXDSS-10296	9.57±0.10	3.71±0.17	9.08±0.16	4.33±0.15	1.50±0.14	0.79±0.09
SXDSS-11479	5.29±0.14	2.75±0.28	5.22±0.27	2.99±0.44	1.16±0.16	0.48±0.19
SXDSS-11971	18.12±0.24	3.85±0.40	7.40±0.47	5.54±0.79	2.90±0.23	1.26±0.33
SXDSS-12128	22.14±0.14	6.96±0.28	17.16±0.25	8.19±0.34	3.87±0.15	2.00±0.12
SXDSS-12844	3.88±0.14	...	0.17±0.18	...	0.38±0.14	0.01±0.17
SXDSS-12890	10.45±0.23	2.19±0.40	4.91±0.38	5.88±0.72	2.05±0.52	0.98±0.29
SXDSS-12994	0.88±0.13	23.07±0.42	...	54.16±0.59	2.81±0.22	1.69±0.22
SXDSS-13080	6.00±0.21	0.59±0.36	1.95±0.44	...	0.89±0.22	...
SXDSS-13103	2.04±0.10	1.01±0.17	3.03±0.17	0.64±0.14	0.25±0.19	...
SXDSS-13564	2.75±0.27	...	2.37±0.56	5.38±1.27	0.90±0.40	0.51±0.46
SXDSS-13607	0.94±0.18	0.61±0.26	0.22±0.34	...
SXDSS-13984	5.93±0.13	0.08±0.21	2.40±0.22	2.55±0.38	0.90±0.13	0.25±0.16
SXDSS-14140	3.19±0.12	0.67±0.19	1.98±0.20	0.29±0.34	0.42±0.12	0.42±0.16
SXDSS-14401	5.68±0.13	0.42±0.21	2.14±0.18	1.22±0.16	0.75±0.21	0.10±0.14
SXDSS-14539	1.49±0.11	0.67±0.15	1.56±0.24	0.41±0.13
SXDSS-14721	4.49±0.12	0.64±0.27	1.32±0.26	2.52±0.16	0.60±0.20	0.68±0.18
SXDSS-14768	17.77±0.14	12.96±0.26	34.11±0.35	9.61±0.16	4.06±0.15	3.73±0.16
SXDSS-15154	24.24±0.18	4.86±0.28	12.26±0.28	16.12±0.46	6.79±0.18	3.24±0.20

TABLE 2 — *Continued*

ID (1)	[OII] ^a (2)	[OIII] λ 4959 (3)	[OIII] λ 5007 (4)	H β (5)	H γ (6)	H δ (7)
SXDSW-15503	5.00±0.14	0.75±0.22	2.43±0.20	3.49±0.35	1.23±0.14	0.72±0.13
SXDSW-15809	2.95±0.13	1.62±0.36	1.99±0.27	4.41±0.44	0.72±0.18	0.32±0.17
SXDSW-16014	1.47±0.11	1.31±0.28	...	2.29±0.36	0.41±0.12	0.08±0.16
SXDSW-16198	4.47±0.23	0.13±0.41	1.14±0.60	0.52±0.21
SXDSW-16925	5.46±0.12	1.33±0.29	4.73±0.19	0.51±0.39	0.85±0.15	0.55±0.14
SXDSW-17066	45.15±0.29	13.40±0.38	43.10±0.57	24.12±0.53	8.72±0.43	5.63±0.23
SXDSW-17078	6.78±0.21	1.88±0.35	3.00±0.50	1.91±0.46	0.93±0.36	0.62±0.18
SXDSW-17122	19.90±0.25	8.32±0.56	16.34±0.55	11.01±0.89	3.42±0.27	2.27±0.36
SXDSW-17661	0.91±0.17	1.48±0.45	0.50±0.30	1.82±0.67	0.19±0.17	...
SXDSW-17713	1.19±0.08	...	0.36±0.13	25.06±0.28	...	1.37±0.08
SXDSW-17857	4.61±0.12	0.20±0.27	1.37±0.17	3.13±0.37	1.67±0.14	1.12±0.16
SXDSW-17950	2.52±0.12	0.48±0.20	0.82±0.16	3.85±0.38	0.67±0.23	0.71±0.15
SXDSW-18358	4.50±0.23	0.67±0.41	1.53±0.35	0.89±2.91	0.46±0.52	0.39±0.31
SXDSW-18531	6.63±0.13	7.88±0.40	11.36±0.29	6.08±0.25	4.14±0.19	0.68±0.12
SXDSW-18825	1.85±0.07	5.06±0.27	8.78±0.20	1.93±0.16	0.88±0.10	0.56±0.07
SXDSW-19290	3.00±0.13	0.33±0.31	0.46±0.18	1.53±0.46	1.64±0.21	0.78±0.17
SXDSW-19359	1.46±0.13	0.68±0.35	0.73±0.23	0.86±0.21	0.17±0.20	0.10±0.15
SXDSW-19641	4.53±0.15	1.24±0.31	3.03±0.32	6.21±0.35	3.53±0.27	0.85±0.16
SXDSW-20331	5.73±0.14	1.76±0.23	3.61±0.21	...	0.51±0.28	0.50±0.17
SXDSW-20516	8.53±0.17	5.00±0.34	15.07±0.41	6.60±0.56	2.71±0.18	1.55±0.24
SXDSW-20939	5.37±0.12	0.54±0.34	2.51±0.23	3.42±0.34	0.32±0.15	0.39±0.13
SXDSW-20960	11.95±0.13	2.61±0.18	5.44±0.16	4.73±0.19	3.40±0.19	1.21±0.12
SXDSW-21422	1.90±0.10	2.41±0.27	1.52±0.18	1.71±0.18	0.88±0.20	0.21±0.14
SXDSW-21499	2.36±0.13	1.95±0.27	3.15±0.20	4.15±0.47	1.42±0.24	0.58±0.17
SXDSW-21553	4.27±0.16	0.92±0.27	1.49±0.22	2.03±0.42	1.40±0.30	0.76±0.20
SXDSW-21649	5.12±0.19	0.75±0.43	1.12±0.51	3.31±0.45	1.00±0.33	0.98±0.20
SXDSW-22444	5.42±0.15	1.68±0.24	4.29±0.26	2.02±0.36	0.35±0.27	0.21±0.16
SXDSW-22739	1.53±0.12	0.29±0.28	0.37±0.16	1.89±0.43	...	0.03±0.14
SXDSW-23533	11.65±0.12	1.46±0.20	3.87±0.21	4.43±0.20	1.59±0.14	0.80±0.09
SXDSW-23680	10.81±0.12	6.64±0.26	17.31±0.22	5.10±0.34	2.26±0.14	1.44±0.13
SXDSW-24515	9.49±0.11	1.68±0.34	11.38±0.21	3.37±0.12	1.49±0.13	0.54±0.08
SXDSW-24564	3.13±0.14	1.53±0.33	4.74±0.29	0.61±0.59	0.45±0.30	0.22±0.19
SXDSW-24653	5.21±0.12	0.84±0.15	1.84±0.13	3.09±0.24	1.26±0.19	0.63±0.12
SXDSW-24734	...	1.47±0.16	3.21±0.16	2.52±0.20	1.14±0.20	0.33±0.12
SXDSW-24830	0.87±0.15	...	1.19±0.23	4.21±0.50	0.39±0.25	1.00±0.22
SXDSW-25068	21.67±0.15	13.40±0.32	26.95±0.36	8.63±0.16	4.00±0.15	2.27±0.14
SXDSW-25191	1.59±0.10	1.02±0.36	1.37±0.21	...	0.02±0.14	0.20±0.11
SXDSW-25629	5.69±0.11	1.35±0.16	3.40±0.15	1.95±0.20	0.99±0.18	0.55±0.11
SXDSW-25713	5.79±0.19	0.50±0.21	2.84±0.21	0.15±0.34	0.93±0.30	0.54±0.19
SXDSW-25776	4.42±0.23	6.91±0.68	6.26±0.50	2.64±0.66	1.43±0.30	0.60±0.23
SXDSW-26008	...	2.03±0.32	5.44±0.34	...	0.83±0.35	0.41±0.21
SXDSW-26127	...	1.99±0.27	3.97±0.30	2.55±0.24	...	0.81±0.16
SXDSW-26406	15.87±0.14	2.47±0.22	6.18±0.18	9.74±0.37	3.20±0.22	1.82±0.14
SXDSW-26551	6.14±0.10	2.15±0.14	4.83±0.15	2.21±0.13	0.94±0.19	0.60±0.10
SXDSW-26690	2.81±0.12	1.36±0.24	1.30±0.25	1.59±0.25	0.29±0.18	0.34±0.12
SXDSW-26823	6.37±0.15	0.45±0.24	2.18±0.25	4.42±0.23	0.27±0.31	0.95±0.16
SXDSW-26847	2.56±0.16	...	1.61±0.43	2.34±0.40	...	0.69±0.18
SXDSW-26877	7.17±0.19	1.55±0.37	3.70±0.37	2.39±0.28	1.46±0.37	0.22±0.21
SXDSW-26991	4.66±0.15	1.12±0.31	1.85±0.28	1.07±0.22	...	0.71±0.17
SXDSW-27153	2.51±0.15	...	3.10±0.29	6.02±0.33	4.21±0.34	2.03±0.19
SXDSW-27756	3.27±0.12	0.74±0.20	1.59±0.19	2.07±0.19	1.36±0.25	0.63±0.14
SXDSW-28087	3.28±0.15	1.29±0.27	2.06±0.25	3.13±0.33	...	0.85±0.17
SXDSW-28260	9.10±0.12	4.08±0.25	8.15±0.31	3.52±0.14	1.40±0.14	0.75±0.14
SXDSW-28609	6.61±0.12	2.50±0.29	7.20±0.20	2.03±0.36	0.72±0.13	0.65±0.15
SXDSW-29408	1.37±0.13	...	0.71±0.26	1.08±0.25	0.50±0.20	0.11±0.12
SXDSW-30365	7.83±0.14	2.03±0.25	3.61±0.34	3.10±0.17	1.47±0.17	1.06±0.19
SXDSW-31064	3.38±0.11	1.14±0.20	1.53±0.23	2.66±0.15	0.93±0.17	0.26±0.19
SXDSW-31476	2.12±0.16	...	0.38±0.59	2.92±0.27	1.18±0.24	0.47±0.20
SXDSW-31483	2.21±0.11	1.50±0.17	4.59±0.27	0.83±0.12
SXDSW-31939	3.23±0.10	1.67±0.36	0.70±0.17	1.30±0.13	0.84±0.15	0.49±0.11
SXDSW-31979	5.91±0.19	5.91±0.45	10.20±0.65	3.71±0.28	2.93±0.27	1.13±0.33
SXDSW-32006	4.62±0.19	0.94±0.66	1.68±0.44	1.90±0.28	1.81±0.30	0.50±0.21
SXDSW-32621	3.07±0.14	0.33±0.41	1.37±0.36	1.18±0.18	0.41±0.19	0.20±0.17
SXDSW-32712	0.96±0.09	0.30±0.25	...	1.27±0.16	0.85±0.16	0.51±0.15
SXDSW-32738	4.83±0.12	...	8.23±0.33	1.71±0.14	0.44±0.15	0.44±0.13
SXDSW-32770	5.18±0.12	0.22±0.40	0.57±0.26	...	0.33±0.16	...
SXDSW-32847	2.39±0.09	1.30±0.35	1.05±0.22	1.18±0.11	0.30±0.12	...
SXDSW-33128	11.11±0.20	24.12±0.69	58.48±0.72	6.24±0.34	2.75±0.34	1.59±0.25
SXDSW-33233	1.56±0.12	0.10±0.39	1.81±0.45	0.45±0.15	0.48±0.16	...
SXDSW-33555	1.06±0.10	0.78±0.22	2.40±0.25	0.63±0.22	0.07±0.16	0.12±0.10
SXDSW-33802	3.02±0.18	0.15±0.52	...	1.84±0.28	1.44±0.31	0.54±0.31
SXDSW-33968	10.71±0.16	1.75±0.50	9.66±0.56	4.85±0.22	2.02±0.20	0.77±0.17
SXDSW-34130	3.77±0.11	1.64±0.28	3.99±0.31	1.49±0.13	...	0.55±0.15

TABLE 2 — *Continued*

ID	[OII] ^a	[OIII]λ4959	[OIII]λ5007	Hβ	Hγ	Hδ
(1)	(2)	(3)	(4)	(5)	(6)	(7)

NOTE. — All line fluxes are in units of 10^{-17} erg s⁻¹ cm⁻².

^a The sum of the 3726 Å and 3729 Å lines.

TABLE 3
 STELLAR MASS, SFR, AND AGN CLASSIFICATION

ID	Mass	SFR _{SED}	SFR _{Hα,SED}	SFR _{Hα,Balmer}	AGN
(1)	$\log(M_{\odot})$ (2)	$\log(M_{\odot} \text{ yr}^{-1})$ (3)	$\log(M_{\odot} \text{ yr}^{-1})$ (4)	$\log(M_{\odot} \text{ yr}^{-1})$ (5)	(6)
SXDSN-12615	10.23±0.11	0.76±0.10	0.68±0.29	-1.75±0.75	0
SXDSN-14848	0.01±0.08	...	0
SXDSN-17153	11.15±0.06	1.88±0.05	1.73±0.19	0.27±0.38	0
SXDSN-17287	9.93±0.13	0.26±0.30	0.89±0.46	...	0
SXDSN-18372	10.01±0.08	0.70±0.09	0.81±0.35	1.79±0.64	0
SXDSN-18643	10.81	1.81	1.55±0.06	1.59±0.46	0
SXDSN-18689	10.48±0.12	0.77±0.33	1.32±0.42	0.79±0.74	0
SXDSN-18825	9.52±0.14	0.57±0.20	0.03±0.40	-1.14±0.49	0
SXDSN-19419	10.60±0.09	0.93±0.22	0.59±0.39	...	0
SXDSN-19725	10.16±0.10	0.99±0.18	1.05±0.40	...	0
SXDSN-19822	11.63	2.93	2.18±0.02	1.40±0.05	1
SXDSN-20554	9.39±0.12	0.14±0.13	0.00±0.21	...	0
SXDSN-20774	9.28±0.16	0.29±0.12	0.06±0.36	...	0
SXDSN-20874	9.66±0.10	0.47±0.21	0.51±0.37	...	0
SXDSN-22048	9.60±0.12	0.37±0.12	0.32±0.30	-0.32±0.47	0
SXDSN-22485	10.28±0.09	0.61±0.14	0.39±0.32	0.16±0.58	0
SXDSN-23784	9.96±0.10	0.95±0.21	0.58±0.40	0.20±0.40	0
SXDSN-23860	9.73±0.12	0.98±0.31	1.11±0.38	...	0
SXDSN-24371	11.28±0.07	2.39±0.14	2.44±0.10	...	0
SXDSN-24458	9.70±0.14	0.65±0.12	0.76±0.40	0.81±0.35	0
SXDSN-24652	9.39±0.11	0.14±0.12	0.05±0.21	...	0
SXDSN-24723	9.86±0.12	0.89±0.19	0.47±0.32	...	0
SXDSN-24979	9.74±0.12	0.26±0.09	0.00±0.49	...	0
SXDSN-25202	9.93±0.08	0.38±0.14	0.66±0.32	...	0
SXDSN-26559	10.01±0.12	0.92±0.17	0.53±0.28	...	0
SXDSN-26798	9.45±0.13	0.00±0.09	0.09±0.52	...	0
SXDSN-26828	9.50±0.18	1.18±0.12	0.76±0.38	...	0
SXDSN-27037	10.14±0.17	0.95±0.36	0.91±0.30	...	0
SXDSN-28032	9.73±0.11	0.63±0.10	0.65±0.36	-0.23±0.34	0
SXDSN-28267	9.91±0.09	1.13±0.13	1.21±0.10	0.86±0.33	0
SXDSN-29887	9.74±0.13	0.65±0.22	0.10±0.42	...	0
SXDSN-30551	9.82±0.12	0.88±0.18	0.69±0.49	0.27±0.35	0
SXDSN-31207	10.38±0.10	1.53±0.58	1.45±0.34	0.74±0.36	0
SXDSN-31304	11.78±0.03	2.54±0.03	2.07±0.11	...	0
SXDSN-31331	11.17±0.03	0.46±0.07	0.20±0.26	0.44±0.51	0
SXDSN-31929	7.45±0.07	-0.77±0.16	0
SXDSN-32915	9.35±0.13	1.14±0.15	0.78±0.33	-1.33±0.46	0
SXDSN-33371	10.09±0.09	1.95±0.08	0.82±0.32	...	0
SXDSN-34057	9.34±0.09	0.05±0.18	0.42±0.40	...	0
SXDSN-34591	9.56±0.11	0.44±0.16	0.37±0.38	...	0
SXDSN-34643	9.60±0.14	0.78±0.12	0.27±0.35	...	0
SXDSN-34925	9.88±0.16	1.38±0.19	0.83±0.34	-0.25±0.67	0
SXDSN-35304	9.65±0.14	0.47±0.23	0.48±0.36	...	0
SXDSN-35455	9.82±0.12	0.67±0.14	0.32±0.37	0.35±0.50	0
SXDSN-35945	10.58	1.79	1.54±0.32	-0.69±0.41	1
SXDSN-36476	9.10±0.13	0.37±0.13	-0.12±0.37	...	0
SXDSN-37348	9.52±0.12	0.13±0.12	0.04±0.24	...	0
SXDSN-37430	9.76±0.10	0.52±0.19	0.59±0.33	...	0
SXDSN-38796	11.20±0.08	2.22±0.33	1.35±0.30	1.08±0.29	0
SXDSN-39242	9.38±0.06	-0.02±0.13	0.22±0.16	-0.41±0.71	1
SXDSN-39615	9.74±0.10	0.78±0.20	0.20±0.41	...	0
SXDSN-39807	9.61±0.11	0.30±0.14	-0.17±0.27	...	0
SXDSN-41162	9.60±0.05	0.54±0.13	0.83±0.32	...	0
SXDSN-41683	10.44±0.12	1.53±0.24	1.05±0.35	...	0
SXDSN-41684	9.40±0.13	1.15±0.09	0
SXDSS-8347	9.62±0.09	0.71±0.12	0
SXDSS-12333	9.30±0.12	0.03±0.05	0
SXDSS-12862	10.77±0.17	1.43±0.35	1.24±0.32	...	0
SXDSS-14115	9.79±0.16	0.78±0.18	0.87±0.38	...	0
SXDSS-14438	9.27±0.07	0.00±0.05	0
SXDSS-14722	9.71±0.13	0.71±0.19	0
SXDSS-15629	9.58±0.14	0.16±0.09	-0.06±0.36	...	0
SXDSS-15945	9.66±0.10	0.45±0.09	-0.17±0.37	0.14±0.42	0
SXDSS-16362	10.45	0
SXDSS-16423	9.23±0.12	0.01±0.10	-0.77±0.37	...	0
SXDSS-16739	10.49±0.07	1.05±0.09	0.66±0.33	...	0
SXDSS-16866	9.37±0.11	0.18±0.10	0.01±0.75	...	0
SXDSS-17510	10.01±0.17	1.32±0.16	0.82±0.44	...	0
SXDSS-17705	9.60±0.16	0.64±0.20	0.83±0.43	...	0
SXDSS-17733	10.90±0.09	1.15±0.29	1.33±0.35	0.06±0.42	1
SXDSS-17787	0
SXDSS-17924	9.71±0.11	0.46±0.08	0.24±0.17	...	0
SXDSS-17941	0

TABLE 3 — *Continued*

ID	Mass	SFR _{SED}	SFR _{Hα,SED}	SFR _{Hα,Balmer}	AGN
(1)	$\log(M_{\odot})$ (2)	$\log(M_{\odot} \text{ yr}^{-1})$ (3)	$\log(M_{\odot} \text{ yr}^{-1})$ (4)	$\log(M_{\odot} \text{ yr}^{-1})$ (5)	(6)
SXDSS-17958	9.43±0.17	0.55±0.19	0.70±0.43	...	0
SXDSS-18093	9.46±0.14	0.55±0.19	0
SXDSS-18211	10.66±0.10	1.00±0.26	0.98±0.38	...	0
SXDSS-18370	0.04±0.15	...	0
SXDSS-18554	9.22±0.11	0.04±0.11	-0.06±0.44	...	0
SXDSS-18604	9.20±0.10	-0.03±0.02	0
SXDSS-18617	9.22±0.09	0.14±0.09	-0.19±0.27	...	0
SXDSS-18709	0
SXDSS-19166	10.99±0.10	1.44±0.45	1.56±0.32	...	1
SXDSS-19596	9.71±0.17	1.09±0.30	1.24±0.18	...	0
SXDSS-20389	9.29±0.12	0.07±0.15	0
SXDSS-20452	10.26±0.10	0.92±0.10	0.73±0.24	...	0
SXDSS-20675	9.91±0.10	0.86±0.38	0.86±0.33	1.64±0.66	0
SXDSS-21192	9.19±0.13	0.10±0.17	-0.28±0.40	...	0
SXDSS-21634	9.51±0.12	0.49±0.13	0.45±0.36	-0.78±0.56	0
SXDSS-21685	11.13±0.18	1.91±0.60	1.54±0.32	...	0
SXDSS-21861	0.31±0.05	0.35±0.31	0
SXDSS-21905	11.45±0.09	1.80±0.29	1.53±0.24	-1.95±0.63	1
SXDSS-22205	0.14±0.12	...	0
SXDSS-22262	11.05±0.09	1.34±0.25	0.95±0.52	...	0
SXDSS-22277	9.63±0.12	0.35±0.12	0.13±0.27	...	0
SXDSS-22355	10.85±0.03	2.28±0.24	1.79±0.17	...	0
SXDSS-22389	9.83±0.09	0.29±0.14	0.75±0.41	...	0
SXDSS-22452	9.53±0.10	0.42±0.10	0.22±0.23	...	0
SXDSS-22538	10.08±0.09	1.11±0.13	1.45±0.32	0.43±0.54	0
SXDSS-22557	9.26±0.13	0.09±0.12	-0.22±0.61	...	0
SXDSS-22717	10.09±0.11	0.07±0.18	0.61±0.40	...	0
SXDSS-22728	11.05±0.07	1.11±0.10	1.40±0.16	0.80±0.36	1
SXDSS-22887	9.09±0.07	0.19±0.18	0.57±0.45	...	0
SXDSS-22991	10.63±0.10	1.95±0.21	0
SXDSS-23082	9.42±0.09	0.44±0.11	0
SXDSS-23167	9.48±0.11	0.10±0.03	-0.29±0.08	...	0
SXDSS-23384	9.47±0.12	0.34±0.17	0.53±0.33	...	0
SXDSS-23393	10.32±0.08	1.48±0.16	1.40±0.44	1.50±0.26	1
SXDSS-23571	10.11±0.14	0.52±0.33	0.52±0.32	...	0
SXDSS-23647	10.01±0.09	1.14±0.18	1.09±0.48	0.48±0.33	0
SXDSS-23665	9.88±0.14	0.87±0.14	0.75±0.48	...	0
SXDSS-23667	10.00±0.12	0.75±0.15	0.50±0.34	1.28±0.55	0
SXDSS-23807	9.42±0.05	0.15±0.03	0
SXDSS-24027	9.72±0.17	1.15±0.17	1.06±0.33	0.34±0.49	0
SXDSS-24055	9.52±0.13	0.70±0.17	0.45±0.31	...	0
SXDSS-24177	9.70±0.08	0.50±0.19	0.28±0.33	...	0
SXDSS-24469	9.31±0.12	-0.05±0.13	0
SXDSS-24527	9.92±0.10	0.46±0.14	0.14±0.44	...	0
SXDSS-24609	10.48±0.08	1.23±0.09	1.06±0.12	1.21±0.27	0
SXDSS-26461	9.94±0.10	0.89±0.17	0.78±0.42	...	0
SXDSS-26565	9.32±0.14	0.35±0.13	0.11±0.38	...	0
SXDSS-26597	9.99±0.11	0.64±0.15	0.34±0.34	...	0
SXDSS-26724	9.50±0.16	0.88±0.21	0.91±0.43	...	0
SXDSS-27335	9.30±0.17	1.05±0.12	0.76±0.37	...	0
SXDSS-27364	9.47±0.10	0.04±0.10	0
SXDSS-27425	9.51±0.09	0.28±0.08	0.15±0.14	...	0
SXDSS-27514	10.67±0.15	0.34±0.50	0.52±0.55	...	0
SXDSS-27584	10.61±0.14	1.49±0.56	1.21±0.36	...	0
SXDSS-27730	10.62±0.08	0.44±0.12	0
SXDSS-27769	9.99±0.05	1.18±0.14	1.23±0.38	0.82±0.30	0
SXDSS-27865	10.12±0.12	0.56±0.27	0.81±0.37	...	0
SXDSS-27927	9.49±0.10	0.13±0.12	-0.01±0.29	0.90±0.57	0
SXDSS-28010	9.36±0.13	0.29±0.16	-0.22±0.34	...	0
SXDSS-28369	10.70±0.13	1.40±0.50	1.44±0.27	...	0
SXDSS-28490	9.65±0.10	0.73±0.21	-0.06±0.52	...	0
SXDSS-28526	9.93±0.19	1.52±0.14	1.11±0.24	0.60±0.47	0
SXDSS-28810	10.97±0.13	1.23±0.54	1.39±0.47	...	0
SXDSS-28845	10.78±0.12	1.79±0.19	1.50±0.31	0.57±0.75	0
SXDSS-28926	9.29±0.14	0.22±0.25	0
SXDSS-29206	9.55±0.10	0.16±0.04	-0.12±0.16	...	0
SXDSS-29259	9.48±0.15	0.26±0.25	0
SXDSS-29322	10.91±0.07	1.02±0.17	0.87±0.47	-2.35±0.86	0
SXDSS-29327	10.40±0.09	1.21±0.16	0.83±0.30	0.33±0.52	0
SXDSS-29607	10.20±0.12	0.82±0.36	0.66±0.48	...	0
SXDSS-29646	10.10±0.09	0.70±0.13	0.60±0.32	...	0
SXDSS-29754	10.55±0.08	0.69±0.16	0.80±0.42	...	0
SXDSS-29859	9.51±0.12	0.55±0.10	0.37±0.35	...	0
SXDSS-29972	9.15±0.07	0.43±0.14	0.43±0.37	...	0

TABLE 3 — *Continued*

ID	Mass	SFR _{SED}	SFR _{Hα,SED}	SFR _{Hα,Balmer}	AGN
(1)	$\log(M_{\odot})$ (2)	$\log(M_{\odot} \text{ yr}^{-1})$ (3)	$\log(M_{\odot} \text{ yr}^{-1})$ (4)	$\log(M_{\odot} \text{ yr}^{-1})$ (5)	(6)
SXDSS-30051	10.74±0.07	1.33±0.12	1.15±0.41	...	0
SXDSS-30124	9.37±0.07	0.06±0.01	-0.50±0.19	-2.23±0.76	0
SXDSS-30142	10.97±0.15	2.39±0.23	2.28±0.32	0.40±0.47	0
SXDSS-30295	9.80±0.06	0.56±0.08	0.17±0.38	0.30±0.31	1
SXDSS-31496	9.58±0.09	0.69±0.17	0.30±0.36	...	0
SXDSS-32097	10.12±0.09	1.00±0.12	0.83±0.29	0.93±0.26	0
SXDSS-32132	10.62±0.05	0.67±0.06	0.15±0.42	...	0
SXDSS-32277	9.88±0.06	0.70±0.06	0.80±0.10	0.16±0.59	0
SXDSS-32372	10.60±0.12	1.11±0.33	1.11±0.37	...	0
SXDSS-33021	9.69±0.12	0.36±0.12	-0.05±0.44	...	0
SXDSS-33298	9.00±9.00	9.00±9.00	4.13±3.07	1.00±0.17	0
SXDSS-33303	9.85±0.14	0.90±0.22	1.04±0.29	...	0
SXDSS-33787	9.37±0.07	0.08±0.02	-0.14±0.16	...	0
SXDSS-35437	9.90±0.17	1.15±0.32	1.06±0.40	1.29±0.42	0
SXDSS-35468	10.03±0.16	0.73±0.37	0.86±0.32	...	0
SXDSS-35702	9.52±0.10	0.51±0.19	0.44±0.35	0.54±0.43	0
SXDSS-35926	9.55±0.12	0.39±0.05	0.26±0.09	...	0
SXDSS-36006	9.73±0.12	0.76±0.29	1.10±0.39	0.72±0.53	0
SXDSS-36019	9.93±0.18	1.05±0.14	0.96±0.40	1.23±0.19	0
SXDSS-36053	9.91±0.14	0.33±0.14	0.19±0.24	...	0
SXDSS-36054	10.27±0.21	-0.53±0.96	0.99±0.52	...	0
SXDSS-36609	10.79±0.10	1.79±0.15	2.03±0.53	1.39±0.21	1
SXDSS-36655	10.24±0.13	0.82±0.38	1.04±0.39	...	0
SXDSS-36770	9.85±0.12	1.53±0.18	1.47±0.37	-0.20±0.34	0
SXDSS-36865	9.59±0.10	0.66±0.12	0.67±0.35	0.76±0.63	0
SXDSS-36954	9.38±0.11	-0.16±0.18	-0.40±0.29	...	0
SXDSS-36995	10.64±0.10	0.89±0.19	0.58±0.41	...	0
SXDSS-37057	9.19±0.12	0.21±0.17	0.06±0.34	-0.56±0.52	0
SXDSS-37189	9.22±0.02	-0.01±0.09	...	10.47	0
SXDSS-37234	9.46±0.08	0.25±0.20	0.65±0.47	...	0
SXDSS-37285	10.29±0.16	1.82±0.14	1.98±0.28	...	0
SXDSS-37540	9.91±0.07	1.23±0.16	1.12±0.35	-0.09±0.44	0
SXDSS-37564	9.64±0.08	0.52±0.14	0.43±0.35	-0.24±0.70	0
SXDSS-37774	9.82±0.18	0.96±0.30	1.06±0.31	0.58±0.41	0
SXDSS-37799	10.19±0.11	0.81±0.28	0.92±0.41	...	0
SXDSS-37947	9.71±0.10	0.43±0.24	0.44±0.41	...	0
SXDSS-37948	9.40±0.12	-0.16±0.16	0
SXDSS-38003	9.17±0.12	-0.12±0.17	0
SXDSS-38307	9.45±0.17	0.62±0.25	0.48±0.42	...	0
SXDSS-38485	10.45±0.09	0.60±0.22	1.14±0.34	...	0
SXDSS-38541	10.22	1.74	1.12±0.05	...	0
SXDSS-38602	10.46±0.14	0.47±0.50	1.27±0.43	...	0
SXDSS-38698	10.62±0.05	1.44±0.07	1.51±0.20	1.18±0.18	0
SXDSS-38754	9.27±0.12	0.15±0.10	0
SXDSS-38784	10.59±0.13	1.64±0.53	1.50±0.31	...	0
SXDSS-39016	10.03±0.16	1.04±0.13	0.98±0.35	0.98±0.35	0
SXDSS-39160	9.34±0.11	0.07±0.12	-0.26±0.11	...	1
SXDSS-39161	10.74±0.06	1.60±0.21	1.62±0.32	...	0
SXDSS-39226	9.99±0.11	0.83±0.35	0.84±0.36	...	0
SXDSS-39288	10.02±0.09	1.10±0.12	1.49±0.31	1.00±0.15	1
SXDSS-39308	9.60±0.14	0.46±0.16	0.06±0.51	...	0
SXDSS-39501	9.66±0.10	-0.06±0.21	0.20±0.49	...	0
SXDSS-39548	9.77±0.14	0.72±0.18	0.45±0.42	...	0
SXDSS-39672	10.18±0.14	0.53±0.42	0.66±0.48	...	0
SXDSS-40071	0.27±0.06	...	0
SXDSS-40327	9.78±0.10	0.67±0.58	0.79±0.42	...	0
SXDSS-40667	9.77±0.04	1.62±0.02	0.14±0.26	0.57±0.54	0
SXDSS-41193	9.78±0.15	0.55±0.08	0.30±0.10	0.70±0.29	0
SXDSS-41546	10.98	2.53	2.10±0.06	...	0
SXDSW-8210	9.63±0.16	0.71±0.20	0.16±0.33	-4.22±0.48	0
SXDSW-9136	9.58±0.19	0.84±0.19	0.80±0.27	...	0
SXDSW-10296	10.11±0.14	1.26±0.32	1.21±0.38	1.29±0.27	1
SXDSW-11479	9.45±0.08	0.19±0.03	0.02±0.07	0.51±0.53	0
SXDSW-11971	9.92±0.14	1.01±0.13	0.97±0.39	0.33±0.41	0
SXDSW-12128	10.05±0.12	1.50±0.09	1.78±0.40	0.57±0.14	0
SXDSW-12844	9.52±0.10	0.20±0.17	0.10±0.23	...	0
SXDSW-12890	10.59±0.10	1.70±0.09	1.86±0.14	...	1
SXDSW-12994	10.65±0.12	0.98±0.18	0.80±0.38	6.31±0.23	0
SXDSW-13080	9.65±0.08	0.43±0.15	0.49±0.31	...	0
SXDSW-13103	9.54±0.09	-0.11±0.03	-0.41±0.18	...	0
SXDSW-13564	10.00±0.12	0.40±0.28	0.59±0.46	...	0
SXDSW-13607	9.97±0.15	0.67±0.71	1.15±0.43	...	0
SXDSW-13984	9.20±0.11	0.06±0.14	0.01±0.36	0.49±0.66	0
SXDSW-14140	9.81±0.09	0.41±0.16	0.23±0.30	...	0

TABLE 3 — *Continued*

ID	Mass	SFR _{SED}	SFR _{Hα,SED}	SFR _{Hα,Balmer}	AGN
(1)	$\log(M_{\odot})$ (2)	$\log(M_{\odot} \text{ yr}^{-1})$ (3)	$\log(M_{\odot} \text{ yr}^{-1})$ (4)	$\log(M_{\odot} \text{ yr}^{-1})$ (5)	(6)
SXDSW-14401	9.65±0.14	0.64±0.16	0.01±0.42	...	0
SXDSW-14539	9.16	-0.14±0.05	-0.16±0.12	...	0
SXDSW-14721	10.59±0.12	0.83±0.25	0.76±0.42	...	0
SXDSW-14768	9.87±0.10	0.68±0.10	0.29±0.32	0.36±0.15	0
SXDSW-15154	10.91±0.05	1.81±0.17	1.86±0.18	1.37±0.10	1
SXDSW-15503	9.81±0.12	0.68±0.19	0.29±0.43	0.71±0.44	0
SXDSW-15809	10.15±0.10	0.89±0.17	0.80±0.41	...	0
SXDSW-16014	0
SXDSW-16198	9.62±0.11	0.38±0.12	0.30±0.34	...	0
SXDSW-16925	9.04±0.15	0.32±0.19	-0.21±0.42	...	0
SXDSW-17066	10.30±0.09	1.70±0.06	2.19±0.22	1.74±0.13	1
SXDSW-17078	9.27±0.16	0.22±0.19	0.25±0.44	...	0
SXDSW-17122	0.48±0.03	1.61±0.32	0
SXDSW-17661	10.50±0.09	0.75±0.19	1.21±0.42	...	0
SXDSW-17713	10.27±0.05	1.25±0.13	1.89±0.48	...	0
SXDSW-17857	10.74±0.09	1.36±0.27	1.51±0.34	0.18±0.37	0
SXDSW-17950	10.72±0.08	1.12±0.21	0.93±0.43	...	0
SXDSW-18358	9.90±0.06	1.36±0.24	1.25±0.37	...	0
SXDSW-18531	0.00±0.06	-1.03±0.16	0
SXDSW-18825	9.68±0.02	0.63±0.08	1.27±0.33	0.33±0.42	0
SXDSW-19290	10.70±0.15	1.89±0.14	1.51±0.23	...	0
SXDSW-19359	9.62±0.10	-0.03±0.22	0.35±0.48	...	0
SXDSW-19641	10.51±0.07	0.23±0.14	0.43±0.46	-0.63±0.26	0
SXDSW-20331	9.26±0.11	-0.05±0.04	-0.14±0.09	...	0
SXDSW-20516	9.75±0.09	0.73±0.09	0.76±0.35	0.71±0.30	0
SXDSW-20939	9.64±0.08	0.57±0.05	0.29±0.04	...	0
SXDSW-20960	9.69±0.09	0.31±0.10	0.24±0.18	-1.11±0.18	0
SXDSW-21422	10.82±0.10	1.31±0.17	1.12±0.24	...	0
SXDSW-21499	9.51±0.11	0.14±0.10	-0.14±0.23	0.60±0.53	0
SXDSW-21553	10.29±0.19	1.55±0.17	1.35±0.26	...	0
SXDSW-21649	10.43±0.09	1.20±0.17	1.40±0.28	...	0
SXDSW-22444	9.27±0.12	-0.10±0.06	-0.24±0.07	...	0
SXDSW-22739	9.51±0.13	0.30±0.13	-0.09±0.40	...	0
SXDSW-23533	9.95±0.12	1.01±0.14	1.26±0.42	1.38±0.26	0
SXDSW-23680	9.91±0.07	0.48±0.03	0.57±0.05	0.65±0.22	1
SXDSW-24515	9.67	0.57	0.14±0.07	0.22±0.29	0
SXDSW-24564	9.36±0.07	0.43±0.21	1.06±0.41	...	0
SXDSW-24653	9.70±0.11	0.95±0.17	0.75±0.40	0.47±0.47	0
SXDSW-24734	9.61±0.09	0.46±0.17	0.49±0.27	-0.01±0.51	0
SXDSW-24830	11.03±0.18	0.88±0.84	1.54±0.45	...	0
SXDSW-25068	9.72±0.15	0.91±0.10	0.88±0.36	0.45±0.12	1
SXDSW-25191	9.26±0.11	-0.04±0.19	0.10±0.40	...	0
SXDSW-25629	9.40±0.15	0.33±0.15	0.23±0.26	-0.19±0.60	0
SXDSW-25713	9.40±0.14	0.29±0.13	0.16±0.38	...	0
SXDSW-25776	9.29±0.03	-1.32±0.04	-0.08±0.09	...	0
SXDSW-26008	9.41±0.06	0.32±0.02	0.05±0.08	...	1
SXDSW-26127	9.38±0.14	0.34±0.20	0.49±0.31	...	0
SXDSW-26406	10.56±0.12	2.03±0.17	1.98±0.26	1.74±0.22	0
SXDSW-26551	9.47±0.12	0.27±0.13	-0.15±0.17	...	0
SXDSW-26690	9.50±0.13	0.26±0.13	-0.07±0.29	...	0
SXDSW-26823	9.95±0.12	0.66±0.23	0.28±0.31	...	0
SXDSW-26847	11.09±0.06	1.85±0.31	1.66±0.25	...	1
SXDSW-26877	9.54±0.10	0.28±0.14	0.19±0.32	...	0
SXDSW-26991	9.31±0.14	0.45±0.18	0.45±0.42	...	0
SXDSW-27153	10.68±0.05	1.16±0.09	1.18±0.13	-0.35±0.24	0
SXDSW-27756	10.26±0.08	0.91±0.09	1.05±0.36	-0.64±0.64	0
SXDSW-28087	10.32±0.11	0.85±0.24	0.87±0.37	...	0
SXDSW-28260	9.68±0.07	0.59±0.17	0.64±0.26	0.39±0.30	0
SXDSW-28609	9.27±0.15	0.21±0.13	0.28±0.36	0.84±0.68	0
SXDSW-29408	8.86±0.07	0.29±0.25	0
SXDSW-30365	9.70±0.12	0.52±0.10	0.16±0.34	-0.16±0.34	0
SXDSW-31064	10.07±0.08	0.87±0.36	0.83±0.37	0.58±0.49	0
SXDSW-31476	10.65±0.12	1.15±0.28	1.18±0.36	...	0
SXDSW-31483	10.11±0.09	0.24±0.22	0.57±0.35	...	0
SXDSW-31939	9.70±0.11	0.37±0.15	0.46±0.36	-0.83±0.51	0
SXDSW-31979	9.73	0.66	1.59±0.06	-1.37±0.33	0
SXDSW-32006	9.49±0.12	0.19±0.18	0.18±0.38	-2.13±0.62	0
SXDSW-32621	9.33±0.12	0.05±0.12	-0.28±0.36	...	0
SXDSW-32712	10.96±0.14	1.65±0.52	1.50±0.39	-0.69±0.66	0
SXDSW-32738	9.27±0.13	0.14±0.14	0.24±0.40	...	0
SXDSW-32770	9.63±0.10	0.19±0.13	0.18±0.21	...	0
SXDSW-32847	9.71±0.11	0.23±0.16	-0.01±0.35	...	0
SXDSW-33128	11.17±0.09	2.32±0.05	2.18±0.14	0.76±0.38	1
SXDSW-33233	9.45±0.14	0.65±0.18	0.21±0.54	...	0

TABLE 3 — *Continued*

ID	Mass	SFR _{SED}	SFR _{Hα,SED}	SFR _{Hα,Balmer}	AGN
(1)	$\log(M_{\odot})$ (2)	$\log(M_{\odot} \text{ yr}^{-1})$ (3)	$\log(M_{\odot} \text{ yr}^{-1})$ (4)	$\log(M_{\odot} \text{ yr}^{-1})$ (5)	(6)
SXDSW-33555	9.32±0.17	0.57±0.32	0.52±0.41	...	0
SXDSW-33802	9.20±0.07	-0.32±0.01	0.17±0.07	...	0
SXDSW-33968	9.69±0.09	0.41±0.09	0.20±0.08	0.37±0.29	0
SXDSW-34130	9.70±0.12	0.46±0.09	0.17±0.27	...	0

NOTE. — Ellipses indicate weak measurements. (2): Stellar mass determinations are described in Section 3.1. (3): SFR based on SED fitting. (4): H α SFR, dereddened using the prescription of Charlot & Fall (2000) and SED results. (5): H α SFR, dereddened using the Balmer decrement. (6): “1” denotes AGN, using diagnostics described in Section 2.2.

TABLE 4
NEWH α SED-CORRECTED METALLICITIES

ID	M91 upper	M91 lower	Z94	T04	N06	KK04 upper	KK04 lower
SXDSN-12615	8.661±0.120	7.986±0.179	8.768±0.132	8.713±0.119	8.700	8.828	8.177
SXDSN-18825	8.568±0.079	8.149±0.092	8.672±0.097	8.635±0.068	8.601	8.734	8.302
SXDSN-19822	8.944±0.002	7.362±0.006	9.102±0.003	9.020±0.003	9.066	9.049	7.680
SXDSN-20554	8.956±0.026	7.408±0.069	9.122±0.032	9.041±0.033	9.094	9.066	7.701
SXDSN-22048	8.295±0.183	8.487±0.202	8.358±0.256	8.400±0.172	...	8.410	8.574
SXDSN-22485	8.819±0.058	7.783±0.116	8.973±0.063	8.894±0.058	8.911	8.985	7.992
SXDSN-23784	8.814±0.039	7.770±0.100	8.962±0.043	8.884±0.039	8.899	8.977	7.988
SXDSN-23860	8.903±0.048	8.413±0.172	7.597±0.116	9.065±0.054	8.983±0.052	9.019	9.043
SXDSN-24371	8.948±0.027	7.500±0.099	9.118±0.033	9.036±0.030	9.088	9.072	7.759
SXDSN-24458	8.830±0.026	7.763±0.054	8.985±0.030	8.906±0.028	8.924	8.993	7.975
SXDSN-24652	8.413±0.172	8.256±0.291	8.315±0.286	8.370±0.230	...	8.448	8.427
SXDSN-26559	8.829±0.078	7.850±0.175	8.998±0.087	8.917±0.081	8.938	9.002	8.022
SXDSN-26798	8.459±0.122	8.250±0.153	8.496±0.171	8.500±0.111	8.395	8.580	8.400
SXDSN-26828	8.164±0.119	8.633±0.101	8.232±0.139	8.313±0.116	...	8.262	8.685
SXDSN-27037	8.929±0.058	7.699±0.188	9.106±0.059	9.024±0.058	9.072	9.079	7.881
SXDSN-28032	8.427±0.113	8.278±0.144	8.436±0.151	8.456±0.117	8.296	8.528	8.427
SXDSN-28267	8.584±0.053	8.028±0.076	8.609±0.080	8.585±0.061	8.534	8.712	8.233
SXDSN-31207	9.039±0.019	7.238±0.081	9.230±0.024	9.151±0.027	...	9.126	7.538
SXDSN-31304	8.985±0.034	7.401±0.101	9.161±0.040	9.081±0.041	9.151	9.093	7.677
SXDSN-31331	9.008±0.028	7.320±0.117	9.189±0.032	9.110±0.032	9.196	9.104	7.613
SXDSN-31929	8.449±0.116	8.268±0.255	7.886±0.286	8.089±0.187	...	8.226	8.466
SXDSN-32915	8.825±0.058	7.731±0.137	8.971±0.065	8.892±0.067	8.909	8.984	7.960
SXDSN-34643	8.710±0.071	7.908±0.117	8.828±0.083	8.763±0.077	8.759	8.878	8.113
SXDSN-34925	8.556±0.152	8.130±0.198	8.631±0.173	8.603±0.145	8.559	8.707	8.298
SXDSN-35455	8.838±0.036	7.706±0.067	8.986±0.042	8.907±0.035	8.926	8.994	7.939
SXDSN-35945	8.922±0.018	7.364±0.089	9.067±0.022	8.985±0.021	9.021	9.030	7.692
SXDSN-36476	8.491±0.146	8.227±0.217	8.557±0.188	8.546±0.138	8.474	8.632	8.375
SXDSN-38796	9.053±0.021	7.274±0.103	9.249±0.027	9.170±0.029	...	9.155	7.541
SXDSN-39242	8.555±0.107	8.047±0.176	8.532±0.193	8.527±0.138	8.443	8.657	8.257
SXDSN-39615	8.433±0.182	8.317±0.186	8.505±0.207	8.507±0.147	8.407	8.572	8.441
SXDSN-39807	8.672±0.094	7.939±0.164	8.764±0.124	8.710±0.112	8.695	8.831	8.147
SXDSN-41162	8.384±0.215	8.326±0.309	8.367±0.312	8.407±0.210	...	8.462	8.469
SXDSS-8347	8.129±0.265	8.627±0.281	8.092±0.385	8.220±0.256	...	8.143	8.704
SXDSS-12862	9.019±0.034	7.345±0.162	9.204±0.053	9.125±0.053	9.220	9.121	7.617
SXDSS-14115	8.734±0.103	7.977±0.174	8.890±0.112	8.818±0.095	8.822	8.918	8.138
SXDSS-14438	8.315±0.198	8.440±0.231	8.342±0.262	8.389±0.177	...	8.410	8.548
SXDSS-14722	8.643±0.085	7.995±0.127	8.733±0.090	8.684±0.072	8.664	8.802	8.190
SXDSS-15629	8.614±0.144	8.133±0.163	8.750±0.134	8.698±0.108	8.682	8.798	8.273
SXDSS-15945	8.553±0.096	8.162±0.152	8.648±0.101	8.616±0.079	8.577	8.714	8.316
SXDSS-16362	8.261±0.082	8.457±0.106	8.134±0.112	8.248±0.074	...	8.243	8.586
SXDSS-17510	8.285±0.179	8.473±0.171	8.369	8.575
SXDSS-17705	8.543±0.140	8.104±0.160	8.568±0.167	8.554±0.135	8.487	8.667	8.291
SXDSS-17733	8.643±0.101	8.057±0.137	8.767±0.116	8.713±0.102	8.699	8.819	8.222
SXDSS-17924	8.422±0.148	8.332±0.177	8.494±0.171	8.499±0.135	8.391	8.560	8.453
SXDSS-17941	8.420±0.153	8.318±0.183	8.472±0.188	8.482±0.150	8.358	8.546	8.448
SXDSS-17958	8.466±0.117	8.232±0.156	8.493±0.126	8.498±0.091	8.390	8.582	8.388
SXDSS-18370	8.276±0.109	8.445±0.123	8.184±0.156	8.281±0.112	...	8.284	8.572
SXDSS-18554	8.196±0.066	8.564±0.063	8.185±0.094	8.281±0.063	...	8.243	8.651
SXDSS-18617	8.534±0.065	8.100±0.105	8.533±0.098	8.527±0.073	8.444	8.644	8.293
SXDSS-19166	8.727±0.104	7.922±0.180	8.863±0.112	8.794±0.104	8.794	8.901	8.113
SXDSS-20452	8.905±0.060	7.822±0.146	9.087±0.056	9.005±0.056	9.046	9.071	7.961
SXDSS-20675	8.951±0.063	7.555±0.175	9.124±0.068	9.043±0.067	9.097	9.082	7.788
SXDSS-21192	8.482±0.172	8.196±0.220	8.495±0.266	8.500±0.198	8.393	8.593	8.364
SXDSS-21634	8.414±0.122	8.290±0.139	8.411±0.142	8.438±0.100	8.239	8.505	8.439
SXDSS-21861	8.665±0.060	7.936±0.108	8.747±0.096	8.696±0.058	8.678	8.820	8.149
SXDSS-21905	8.880±0.057	7.594±0.133	9.032±0.069	8.950±0.072	8.978	9.021	7.854
SXDSS-22205	8.589±0.098	8.117±0.139	8.695±0.114	8.653±0.090	8.625	8.757	8.277
SXDSS-22277	8.448±0.165	8.309±0.200	8.533±0.213	8.528±0.168	8.445	8.597	8.431
SXDSS-22355	8.773±0.136	7.778±0.274	8.896±0.161	8.824±0.191	8.829	8.933	8.012
SXDSS-22452	8.314±0.060	8.735±0.047	7.102±0.050	7.634±0.027	...	7.588	8.886

TABLE 4 — *Continued*

ID	M91 upper	M91 lower	Z94	T04	N06	KK04 upper	KK04 lower
SXDSS-22538	8.969±0.014	7.534±0.031	9.145±0.014	9.065±0.015	9.128	9.096	7.764
SXDSS-22557	8.684±0.099	7.928±0.155	8.785±0.125	8.727±0.101	8.717	8.847	8.136
SXDSS-22728	8.828±0.021	7.723±0.033	8.974±0.025	8.895±0.023	8.912	8.986	7.954
SXDSS-22991	8.808±0.100	7.897±0.183	8.978±0.106	8.898±0.093	8.916	8.987	8.058
SXDSS-23167	8.679±0.038	7.873±0.068	8.742±0.056	8.691±0.050	8.673	8.826	8.107
SXDSS-23393	8.819±0.051	7.766±0.124	8.970±0.055	8.891±0.051	8.907	8.982	7.982
SXDSS-23647	8.561±0.080	8.186±0.130	8.681±0.090	8.642±0.070	8.611	8.736	8.323
SXDSS-23667	8.929±0.031	7.532±0.074	9.095±0.036	9.013±0.040	9.057	9.059	7.790
SXDSS-24027	8.393±0.113	8.331±0.139	8.407±0.138	8.435±0.097	8.227	8.491	8.467
SXDSS-24469	8.805±0.127	7.795±0.222	8.953±0.116	8.876±0.118	8.889	8.971	8.006
SXDSS-24609	8.901±0.026	7.668±0.067	9.069±0.029	8.987±0.029	9.024	9.050	7.883
SXDSS-26565	8.413±0.177	8.288±0.226	8.403±0.235	8.432±0.176	8.216	8.500	8.439
SXDSS-26597	8.748±0.102	7.949±0.185	8.904±0.095	8.830±0.093	8.836	8.930	8.117
SXDSS-26724	8.758±0.113	7.791±0.200	8.873±0.151	8.803±0.119	8.805	8.918	8.026
SXDSS-27335	8.589±0.129	8.064±0.193	8.658±0.177	8.624±0.129	8.587	8.738	8.250
SXDSS-28369	8.940±0.070	7.578±0.172	9.112±0.077	9.030±0.084	9.080	9.075	7.808
SXDSS-28526	8.533±0.077	8.243±0.092	8.662±0.090	8.627±0.070	8.591	8.713	8.362
SXDSS-29206	8.501±0.109	8.191±0.148	8.546±0.134	8.537±0.099	8.461	8.631	8.353
SXDSS-29259	8.635±0.135	8.069±0.218	8.759±0.167	8.705±0.150	8.690	8.811	8.232
SXDSS-29327	8.921±0.048	7.669±0.140	9.095±0.060	9.013±0.050	9.057	9.069	7.870
SXDSS-29859	8.440±0.094	8.242±0.124	8.417±0.132	8.443±0.092	8.255	8.524	8.406
SXDSS-30051	8.990±0.028	7.434±0.089	9.168±0.033	9.088±0.038	9.162	9.103	7.692
SXDSS-30124	8.164±0.188	8.588±0.197	8.122±0.299	8.240±0.190	...	8.183	8.675
SXDSS-30142	8.942±0.037	7.524±0.098	9.111±0.042	9.029±0.042	9.078	9.069	7.777
SXDSS-30295	8.533±0.072	8.104±0.107	8.537±0.087	8.531±0.065	8.449	8.646	8.296
SXDSS-31496	8.898±0.024	7.615±0.048	9.060±0.031	8.978±0.029	9.012	9.040	7.855
SXDSS-32097	8.820±0.052	7.785±0.124	8.974±0.056	8.895±0.050	8.912	8.985	7.993
SXDSS-32132	8.333±0.152	8.470±0.150	8.432±0.163	8.453±0.128	8.287	8.478	8.549
SXDSS-32277	8.697±0.102	8.124±0.142	8.876±0.103	8.806±0.089	8.808	8.901	8.228
SXDSS-33021	8.741±0.086	7.870±0.138	8.870±0.118	8.800±0.090	8.802	8.910	8.078
SXDSS-33298	8.805±0.069	7.810±0.147	8.958±0.073	8.880±0.067	8.894	8.973	8.014
SXDSS-33787	8.600±0.048	7.996±0.078	8.622±0.070	8.596±0.053	8.549	8.728	8.209
SXDSS-35437	9.020±0.033	7.478±0.144	9.206±0.041	9.127±0.042	9.224	9.143	7.686
SXDSS-36006	8.801±0.091	7.842±0.132	8.957±0.092	8.879±0.075	8.894	8.973	8.033
SXDSS-36019	8.741±0.047	7.842±0.082	8.860±0.049	8.791±0.042	8.792	8.905	8.063
SXDSS-36053	8.741±0.134	7.959±0.256	8.896±0.139	8.823±0.145	8.828	8.923	8.125
SXDSS-36609	8.885±0.031	7.608±0.081	9.041±0.034	8.960±0.033	8.990	9.028	7.859
SXDSS-36655	8.712±0.098	7.946±0.163	8.845±0.112	8.779±0.094	8.777	8.887	8.133
SXDSS-36770	8.921±0.028	7.630±0.081	9.092±0.030	9.010±0.029	9.054	9.064	7.849
SXDSS-36865	8.699±0.083	7.996±0.149	8.840±0.091	8.774±0.085	8.772	8.880	8.165
SXDSS-36954	8.248±0.205	8.528±0.201	8.289±0.297	8.352±0.213	...	8.341	8.612
SXDSS-37057	8.749±0.047	7.845±0.103	8.876±0.056	8.805±0.053	8.808	8.916	8.060
SXDSS-37189	8.691±0.066	7.809±0.132	8.724±0.096	8.677±0.077	8.655	8.827	8.065
SXDSS-37234	7.971±0.322	8.763±0.267	7.804±0.475	8.038±0.289	...	7.849	8.829
SXDSS-37285	8.854±0.052	7.651±0.140	9.001±0.057	8.921±0.054	8.943	9.003	7.900
SXDSS-37540	8.845±0.024	7.733±0.043	9.001±0.031	8.921±0.027	8.942	9.004	7.951
SXDSS-37564	8.644±0.116	7.999±0.186	8.740±0.144	8.690±0.126	8.671	8.807	8.191
SXDSS-37774	8.897±0.038	7.623±0.095	9.059±0.041	8.978±0.039	9.012	9.041	7.861
SXDSS-37948	8.595±0.148	8.098±0.225	8.695±0.180	8.653±0.150	8.625	8.760	8.265
SXDSS-38003	8.152±0.262	8.590±0.261	8.064±0.361	8.202±0.274	...	8.135	8.684
SXDSS-38307	8.945±0.067	7.405±0.229	9.106±0.073	9.025±0.079	9.072	9.056	7.706
SXDSS-38541	8.950±0.037	7.523±0.091	9.121±0.044	9.040±0.044	9.093	9.077	7.771
SXDSS-38698	8.871±0.030	7.884±0.068	9.054±0.026	8.972±0.026	9.004	9.046	8.014
SXDSS-38754	8.622±0.037	7.947±0.052	8.641±0.062	8.610±0.040	8.569	8.750	8.173
SXDSS-39016	8.706±0.068	8.021±0.126	8.860±0.071	8.791±0.061	8.792	8.893	8.175
SXDSS-39160	8.920±0.031	7.252±0.114	9.047±0.047	8.965±0.051	8.996	9.015	7.617
SXDSS-39226	8.994±0.037	7.365±0.115	9.171±0.045	9.091±0.050	9.167	9.096	7.650
SXDSS-39288	8.668±0.023	7.923±0.040	8.747±0.029	8.696±0.024	8.678	8.822	8.140
SXDSS-39308	8.449±0.099	8.262±0.142	8.482±0.139	8.490±0.101	8.374	8.567	8.410
SXDSS-39548	8.561±0.063	8.085±0.106	8.602±0.076	8.580±0.058	8.527	8.695	8.273
SXDSS-40071	8.945±0.062	7.589±0.199	9.119±0.070	9.037±0.073	9.090	9.081	7.811
SXDSS-40667	8.814±0.050	7.720±0.109	8.951±0.062	8.873±0.051	8.886	8.971	7.959
SXDSS-41193	8.584±0.019	8.037±0.029	8.619±0.031	8.594±0.022	8.546	8.717	8.238
SXDSS-8210	8.574±0.134	8.241±0.166	8.733±0.144	8.684±0.115	8.664	8.772	8.342
SXDSS-9136	8.611±0.106	8.035±0.154	8.689±0.135	8.648±0.112	8.619	8.765	8.225
SXDSS-10296	8.606±0.060	8.034±0.098	8.675±0.070	8.637±0.055	8.605	8.756	8.227
SXDSS-11479	8.766±0.056	7.750±0.123	8.874±0.075	8.804±0.079	8.806	8.922	7.999
SXDSS-11971	8.469±0.149	8.288±0.176	8.563±0.177	8.550±0.130	8.481	8.625	8.412
SXDSS-12128	8.340±0.052	8.408±0.059	8.365±0.065	8.406±0.041	...	8.437	8.523
SXDSS-12890	8.797±0.075	7.818±0.154	8.947±0.081	8.870±0.081	8.882	8.966	8.023
SXDSS-13103	8.346±0.156	8.344±0.235	8.203±0.238	8.294±0.168	...	8.339	8.500
SXDSS-13564	9.020±0.038	7.264±0.148	9.205±0.054	9.126±0.054	9.222	9.107	7.570
SXDSS-13984	8.550±0.086	8.221±0.095	8.680±0.094	8.641±0.080	8.610	8.731	8.344
SXDSS-14401	8.126±0.187	8.644±0.166	8.131±0.243	8.246±0.155	...	8.170	8.709
SXDSS-14721	8.897±0.044	7.657±0.097	9.063±0.043	8.981±0.042	9.016	9.045	7.880
SXDSS-14768	8.546±0.052	8.065±0.097	8.524±0.068	8.521±0.045	8.433	8.647	8.270
SXDSS-15154	8.781±0.054	7.869±0.116	8.934±0.055	8.858±0.050	8.868	8.955	8.058

TABLE 4 — *Continued*

ID	M91 upper	M91 lower	Z94	T04	N06	KK04 upper	KK04 lower
SXDSW-15503	8.913±0.044	7.560±0.130	9.075±0.049	8.993±0.049	9.031	9.048	7.816
SXDSW-15809	9.027±0.017	7.216±0.064	9.214±0.023	9.135±0.023	9.238	9.106	7.537
SXDSW-17066	8.697±0.055	7.893±0.104	8.795±0.069	8.735±0.057	8.726	8.857	8.111
SXDSW-17078	8.287±0.211	8.489±0.226	8.337±0.268	8.386±0.182	...	8.393	8.579
SXDSW-17122	8.798±0.028	7.708±0.055	8.921±0.036	8.846±0.032	8.855	8.953	7.960
SXDSW-17857	8.885±0.058	7.721±0.131	9.055±0.060	8.973±0.059	9.006	9.042	7.921
SXDSW-17950	9.051±0.018	7.252±0.100	9.246±0.028	9.167±0.028	...	9.147	7.532
SXDSW-18531	8.805±0.038	7.641±0.104	8.913±0.051	8.839±0.046	8.846	8.951	7.917
SXDSW-18825	8.570±0.044	7.992±0.073	8.485±0.082	8.492±0.054	8.379	8.646	8.222
SXDSW-19359	8.733±0.128	7.945±0.196	8.879±0.129	8.809±0.122	8.811	8.912	8.122
SXDSW-19641	9.011±0.017	7.279±0.087	9.193±0.022	9.113±0.023	9.201	9.099	7.587
SXDSW-20516	8.760±0.040	7.708±0.106	8.841±0.053	8.775±0.045	8.773	8.907	7.976
SXDSW-20939	8.912±0.025	7.553±0.058	9.072±0.030	8.990±0.030	9.028	9.045	7.812
SXDSW-20960	8.464±0.127	8.312±0.155	8.571±0.124	8.557±0.105	8.491	8.627	8.425
SXDSW-21422	8.932±0.028	7.446±0.078	9.091±0.038	9.009±0.034	9.052	9.050	7.738
SXDSW-21499	8.961±0.027	7.389±0.083	9.128±0.033	9.046±0.033	9.102	9.067	7.687
SXDSW-21553	8.772±0.091	7.887±0.182	8.926±0.104	8.850±0.090	8.860	8.949	8.072
SXDSW-22444	8.573±0.110	8.086±0.169	8.635±0.149	8.606±0.111	8.562	8.718	8.268
SXDSW-23533	8.636±0.076	8.102±0.127	8.775±0.089	8.719±0.074	8.706	8.820	8.248
SXDSW-23680	8.546±0.068	8.070±0.109	8.533±0.079	8.528±0.065	8.444	8.652	8.272
SXDSW-24515	8.524±0.023	8.106±0.030	8.506±0.033	8.508±0.027	8.408	8.624	8.301
SXDSW-24653	8.885±0.047	7.669±0.138	9.048±0.051	8.966±0.048	8.997	9.035	7.893
SXDSW-24830	9.093±0.011	6.893±0.050	9.324±0.020	9.240±0.019	...	9.149	7.293
SXDSW-25068	8.463±0.057	8.211±0.092	8.449±0.069	8.466±0.049	8.320	8.556	8.380
SXDSW-25629	8.577±0.102	8.105±0.138	8.659±0.114	8.625±0.087	8.588	8.732	8.276
SXDSW-25776	8.671±0.126	7.896±0.216	8.736±0.151	8.687±0.159	8.667	8.819	8.124
SXDSW-26406	8.802±0.072	7.853±0.143	8.961±0.073	8.883±0.067	8.898	8.975	8.039
SXDSW-26551	8.424±0.089	8.299±0.137	8.458±0.107	8.472±0.086	8.335	8.539	8.438
SXDSW-26690	8.678±0.094	8.046±0.144	8.824±0.107	8.760±0.098	8.755	8.864	8.200
SXDSW-26823	8.935±0.035	7.562±0.125	9.104±0.038	9.022±0.038	9.069	9.068	7.803
SXDSW-26847	8.964±0.040	7.392±0.086	9.133±0.051	9.052±0.051	9.109	9.071	7.686
SXDSW-26877	8.615±0.110	8.058±0.145	8.713±0.120	8.668±0.095	8.644	8.779	8.235
SXDSW-26991	8.410±0.172	8.336±0.254	8.467±0.202	8.479±0.160	8.350	8.537	8.461
SXDSW-27153	9.015±0.017	7.255±0.086	9.197±0.022	9.118±0.023	9.209	9.099	7.569
SXDSW-27756	8.887±0.043	7.615±0.117	9.045±0.048	8.963±0.047	8.994	9.030	7.862
SXDSW-28087	8.978±0.021	7.350±0.057	9.149±0.026	9.068±0.027	9.133	9.077	7.653
SXDSW-28260	8.538±0.022	8.131±0.032	8.584±0.031	8.566±0.024	8.505	8.672	8.307
SXDSW-28609	8.341±0.164	8.367±0.192	8.274±0.213	8.342±0.157	...	8.380	8.509
SXDSW-30365	8.319±0.066	8.480±0.067	8.410±0.079	8.438±0.057	8.238	8.457	8.560
SXDSW-31064	8.928±0.042	7.555±0.118	9.094±0.054	9.013±0.041	9.057	9.060	7.804
SXDSW-31483	8.364±0.100	8.314±0.136	8.174±0.199	8.274±0.130	...	8.332	8.481
SXDSW-31939	8.781±0.082	7.915±0.161	8.945±0.087	8.868±0.077	8.880	8.962	8.082
SXDSW-31979	8.594±0.075	8.017±0.135	8.628±0.097	8.601±0.081	8.555	8.727	8.223
SXDSW-32006	8.804±0.056	7.789±0.087	8.951±0.077	8.874±0.077	8.887	8.969	8.003
SXDSW-32621	8.715±0.102	7.925±0.157	8.843±0.110	8.777±0.103	8.774	8.887	8.120
SXDSW-32738	8.351±0.096	8.337±0.141	8.208±0.148	8.297±0.109	...	8.345	8.494
SXDSW-32847	8.616±0.084	8.132±0.114	8.754±0.096	8.702±0.086	8.686	8.801	8.271
SXDSW-33128	7.846±0.153	8.925±0.136	7.266±0.214	7.725±0.108	...	7.361	8.983
SXDSW-33968	8.584±0.064	8.078±0.110	8.655±0.077	8.622±0.060	8.584	8.734	8.259
SXDSW-34130	8.554±0.091	8.087±0.125	8.582±0.107	8.565±0.081	8.504	8.680	8.278

NOTE. — All metallicities are reported in form $Z = 12 + \log(\text{O}/\text{H})$. “N06” refers to Nagao et al. (2006).

TABLE 5
 NEWH α BALMER-CORRECTED METALLICITIES

ID	M91 upper	M91 lower	Z94	T04	N06	KK04 upper	KK04 lower
SXDSN-12615	9.077±0.009	6.776±0.080	9.301±0.017	9.218±0.015	...	9.071	7.242
SXDSN-18825	8.697±0.079	7.820±0.162	8.751±0.116	8.699±0.091	8.682	8.840	8.067
SXDSN-19822	8.700±0.066	7.986±0.092	8.839±0.080	8.773±0.068	8.771	8.880	8.159
SXDSN-20554
SXDSN-22048	9.068±0.021	7.048±0.136	9.276±0.041	9.196±0.040	...	9.132	7.400
SXDSN-22485	8.935±0.060	7.490±0.223	9.099±0.079	9.017±0.069	9.063	9.059	7.760
SXDSN-23784	8.692±0.122	8.064±0.234	8.852±0.145	8.785±0.118	8.784	8.884	8.202
SXDSN-23860
SXDSN-24371
SXDSN-24458	8.293±0.130	8.413±0.153	8.138±0.193	8.250±0.112	...	8.264	8.562
SXDSN-24652
SXDSN-26559
SXDSN-26798
SXDSN-26828
SXDSN-27037
SXDSN-28032	8.940±0.048	7.391±0.133	9.098±0.052	9.016±0.057	9.061	9.049	7.697
SXDSN-28267	8.868±0.063	7.671±0.162	9.025±0.074	8.944±0.070	8.970	9.019	7.902
SXDSN-31207	8.907±0.086	7.659±0.215	9.076±0.089	8.994±0.085	9.033	9.054	7.873
SXDSN-31304
SXDSN-31331	8.510±0.120	8.149±0.166	8.522±0.136	8.520±0.111	8.431	8.624	8.330
SXDSN-31929
SXDSN-32915	8.987±0.011	6.955±0.081	9.143±0.013	9.062±0.014	9.124	9.019	7.375
SXDSN-34643
SXDSN-34925	8.686±0.103	7.781±0.302	8.674±0.215	8.637±0.175	8.604	8.806	8.047
SXDSN-35455	8.684±0.167	7.982±0.277	8.809±0.165	8.748±0.144	8.740	8.858	8.165
SXDSN-35945	9.011±0.004	6.946±0.039	9.185±0.006	9.106±0.006	9.189	9.033	7.367
SXDSN-36476
SXDSN-38796	8.089±0.206	8.679±0.174	8.088±0.261	8.217±0.165	...	8.121	8.743
SXDSN-39242	9.002±0.036	7.201±0.194	9.178±0.050	9.098±0.051	9.178	9.075	7.544
SXDSN-39615
SXDSN-39807
SXDSN-41162
SXDSS-8347
SXDSS-12862
SXDSS-14115
SXDSS-14438
SXDSS-14722
SXDSS-15629
SXDSS-15945	8.468±0.222	8.247±0.309	8.518±0.259	8.516±0.179	8.425	8.598	8.396
SXDSS-16362	8.466±0.192	8.249±0.252	8.516±0.250	8.515±0.173	8.422	8.596	8.398
SXDSS-17510
SXDSS-17705
SXDSS-17733	8.717±0.110	7.824±0.210	8.804±0.145	8.743±0.116	8.735	8.871	8.061
SXDSS-17924
SXDSS-17941
SXDSS-17958
SXDSS-18370
SXDSS-18554
SXDSS-18617
SXDSS-19166
SXDSS-20452
SXDSS-20675	7.595±0.692	9.061±0.464	7.465±0.788	7.837±0.526	...	7.400	9.071
SXDSS-21192
SXDSS-21634	8.803±0.088	7.615±0.240	8.900±0.138	8.827±0.111	8.833	8.946	7.898
SXDSS-21861	8.612±0.137	8.026±0.216	8.684±0.182	8.645±0.136	8.614	8.763	8.220
SXDSS-21905	8.906±0.062	7.230±0.208	9.012±0.075	8.931±0.078	8.955	9.002	7.597
SXDSS-22205
SXDSS-22277
SXDSS-22355
SXDSS-22452
SXDSS-22538	8.900±0.051	7.474±0.171	9.046±0.055	8.965±0.076	8.995	9.025	7.768
SXDSS-22557
SXDSS-22728	8.667±0.145	7.927±0.204	8.747±0.158	8.695±0.123	8.678	8.821	8.142
SXDSS-22991
SXDSS-23167
SXDSS-23393	8.412±0.169	8.321±0.201	8.453±0.204	8.469±0.161	8.327	8.530	8.456
SXDSS-23647	8.620±0.136	8.013±0.212	8.693±0.159	8.651±0.135	8.623	8.771	8.210
SXDSS-23667	8.132±0.371	8.632±0.399	8.122±0.544	8.240±0.328	...	8.167	8.709
SXDSS-24027	8.614±0.168	8.023±0.284	8.686±0.215	8.646±0.176	8.616	8.765	8.218
SXDSS-24469
SXDSS-24609	8.397±0.229	8.315±0.282	8.394±0.264	8.426±0.219	8.185	8.485	8.462
SXDSS-26565
SXDSS-26597
SXDSS-26724
SXDSS-27335
SXDSS-28369

TABLE 5 — *Continued*

ID	M91 upper	M91 lower	Z94	T04	N06	KK04 upper	KK04 lower
SXDSS-28526	8.451±0.220	8.270±0.314	8.498±0.258	8.502±0.223	8.398	8.577	8.415
SXDSS-29206
SXDSS-29259
SXDSS-29327	8.525±0.207	8.165±0.293	8.584±0.265	8.566±0.206	8.506	8.665	8.331
SXDSS-29859
SXDSS-30051
SXDSS-30124	8.874±0.070	7.378±0.211	8.979±0.094	8.900±0.084	8.917	8.991	7.713
SXDSS-30142	8.620±0.142	7.942±0.329	8.628±0.225	8.600±0.177	8.555	8.743	8.171
SXDSS-30295	8.487±0.159	8.221±0.234	8.540±0.210	8.533±0.167	8.453	8.620	8.375
SXDSS-31496
SXDSS-32097	8.519±0.139	8.174±0.217	8.578±0.188	8.561±0.136	8.498	8.659	8.337
SXDSS-32132
SXDSS-32277	8.548±0.271	8.156±0.353	8.633±0.302	8.604±0.238	8.560	8.704	8.315
SXDSS-33021
SXDSS-33298	8.520±0.143	8.173±0.175	8.578±0.178	8.562±0.129	8.499	8.659	8.337
SXDSS-33787
SXDSS-35437	8.083±0.323	8.679±0.415	8.063±0.418	8.201±0.284	...	8.100	8.747
SXDSS-36006	8.534±0.206	8.152±0.322	8.594±0.264	8.574±0.204	8.517	8.675	8.320
SXDSS-36019	8.233±0.123	8.510±0.129	8.192±0.165	8.286±0.107	...	8.267	8.620
SXDSS-36053
SXDSS-36609	8.502±0.153	8.200±0.181	8.557±0.188	8.546±0.133	8.474	8.638	8.358
SXDSS-36655
SXDSS-36770	8.901±0.065	7.475±0.156	9.047±0.085	8.965±0.077	8.997	9.026	7.769
SXDSS-36865	8.621±0.161	8.041±0.301	8.715±0.186	8.669±0.179	8.646	8.783	8.224
SXDSS-36954
SXDSS-37057	8.730±0.127	7.796±0.240	8.818±0.146	8.756±0.130	8.750	8.884	8.039
SXDSS-37189	8.723±0.142	7.943±0.287	8.864±0.135	8.795±0.123	8.795	8.901	8.125
SXDSS-37234
SXDSS-37285
SXDSS-37540	8.688±0.126	7.885±0.276	8.771±0.166	8.715±0.142	8.702	8.843	8.109
SXDSS-37564	8.613±0.186	8.025±0.426	8.685±0.235	8.645±0.187	8.615	8.764	8.219
SXDSS-37774	8.499±0.191	8.204±0.284	8.554±0.281	8.543±0.194	8.470	8.634	8.362
SXDSS-37948
SXDSS-38003
SXDSS-38307
SXDSS-38541
SXDSS-38698	8.535±0.129	8.150±0.199	8.595±0.177	8.575±0.128	8.519	8.677	8.319
SXDSS-38754
SXDSS-39016	8.426±0.183	8.304±0.231	8.469±0.208	8.480±0.160	8.353	8.546	8.442
SXDSS-39160
SXDSS-39226
SXDSS-39288	8.705±0.065	7.949±0.106	8.835±0.069	8.770±0.065	8.766	8.879	8.137
SXDSS-39308
SXDSS-39548
SXDSS-40071
SXDSS-40667	8.121±0.470	8.643±0.381	8.109±0.489	8.231±0.292	...	8.152	8.717
SXDSS-41193	8.434±0.192	8.292±0.240	8.479±0.232	8.488±0.176	8.369	8.557	8.432
SXDSW-8210	8.965±0.034	6.917±0.129	9.090±0.067	9.008±0.074	9.051	9.003	7.337
SXDSW-9136
SXDSW-10296	8.366±0.122	8.372±0.141	8.388±0.169	8.422±0.117	8.163	8.466	8.500
SXDSW-11479	8.815±0.122	7.803±0.276	8.970±0.123	8.891±0.121	8.908	8.982	8.004
SXDSW-11971	9.056±0.030	7.142±0.182	9.255±0.048	9.176±0.042	...	9.132	7.466
SXDSW-12128	9.052±0.008	7.020±0.036	9.252±0.014	9.173±0.014	...	9.096	7.399
SXDSW-12890
SXDSW-13103
SXDSW-13564
SXDSW-13984	8.548±0.282	8.287±0.388	8.711±0.293	8.666±0.214	8.642	8.749	8.375
SXDSW-14401
SXDSW-14721
SXDSW-14768	8.911±0.020	7.632±0.055	9.079±0.022	8.997±0.027	9.037	9.055	7.856
SXDSW-15154	8.602±0.038	7.928±0.067	8.518±0.069	8.516±0.056	8.425	8.685	8.172
SXDSW-15503	9.080±0.016	6.998±0.072	9.298±0.026	9.216±0.022	...	9.147	7.359
SXDSW-15809
SXDSW-17066	8.586±0.068	8.149±0.086	8.709±0.069	8.664±0.055	8.639	8.763	8.294
SXDSW-17078
SXDSW-17122	8.546±0.160	8.270±0.179	8.700±0.148	8.657±0.114	8.631	8.741	8.369
SXDSW-17857	8.717±0.079	7.811±0.172	8.796±0.102	8.736±0.075	8.727	8.868	8.054
SXDSW-17950
SXDSW-18531	8.957±0.039	7.340±0.087	9.120±0.052	9.038±0.058	9.091	9.057	7.656
SXDSW-18825	8.675±0.125	7.967±0.227	8.786±0.157	8.728±0.137	8.717	8.843	8.160
SXDSW-19359
SXDSW-19641	8.801±0.084	7.582±0.171	8.881±0.092	8.810±0.096	8.813	8.939	7.877
SXDSW-20516	8.509±0.083	8.144±0.136	8.508±0.100	8.509±0.080	8.411	8.616	8.329
SXDSW-20939
SXDSW-20960	9.012±0.018	7.054±0.049	9.190±0.024	9.110±0.028	9.197	9.056	7.444
SXDSW-21422
SXDSW-21499	8.769±0.145	7.947±0.311	8.935±0.152	8.858±0.139	8.869	8.954	8.104

TABLE 5 — *Continued*

ID	M91 upper	M91 lower	Z94	T04	N06	KK04 upper	KK04 lower
SXDSW-21553
SXDSW-22444
SXDSW-23533	8.702±0.096	8.002±0.180	8.848±0.115	8.782±0.097	8.780	8.886	8.166
SXDSW-23680	8.953±0.042	7.435±0.124	9.120±0.064	9.038±0.057	9.091	9.067	7.717
SXDSW-24515	8.977±0.043	7.483±0.119	9.153±0.052	9.073±0.049	9.140	9.097	7.728
SXDSW-24653	8.956±0.073	7.555±0.258	9.130±0.079	9.049±0.083	9.105	9.087	7.784
SXDSW-24830
SXDSW-25068	9.067±0.011	7.148±0.041	9.272±0.017	9.191±0.016	...	9.154	7.455
SXDSW-25629	8.820±0.144	7.902±0.329	8.994±0.147	8.914±0.161	8.934	8.999	8.054
SXDSW-25776
SXDSW-26406	8.615±0.098	8.146±0.153	8.759±0.127	8.705±0.112	8.690	8.803	8.280
SXDSW-26551
SXDSW-26690
SXDSW-26823
SXDSW-26847
SXDSW-26877
SXDSW-26991
SXDSW-27153	9.042±0.013	7.103±0.075	9.236±0.022	9.157±0.022	...	9.102	7.456
SXDSW-27756	8.862±0.080	7.555±0.267	8.996±0.097	8.916±0.106	8.936	8.999	7.837
SXDSW-28087
SXDSW-28260	8.643±0.119	8.091±0.158	8.782±0.100	8.725±0.091	8.714	8.827	8.239
SXDSW-28609	8.740±0.191	7.946±0.381	8.892±0.205	8.820±0.175	8.824	8.921	8.119
SXDSW-30365	8.923±0.053	7.558±0.156	9.089±0.056	9.007±0.054	9.049	9.057	7.807
SXDSW-31064	8.699±0.177	8.006±0.301	8.844±0.200	8.778±0.179	8.776	8.882	8.170
SXDSW-31483
SXDSW-31939	9.012±0.036	7.062±0.166	9.191±0.071	9.111±0.059	9.198	9.058	7.448
SXDSW-31979	8.745±0.054	7.611±0.116	8.713±0.093	8.668±0.074	8.644	8.863	7.912
SXDSW-32006	8.909±0.027	7.227±0.131	9.017±0.035	8.936±0.030	8.961	9.003	7.594
SXDSW-32621
SXDSW-32738
SXDSW-32847
SXDSW-33128	8.899±0.076	7.505±0.197	9.048±0.083	8.967±0.086	8.998	9.028	7.788
SXDSW-33968	8.544±0.083	8.093±0.125	8.557±0.121	8.546±0.080	8.474	8.662	8.287
SXDSW-34130

NOTE. — All metallicities are reported in form $Z = 12 + \log(\text{O}/\text{H})$. “N06” refers to [Nagao et al. \(2006\)](#).

TABLE 6
SAMPLE CUTS AND SUBSAMPLES USED IN ANALYSIS

Sample Cut	N (total)	N (no AGN)	SFR Comparison (Section 4.1)	M_{\star} -SFR Relation (Section 4.2)	M_{\star} - Z Relation (Section 4.3)	M_{\star} - Z -SFR Relation (Section 4.4)
No restrictions	299	278				
Good SED fit ($\chi^2 < 10$)	274	255	X	X	X	X
u -band photometry	174	160	X			
Narrowband S/N $> 3\sigma$	209	202	X	X		X
Metallicity cut ¹	166	147			X	X
Total			114	188	136	119

NOTE. — Note that AGN are removed for all four analyses listed. Also note that these sample cuts denote only the restrictions placed on datasets. Further restrictions (for linear or planar fits) are not listed here and are noted in the text and figures.

¹ The “metallicity cut” includes a 3σ restriction on $[\text{O II}]$, $[\text{O III}]$, and $\text{H}\beta$ (i.e., the $R_{23}(3\sigma)$ sample), as well as the removal of sources for which the calculated M91 upper-branch metallicity was lower than the M91 lower-branch metallicity.

TABLE 7
NEW $\text{H}\alpha$ M_\star - Z AND M_\star -SFR RELATION BINNED POINTS

M_\star -SFR			M_\star - Z		
M_\star	SFR	σ	M	Z	σ
9.27	0.06	0.454	9.27	8.64	0.148
9.52	0.27	0.313	9.52	8.80	0.241
9.76	0.64	0.373	9.76	8.73	0.182
10.01	0.83	0.329	10.02	8.93	0.244
10.29	1.05	0.419	10.30	8.95	0.142
10.59	1.18	0.379	10.61	8.99	0.114
10.81	1.50	0.337	10.83	9.05	0.137
11.15	1.54	0.424	11.17	9.06	0.075
			11.53	8.96	0.027
			11.78	8.99	0.034

TABLE 8
PRINCIPAL COMPONENT ANALYSIS PLANAR RESULTS

Sample ¹ (1)	N (2)	Metallicity (3)	α (4)	β (5)	γ (6)	δ (7)	σ (8)	$P(V1)$ (9)	$P(V2)$ (10)	$P(V1+V2)$ (11)
H α -based SFRs										
$R_{23}(3\sigma)$	119	T04	$-0.384^{+0.03}_{-0.04}$	0.923 ± 0.02	$0.087^{+0.04}_{-0.03}$	$4.301^{+0.57}_{-0.46}$	0.181	78.8 ± 1.6	15.2 ± 1.5	94.0 ± 0.5
$M_\star < 10^{10} M_\odot$	79	T04	$-0.798^{+0.13}_{-0.04}$	$0.649^{+0.11}_{-0.14}$	$0.152^{+0.05}_{-0.06}$	$-1.666^{+1.90}_{-2.38}$	0.170	69.5 ± 2.4	18.9 ± 2.0	88.3 ± 1.4
$M_\star \geq 10^{10} M_\odot$	40	T04	$-0.322^{+0.05}_{-0.04}$	0.947 ± 0.02	0.103 ± 0.04	$5.403^{+0.39}_{-0.78}$	0.159	73.3 ± 3.2	21.3 ± 3.1	94.5 ± 1.0
$R_{23}(3\sigma)$	119	M91	$-0.329^{+0.03}_{-0.04}$	$0.946^{+0.01}_{-0.02}$	$0.063^{+0.03}_{-0.04}$	$5.006^{+0.52}_{-0.41}$	0.170	79.5 ± 1.6	15.1 ± 1.5	94.6 ± 0.5
$M_\star < 10^{10} M_\odot$	79	M91	$-0.717^{+0.17}_{-0.09}$	$0.763^{+0.12}_{-0.16}$	0.128 ± 0.07	$-0.285^{+2.85}_{-2.28}$	0.172	70.5 ± 2.4	17.8 ± 1.9	88.4 ± 1.4
$M_\star \geq 10^{10} M_\odot$	40	M91	$-0.270^{+0.04}_{-0.03}$	$0.964^{+0.01}_{-0.02}$	0.093 ± 0.04	$5.875^{+0.42}_{-0.52}$	0.136	74.5 ± 3.2	21.2 ± 3.1	95.8 ± 0.7
$R_{23}(5\sigma)$	90	T04	-0.446 ± 0.05	$0.884^{+0.03}_{-0.02}$	0.127 ± 0.04	$3.444^{+0.54}_{-0.68}$	0.175	78.7 ± 1.9	15.4 ± 1.7	94.1 ± 0.6
$M_\star < 10^{10} M_\odot$	61	T04	-0.812 ± 0.10	$0.632^{+0.13}_{-0.20}$	$0.205^{+0.06}_{-0.09}$	-1.770 ± 2.83	0.171	71.9 ± 2.4	17.1 ± 1.9	88.9 ± 1.4
$M_\star \geq 10^{10} M_\odot$	29	T04	$-0.438^{+0.07}_{-0.05}$	0.894 ± 0.03	$0.130^{+0.04}_{-0.03}$	$3.705^{+0.80}_{-1.00}$	0.155	74.2 ± 4.1	20.5 ± 3.7	94.6 ± 1.1
$R_{23}(5\sigma)$	90	M91	-0.388 ± 0.04	$0.923^{+0.01}_{-0.03}$	$0.102^{+0.04}_{-0.03}$	$4.193^{+0.63}_{-0.50}$	0.166	79.4 ± 1.9	15.2 ± 1.7	94.6 ± 0.6
$M_\star < 10^{10} M_\odot$	61	M91	-0.750 ± 0.16	$0.707^{+0.20}_{-0.13}$	0.180 ± 0.08	$-0.386^{+3.86}_{-3.09}$	0.170	72.9 ± 2.4	16.2 ± 1.9	89.1 ± 1.4
$M_\star \geq 10^{10} M_\odot$	29	M91	$-0.368^{+0.05}_{-0.06}$	$0.924^{+0.02}_{-0.03}$	$0.120^{+0.03}_{-0.04}$	$4.568^{+0.64}_{-0.80}$	0.134	75.7 ± 4.0	20.1 ± 3.7	95.8 ± 0.9
SED-based SFRs										
$R_{23}(3\sigma)$	119	T04	$-0.384^{+0.04}_{-0.05}$	$0.917^{+0.03}_{-0.02}$	$0.097^{+0.04}_{-0.05}$	$4.318^{+0.53}_{-0.66}$	0.180	79.0 ± 1.8	14.7 ± 1.7	93.7 ± 0.6
$M_\star < 10^{10} M_\odot$	79	T04	-0.794 ± 0.08	0.605 ± 0.16	$0.211^{+0.10}_{-0.06}$	$-2.723^{+2.42}_{-1.82}$	0.162	65.1 ± 2.8	21.4 ± 2.3	86.5 ± 1.6
$M_\star \geq 10^{10} M_\odot$	40	T04	$-0.311^{+0.06}_{-0.05}$	0.952 ± 0.02	$0.070^{+0.05}_{-0.04}$	$5.479^{+0.60}_{-0.75}$	0.163	77.3 ± 2.8	17.5 ± 2.7	94.8 ± 0.9
$R_{23}(3\sigma)$	119	M91	-0.333 ± 0.04	$0.944^{+0.01}_{-0.02}$	0.076 ± 0.04	$4.979^{+0.47}_{-0.59}$	0.169	79.7 ± 1.8	14.6 ± 1.8	94.3 ± 0.5
$M_\star < 10^{10} M_\odot$	79	M91	$-0.734^{+0.15}_{-0.08}$	$0.664^{+0.17}_{-0.12}$	0.201 ± 0.09	-0.941 ± 2.51	0.159	66.0 ± 2.8	20.5 ± 2.3	86.5 ± 1.6
$M_\star \geq 10^{10} M_\odot$	40	M91	$-0.253^{+0.04}_{-0.05}$	$0.968^{+0.01}_{-0.02}$	$0.063^{+0.03}_{-0.04}$	$5.977^{+0.46}_{-0.58}$	0.141	78.5 ± 2.8	17.5 ± 2.7	96.0 ± 0.7
$R_{23}(5\sigma)$	90	T04	$-0.419^{+0.04}_{-0.05}$	$0.907^{+0.02}_{-0.04}$	$0.116^{+0.06}_{-0.04}$	$4.001^{+0.44}_{-0.87}$	0.180	75.9 ± 2.5	17.1 ± 2.4	93.0 ± 0.7
$M_\star < 10^{10} M_\odot$	61	T04	$-0.826^{+1.65}_{-0.00}$	$0.537^{+0.17}_{-0.91}$	$0.287^{+0.06}_{-0.70}$	$-2.508^{+9.03}_{-5.02}$	0.156	68.6 ± 2.8	19.0 ± 2.1	87.6 ± 1.7
$M_\star \geq 10^{10} M_\odot$	29	T04	$-0.399^{+0.06}_{-0.07}$	$0.912^{+0.03}_{-0.04}$	$0.093^{+0.05}_{-0.04}$	$4.117^{+0.84}_{-1.06}$	0.164	72.8 ± 4.0	21.1 ± 3.7	93.9 ± 1.3
$R_{23}(5\sigma)$	90	M91	$-0.373^{+0.04}_{-0.05}$	$0.924^{+0.02}_{-0.03}$	$0.104^{+0.05}_{-0.04}$	$4.423^{+0.66}_{-0.53}$	0.166	76.5 ± 2.5	17.1 ± 2.4	93.6 ± 0.7
$M_\star < 10^{10} M_\odot$	61	M91	$-0.865^{+1.73}_{-0.00}$	$0.594^{+0.27}_{-1.10}$	$0.260^{+0.17}_{-0.64}$	$-2.297^{+7.35}_{-1.84}$	0.164	69.5 ± 2.8	18.3 ± 2.2	87.8 ± 1.6
$M_\star \geq 10^{10} M_\odot$	29	M91	$-0.336^{+0.05}_{-0.06}$	$0.944^{+0.01}_{-0.03}$	$0.078^{+0.04}_{-0.03}$	$4.870^{+0.68}_{-0.85}$	0.143	74.3 ± 3.9	20.9 ± 3.7	95.2 ± 0.9

NOTE. — See Section 4.4.1 for further details. PCA plane defined as $\alpha \log(M_\star/M_\odot) + \beta[12 + \log(\text{O}/\text{H})] + \gamma \log(\text{SFR}/(M_\odot \text{ yr}^{-1})) = \delta$. The rms perpendicular to the PCA plane is provided in Column 8.

¹ The $R_{23}(3\sigma)$ and $R_{23}(5\sigma)$ samples are selected by requiring detections of [O II], [O III], and H β at 3σ and 5σ , respectively.

TABLE 9
 $M = f(Z, \text{SFR})$ REGRESSION PLANAR RESULTS

Sample ¹ (1)	N (2)	Metallicity (3)	β_M (4)	γ_M (5)	δ_M (6)
H α -based SFRs					
$R_{23}(3\sigma)$	119	T04	$0.67^{+0.13}_{-0.11}$	$0.50^{+0.04}_{-0.05}$	$3.75^{+1.02}_{-1.01}$
$R_{23}(3\sigma)$	119	M91	$0.77^{+0.14}_{-0.16}$	0.51 ± 0.04	$2.88^{+1.35}_{-1.21}$
$R_{23}(5\sigma)$	90	T04	0.90 ± 0.05	0.24 ± 0.03	$1.89^{+0.49}_{-0.42}$
$R_{23}(5\sigma)$	90	M91	$1.07^{+0.08}_{-0.06}$	$0.23^{+0.02}_{-0.03}$	$0.45^{+0.57}_{-0.65}$
SED-based SFRs					
$R_{23}(3\sigma)$	119	T04	$0.25^{+0.11}_{-0.13}$	$0.59^{+0.04}_{-0.05}$	$7.16^{+1.23}_{-1.07}$
$R_{23}(3\sigma)$	119	M91	$0.30^{+0.15}_{-0.18}$	0.59 ± 0.04	$6.76^{+1.37}_{-1.20}$
$R_{23}(5\sigma)$	90	T04	$0.69^{+0.05}_{-0.06}$	$0.54^{+0.04}_{-0.03}$	$3.52^{+0.56}_{-0.53}$
$R_{23}(5\sigma)$	90	M91	$0.83^{+0.07}_{-0.08}$	$0.55^{+0.04}_{-0.04}$	2.27 ± 0.65

NOTE. — See Section 4.4.2 for further details. Regression plane defined as $\log(M_*/M_\odot) = \beta_M [12 + \log(\text{O}/\text{H})] + \gamma_M \log(\text{SFR}/(M_\odot \text{ yr}^{-1})) + \delta_M$.

¹ The $R_{23}(3\sigma)$ and $R_{23}(5\sigma)$ samples are selected by requiring detections of [O II], [O III], and H β at 3σ and 5σ , respectively.

TABLE 10
 $Z = f(M, \text{SFR})$ REGRESSION PLANAR RESULTS

Sample ¹ (1)	N (2)	Metallicity (3)	α_Z (4)	γ_Z (5)	δ_Z (6)
H α -based SFRs					
$R_{23}(3\sigma)$	119	T04	0.23 ± 0.02	$0.01^{+0.02}_{-0.03}$	$6.61^{+0.18}_{-0.12}$
$R_{23}(3\sigma)$	119	M91	0.19 ± 0.02	0.00 ± 0.02	$6.97^{+0.18}_{-0.15}$
$R_{23}(5\sigma)$	90	T04	$0.26^{+0.03}_{-0.02}$	$0.00^{+0.03}_{-0.02}$	$6.32^{+0.25}_{-0.24}$
$R_{23}(5\sigma)$	90	M91	0.22 ± 0.02	-0.01 ± 0.02	$6.68^{+0.19}_{-0.20}$
SED-based SFRs					
$R_{23}(3\sigma)$	119	T04	0.25 ± 0.02	$-0.03^{+0.03}_{-0.02}$	$6.39^{+0.22}_{-0.19}$
$R_{23}(3\sigma)$	119	M91	0.21 ± 0.02	-0.03 ± 0.02	$6.81^{+0.19}_{-0.14}$
$R_{23}(5\sigma)$	90	T04	$0.28^{+0.02}_{-0.03}$	-0.04 ± 0.03	$6.15^{+0.25}_{-0.19}$
$R_{23}(5\sigma)$	90	M91	$0.23^{+0.02}_{-0.03}$	-0.04 ± 0.02	$6.60^{0.20}_{-0.18}$

NOTE. — See Section 4.4.2 for further details. Regression plane defined as $12 + \log(\text{O}/\text{H}) = \alpha_Z \log(M_*/M_\odot) + \gamma_Z \log(\text{SFR}/(M_\odot \text{ yr}^{-1})) + \delta_Z$.

¹ The $R_{23}(3\sigma)$ and $R_{23}(5\sigma)$ samples are selected by requiring detections of [O II], [O III], and H β at 3σ and 5σ , respectively.